OUTFLOWS AND ACCRETION AT THE DISK-MAGNETOSPHERE BOUNDARY

A Dissertation

Presented to the Faculty of the Graduate School

of Cornell University

in Partial Fulfillment of the Requirements for the Degree of

Doctor of Philosophy

by

Patrick S Lii

August 2015

OUTFLOWS AND ACCRETION AT THE DISK-MAGNETOSPHERE BOUNDARY

Patrick S Lii, Ph.D.

Cornell University 2015

Accreting magnetized stars are ubiquitous throughout astrophysics and can be found in a variety of astrophysical contexts at both the dawning and closing stages of stellar evolution. These include the young stars at the center of T Tauri-type systems, accreting white dwarfs in cataclysmic variables as well as neutron stars found in low-mass X-ray binaries. The interaction between these stars and their accretion discs is a process which is fundamental to astrophysics: of particular importance is the disc-magnetosphere interaction which determines many of the spectral and time-variable photometric signatures observed in these systems. However, direct imaging of the disc-magnetosphere boundary is observationally challenging due to current resolution limitations while purely analytical studies are difficult due to the highly non-linear nature of magnetohydrodynamic interactions. Simulations bridge the gap between theory and observation and permit us to model the complex interactions in the inner disc with unprecedented detail.

In this work, we present the results of pioneering magnetohydrodynamic (MHD) simulations of accretion, planet migration and outflow phenomena at the disc-magnetosphere boundary and in the inner disc. In order to investigate these processes, we have developed scalable, high-resolution Godunov-type MHD codes in 2.5D axisymmetric cylindrical, 2D plane polar, and fully 3D cylindrical coordinates aimed at studying accretion driven by the magnetorotational instability as well as the disc-magnetosphere interaction. The codes support the inclusion of a planetary perturber and include modules for α-type viscosity and diffusivity in the disc.

Our MHD simulations have established the occurrence of long-lasting outflows in

both slowly and rapidly rotating stars. In the slowly rotating regime where $r_m \leq r_c$, a well-collimated outflow is launched from the disc-magnetosphere boundary in regimes where the accretion rate is high and the stellar dipole is strongly compressed. The models show that the matter outflows from the disc-magnetosphere boundary with half-opening angles $\theta = 20-30^\circ$ and is collimated by the toroidal magnetic field such that the opening angle narrows to $\theta = 4 - 20^\circ$ at the edge of the simulation region. The outflow velocities range from 30 km s^{-1} at the outer edge of the jet to more than 260 km s^{-1} in the interior regions. This outflow mechanism may help to explain the spectral features observed in the major accretion events associated with FU Orionis and EX Lupi-type outbursts as well as the powerful bipolar jets observed in T Tauri systems.

In the rapidly rotating *propeller regime* of accretion where the magnetosphere rotates faster than the inner disk, the MHD models show the emergence a matter-dominated magnetocentrifugal outflow driven from the disc-magnetosphere boundary. However, unlike the outflow in slower rotating regime, the propeller outflow is primarily rotation-powered and can launch a large majority of the accreting matter into a wide angle propeller wind ($\theta \sim 45^\circ$). If the accretion rate exceeds the ejection rate, the accretion onto the star proceeds episodically through a cyclic accumulation-accretion mechanism in which episodes of matter accumulation are followed by a brief episode of simultaneous ejection and accretion onto the star. This cyclic accumulation-accretion mechanism may explain the decahertz flaring observed in some accreting millisecond pulsars expected to be in the propeller regime of accretion. These propeller-driven outflows efficiently transport angular momentum away from the star and may be largely responsible for the rapid spin-down of stars in the propeller regime.

While the star-disc interaction is critical for understanding the inner disc dynamics, planet-disc interactions play a dominant role in determining the final period-mass distribution of planets discovered by modern exoplanet surveys. Protoplanetary discs

can have large central cavities at the dust sublimation radius or the disc-magnetosphere boundary. Using 2D simulations, Masset et al. 2006 showed that migrating planets which encounter the positive surface density gradient at the disc-cavity boundary may become stably trapped due to the action of the corotation torque. We build on their work and study the disc-planet interaction for planets with initial orbits inside, outside, and coincident with the disc-cavity boundary in both 2D and 3D hydrodynamic simulations. We find that the trapping mechanism persists in the 3D simulations, with migration rates that depend on the surface density profile at the surface density transition. The trapping mechanism is robust and may cause the planet to migrate inward or outward in tandem with the disc-cavity boundary which may move as the young star evolves along the Hayashi track toward the main sequence.

BIOGRAPHICAL SKETCH

Patrick Lii was born on a cloudy day in California and grew up in the San Francisco Bay Area. He spent his formative years in the South Bay and graduated from Archbishop Mitty High School before moving to Berkeley, CA to attend UC Berkeley in 2005. In 2009, he received dual Bachelor's degrees in Physics and Astronomy from UC Berkeley and moved to Ithaca, New York to begin a doctorate program in Astronomy. In Ithaca, he discovered that sandals and sneakers are not suitable year-round footwear for upstate New York.

To my parents, who first instilled in me an appetite for knowledge and a thirst for understanding.

And to my grandparents, who inspired me to look to the stars and have never wavered in their support.

ACKNOWLEDGEMENTS

There are many people without whom this thesis would not have been possible. First and foremost, I would like to thank my PhD advisors, Marina Romanova and Richard Lovelace, for their constant support and guidance. Their mentorship over the past few years has been an invaluable source of knowledge and wisdom. Looking back at the past few years, I can see how much I have matured as a scientist under their guidance. Throughout my graduate career, they have treated me as a member of both their academic and immediate family, something for which I will be forever grateful. I also greatly appreciate the substantial contributions from Alexander Koldoba and Galina Ustyugova to the work presented here; they have put substantial effort in developing the numerical codes which have made this research possible and their mentorship has been invaluable in developing the my understanding of the computational aspects of my work. Also, special thanks to my fellow graduate students in the Plasma Astrophysics group, Sergei and Megan, for the many useful discussions (and distractions) throughout the years.

I would like to thank the many professors at Cornell in astronomy, physics, and engineering whose knowledge and guidance I have benefited from. In particular, I am lucky to have several outstanding professors on my special committee: David Chernoff, Peter Diamessis, and Gordon Stacey who have all contributed invaluably to my graduate education. I would especially like to thank James Lloyd for stepping in as the proxy chair on my committee and Monica Armstrong for being an amazing GFA; they were an invaluable resource in dealing with the administrative aspects of the thesis and the defense.

Finally I would like to thank the graduate students of Space Sciences and the many lifelong friends I've made while at Cornell who have helped to make Ithaca's long winters tolerable and beautiful summers unforgettable. In particular, I want to acknowledge

my cohort–Everett and Joyce–without whom I would not have survived my first year at Cornell; the backpacking crew–Jason, Tyler, Mike, Jeremy, and Everett–for the good company on our many adventures into upstate New York; Ryan and Lyann for making sure that I actually got out of the office from time to time; and the archers of the Cornell Archery Club for all the fun practices over the years.

The research in this work was supported in part by NASA grants NNX10AF63G, NNX12AI85G and NNX11AF33G as well as NSF grants AST-1008636, AST-1211318. We utilized computational resources provided by the NASA High-End Computing (HEC) Program through the NASA Advanced Supercomputing (NAS) Division at Ames Research Center and the NASA Center for Computational Sciences (NCCS) at Goddard Space Flight Center.

TABLE OF CONTENTS

LIST OF TABLES

LIST OF FIGURES

LIST OF ABBREVIATIONS

AMP accreting millisecond pulsar

cTTs classical T Tauri star

CV cataclysmic variable

HD hydrodynamics

LMXB low-mass X-ray binary

MHD magnetohydrodynamics

MRI magnetorotational instability

YSO young stellar object

LIST OF SYMBOLS

$\boldsymbol{B}$ magnetic field vector

c_s sound speed

$\boldsymbol{F}$ flux vector (Equation 2.6)

k_B Boltzmann gas constant

$\boldsymbol{M}$ momentum tensor (Equation 2.8)

M_* stellar mass

$\mathrm{M}_\odot$ mass of the Sun

p pressure

r cylindrical radius

$\boldsymbol{r}$ cylindrical vector (r, ϕ, z)

R spherical radius

$\boldsymbol{R}$ spherical vector (R, ϕ, θ)

R_* stellar radius

$\mathrm{R}_\odot$ mass of the Sun

s entropy per unit mass

t time

$\boldsymbol{U}$ conservative variable vector (Equation 2.6)

$\boldsymbol{v}$ velocity vector

α_d diffusivity parameter

α_v Shakura and Sunyaev [1973] viscosity parameter

β plasma parameter

β_1 kinetic plasma parameter

γ adiabatic index

Γ torque

θ polar angle

Π surface pressure

ρ density

Σ surface density

ϕ azimuthal angle

Φ gravitational potential

Ψ magnetic flux function

Ω angular velocity

Ω_K Keplerian angular velocity

Ω_* stellar angular velocity

CHAPTER 1

INTRODUCTION

Accreting magnetized stars are ubiquitous in astrophysics and can be found at both the dawning and closing stages of stellar evolution. These systems include nascent Class 0 and I protostars accreting from dense protoplanetary discs, classical T Tauri stars (cTTs), intermediate polars (IPs) in cataclysmic variables (CVs), as well as accreting millisecond pulsars (AMPs) accreting material from their binary companions. These seemingly disparate systems all share the common feature of disc accretion onto a magnetized central body. In young stellar systems, the central bodies are highly convective pre-main-sequence stars with kilogauss magnetic fields and widely varying disc accretion rates of 10^{-4} – 10^{-8} $M_{\odot}$/yr. In the post-main-sequence systems (IPs and AMPs), the central bodies are dense compact objects with remnant 10^{7} – 10^{9} G magnetic fields accreting material from their binary companions.

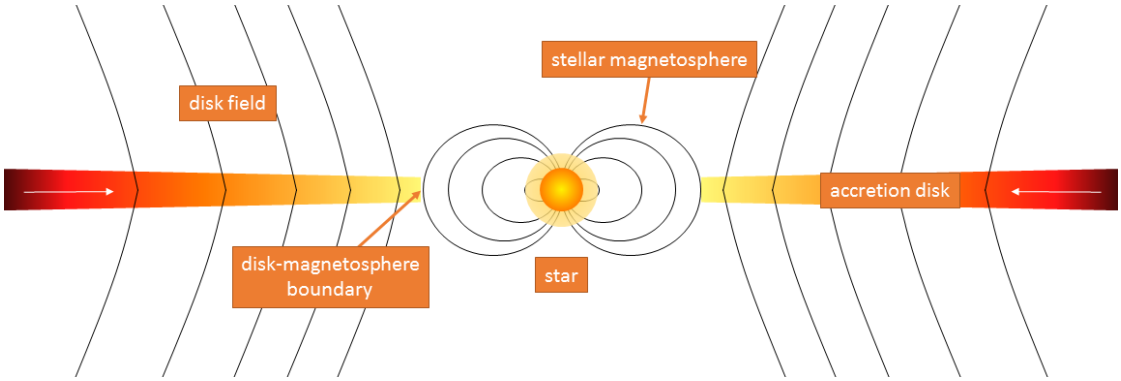

Figure 1.1: **Schematic diagram of an accreting magnetized system.**

A schematic diagram of the interior regions of an accreting magnetized system is shown in Figure 1.1. In these systems, the magnetic pressure of the stellar magnetic field clears a low density region surrounding the star known as the *stellar magnetosphere*. The interface between the low density magnetosphere and the higher density disk is known

as the *disk-magnetosphere boundary*. The location of this boundary is determined by the balance between the magnetic pressure from the stellar magnetic field and the gas and ram pressure of the disc plasma. This corresponds to the location where the kinetic plasma parameter $\beta_1 \equiv (p + \rho v^2)/(B^2/8\pi)$ is unity [Romanova et al., 2002]. For a disc in orbit around a star with an aligned dipole, the magnetospheric radius r_m approximately coincides with the Alfvén radius r_A

$$r_{\rm m} = k r_A = k \left(\frac{\mu^4}{2GM_* \dot{M}^2} \right)^{1/7} , \tag{1.1}$$

where G is the gravitational constant, M_* is the mass of the star, $\dot{M}$ is the accretion rate in the disc, μ is the dipole moment of the star, and k is a dimensionless quantity of order $0.5 - 1$ [Ghosh and Lamb, 1978]. Figure 1.2 shows a representative example of what such a system might look like in our 3D simulations. The stellar magnetic field can be highly complex, consisting of a superposition of dipole, quadrupole, octupole and higher order components that may be misaligned with the stellar spin axis [Donati et al., 2007, 2008, 2010, Gregory et al., 2008, Donati and Landstreet, 2009]. The matter from the disk can accrete onto the star through *funnel streams* which flow around the magnetosphere onto the magnetic poles of the star.

In addition to the stellar magnetic field, the surrounding accretion disk may be threaded by a large scale ordered magnetic field which has been advected in by the accreting matter [Bisnovatyi-Kogan and Ruzmaikin, 1974, 1976, Lovelace, 1976, Bisnovatyi-Kogan and Lovelace, 2007, Rothstein and Lovelace, 2008] or is generated by a magnetic dynamo process in the disk [Moffatt, 1978, Stepinski and Levy, 1988, Stepinski, 1992]. The magnetic fields play a critical role in the evolution of accreting stars: they are essential for launching and collimating outflows, angular momentum transport in the disk, the spin-down of fast-rotating stars, and explaining the observed variability in the inner regions of the disk.

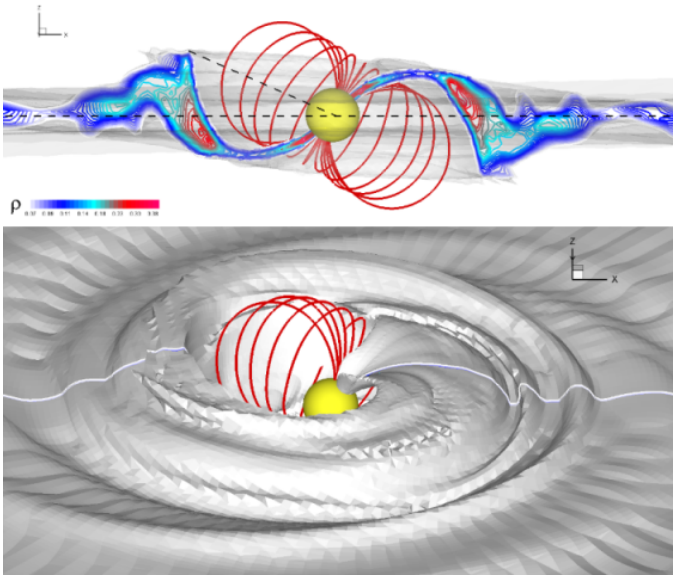

Figure 1.2: **The inner accretion disk in simulations.** The central star has a tilted dipole magnetic field and is orbited by an accretion disk. Adapted from Romanova et al. [2004].

1.1 Accretion in young stellar systems

Direct observations of the dynamics at the stellar magnetosphere are challenging due to the insufficient resolution of contemporary telescopes as well as obscuration of the inner regions by the accretion disc itself. The most observationally accessible accreting systems are classical T Tauri stars in nearby star forming regions where the disc-magnetosphere interaction is accessible through photometric and spectral observations [see reviews by Frank et al., 2014, Ray et al., 2007, Bouvier et al., 2007]. These accreting systems often exhibit well-collimated outflows which may originate from the disc-magnetosphere boundary or stellar surface, or as an extended disc wind [Blandford and Payne, 1982, Lovelace et al., 1991, Ferreira et al., 2006].

The outflows launched from these systems display an onion-like velocity structure with a high-velocity core surrounded by lower-velocity layers [Beck et al., 2007, Coffey

et al., 2008, Pyo et al., 2009, Agra-Amboage et al., 2011]. Direct imaging of cTTs microjets show that the cores of the outflows have velocities on the order of the Keplerian velocity of the inner disc suggesting that they are launched close to the star; additionally, integral field spectroscopy constrains the launching regions of these jets to the inner few AU of the disc [Dougados et al., 2000, Lavalley-Fouquet et al., 2000, Hartigan et al., 2004, Coffey et al., 2008, Maurri et al., 2014]. The outflows are launched with opening angles of $10 - 30^{\circ}$ and become rapidly collimated (either by the ambient medium or large-scale magnetic fields) as they flow outward [Lovelace et al., 1987, Ray et al., 2007]. These observations are consistent with a magnetocentrifugally launched disk wind in which matter flows up along magnetic field lines threading the disk [Blandford and Payne, 1982]. However, outflows may also be launched directly from the surface of the star as a stellar wind or from the disk-magnetosphere boundary as a magnetospheric wind [see review by Ferreira et al., 2006].

Photometric observations of these accreting systems often show periodic or aperiodic variability on timescales of the inner disc orbit, indicative of waves or warps in the disc or non-stationary accretion processes (such as instabilities) at the disc-magnetosphere boundary [Bouvier et al., 1999, Oliveira et al., 2000, Bouvier et al., 2003, Alencar et al., 2001, 2005, Schisano et al., 2009]. Longer term eruptive FUor and EXor-type events have also been observed in these young stars and are believed to be associated with sudden bursts of accretion onto the central body [Herbig, 1977, 2007, 2008, Evans et al., 2009, Caratti o Garatti et al., 2011, Sicilia-Aguilar et al., 2012].

1.1.1 The magnetorotational instability

The outflows in cTTs's facilitate star formation by removing angular momentum from the inner disk, thereby allowing for continued accretion onto the young star. However, the angular momentum transported away by the outflow alone is insufficient to account for the observed accretion rates in cTTs disks. Rather, the dominant angular momentum transport mechanism in astrophysical accretion disks is the magnetorotational instability (MRI) first described by Velikhov [1959] and Chandrasekhar [1960], and then applied to astrophysical disks by Balbus and Hawley [1991]. The MRI converts the disk's kinetic energy into magnetic energy as follows: consider a radial magnetic field line threading an accretion disk with one end anchored on a test mass $m_{\rm in}$ at $r_{\rm in}$ and the other end anchored on a test mass $m_{\rm out}$ at $r_{\rm out}$, with $r_{\rm in} < r_{\rm out}$. Both masses are in a Keplerian orbit around the central star. Since the mass at $r_{\rm in}$ is slightly closer to the star, its orbital velocity is higher than the test mass at $r_{\rm out}$ and there is a velocity shear between the two test particles. The magnetic field line connecting the two particles behaves like a spring under tension and resists the shear between the two test masses, dragging $m_{\rm in}$ backwards (thereby removing angular momentum from the interior particle) while dragging $m_{\rm out}$ forwards (thereby adding angular momentum to the exterior particle). In doing so, a negative torque is applied on the interior mass while a positive torque is applied to the exterior mass, resulting in a net transfer of angular momentum outward in the disk. As the interior and exterior test particles move apart from each other, the magnetic field line is stretched further, resulting in an even stronger torque and more efficient angular momentum transport. This mechanism is unstable and the MRI turbulence creates an effective viscosity as well as magnetic diffusivity in the disk which can account for the observed accretion rates in cTTs disks.

The MRI can only operate in regions of the disk that are sufficiently ionized as the

magnetic fields must be well-coupled to the matter. This means that the MRI is typically most efficient in the inner regions of the disk which are exposed to ionizing radiation from the star. In regions of the disk that are too cold, a high density *dead zone* will form where the MRI becomes inefficient and the accretion rate is low. This typically occurs in regions of the disk where the optical depth is too high for ionizing radiation from the star to penetrate.

The dead zone creates a bump in the density profile of the disk. Accretion disks may also have density transitions at the dust sublimation radius where the disk temperature is high enough to vaporize the dust, at ice lines where molecules condense out of their gas phase, and at the disk-magnetosphere boundary where the stellar magnetic pressure supports a low-density magnetospheric cavity. The density transitions in disks around young stars may play an important role in planet formation and migration. Rossby vortices which form in disk dead zones can trap dust, facilitating the formation of proto-planetary embryos [Lyra et al., 2009, Lyra and Mac Low, 2012]. In addition, the sharp gradient in the gas density at the disk-magnetosphere boundary and dust-sublimation radius may halt the inward migration of planets and protoplanetary embryos [Masset et al., 2006, Morbidelli et al., 2008].

1.1.2 Planet migration in protoplanetary disks

Planets in accretion disks can migrate due to tidal interaction with the matter in the disk. The tidal torque on the planet consists of two components: the differential Lindblad torque and the corotation torque [Goldreich and Tremaine, 1979, 1980]. The Lindblad torque arises from the planet's interaction with the spiral density waves raised by the planet at the Lindblad resonances, located where $m\Omega_p = (m \pm 1)\Omega$. For a Keplerian

disk, this corresponds to

$$r_{\rm LR} = \left(1 \pm \frac{1}{m}\right)^{2/3} r_p \ . \tag{1.2}$$

The positive sign represents the outer Lindblad resonances (OLR) and the negative sign represents the inner Lindblad resonances (ILR). The material interior to the planet's orbit tends to add angular momentum to the planet (i.e. creates a positive torque) while the material exterior to the planet's orbit tends to remove angular momentum (creates negative torque). The difference between the outer and inner Lindblad torques is known as the *differential Lindblad torque*. In a typical accretion disk, the outer Lindblad torque is larger in magnitude compared to the inner Lindblad torque and planet migration typically proceeds inward. The corotation torque arises from the planet's tidal interaction the material which has the same orbital frequency as the planet's orbit $\Omega = \Omega_p$.

There are two regimes of planet migration in protoplanetary disks. In *Type I migration*, the planet has insufficient mass to significantly alter the local disk density and both the differential Lindblad and corotation torques contribute to the overall torque on the planet. In *Type II migration*, the planet is sufficiently massive to open a low-density gap. Due to the paucity of matter in the planet's corotation region, the corotation torque is weak compared to the differential Lindblad torque and the planet's migration rate is set by the viscous timescale of the disk.

In both mass regimes, the migration may be strongly modified if the planet encounters a gap or cavity in the disk (for example, at the dust-sublimation radius or the edge of a dead zone). In the Type II regime, the planet migrates inward until the $m = 1$ OLR falls inside the cavity and the Lindblad torque goes to zero [Lin et al., 1996]. However, the planet-cavity interaction in the Type I regime is more complex due to the action of the corotation resonance. Masset et al. [2006] showed that the corotation torque becomes important when migrating embedded planets encounter density transitions in the

disk. This torque can halt the migration of the planet and create a stable *planet trap* at the cavity edge.

1.2 Accreting millisecond pulsars

Low mass X-ray binaries (LMXBs) are binary systems with a neutron star (or black hole) primary and a less massive ($M_* < \mathrm{M}_\odot$) main sequence or subgiant donor companion. The orbit of the binary tends to be relatively compact with orbital periods ranging from a few hours to a few days. In these systems, the donor companion has overfilled its Roche lobe and transfers material via an accretion disk onto the primary star. During the mass transfer, the disk heats up and the emission from the system is typically dominated by the accretion luminosity which peaks in the X-ray.

LMXBs are thought to be the progenitors of recycled millisecond pulsars. In LMXBs, angular momentum is added to the slowly rotating neutron star by the accreting matter, gradually spinning the compact star up until it becomes a rapidly rotating pulsar. This spin-up mechanism is known as the *recycling scenario* [see review by Srinivasan, 2010]. Hence, if the accreting primary in the LMXB is a neutron star, then it is known as an *accreting millisecond pulsar* (AMP). The accretion in these systems proceeds through funnel flows onto the magnetic poles of the star, giving rise to X-ray pulsations corresponding to the spin frequency of the neutron star [see review by Patruno and Watts, 2012]. As the mass transfer from the donor star declines, the rapidly rotating star is expected to transition from the X-ray bright, accretion-powered state to a radio-bright, rotation-powered state (i.e., a pulsar).

As is the case for young stellar systems, the inner regions of AMPs are inaccessible through direct observation. Rather, information on the interior regions is gleaned

from X-ray photometry and spectroscopy. One complicating factor is that the dynamical timescale of the inner disk can be just a few milliseconds in compact AMPs, necessitating high time cadence observations. Additionally since the emission peaks in the X-ray, which does not effectively penetrate the atmosphere, space-based X-ray observatories are required in order to study these accreting post-main-sequence systems. Nonetheless, much progress has been made in the last two decades in understanding these systems. In particular, the recycling scenario for millisecond pulsars has been directly confirmed for the first time by the identification of a number of systems which swing in between the rotation-powered radio and accretion-powered X-ray states [Papitto et al., 2013, Ferrigno et al., 2014, Patruno et al., 2014, Bassa et al., 2014, Bogdanov and Halpern, 2015]. Prior to this discovery, the link between the accretion and rotation-powered states had only been observed indirectly [Burderi et al., 2003, Hartman et al., 2008, di Salvo et al., 2008, Patruno, 2010, Papitto et al., 2011].

During the transitional phase between the accreting and rotation-powered states, the accretion rate declines and the magnetosphere of the accreting pulsar expands, pushing the system into the *propeller regime of accretion* in which the angular velocity of the star (and its magnetosphere) exceed the angular velocity of the inner disk. This occurs when the magnetospheric radius $r_{\rm m}$ is larger than the corotation radius $r_{\rm c}$, defined as

$$r_{\rm c} = \left(\frac{G\mathrm{M}_*}{\Omega_*^2}\right)^{1/3} . \tag{1.3}$$

The corotation radius represents the location where the angular velocity of the star, Ω_*, is equal to the Keplerian angular velocity of the disc, $\Omega_K = \sqrt{G\mathrm{M}_*/r^3}$. When $r_m \lesssim r_c$, the star is in the funnel flow regime in which matter from the disc may readily accrete onto the star. In the opposite regime where $r_m > r_c$ (i.e., the propeller regime), the rapidly rotating magnetosphere acts as a centrifugal barrier which can inhibit accretion onto the star or cause the star to spin down [Illarionov and Sunyaev, 1975, Lovelace et al., 1999]. If the star is in the "strong" propeller regime of accretion, the star can launch

centrifugally-driven outflows from the disk-magnetosphere boundary; this occurs when the azimuthal velocity at the disk-magnetosphere boundary exceeds the local escape velocity

$$\begin{aligned} v_\phi(r_\mathrm{m}) &> v_\mathrm{esc}(r_\mathrm{m}), \\ \Omega_* r_\mathrm{m} &> \sqrt{\frac{2GM_*}{r_\mathrm{m}}}, \\ \sqrt{\frac{GM_*}{r_\mathrm{c}^3}} r_\mathrm{m} &> \sqrt{\frac{2GM_*}{r_\mathrm{m}}}, \\ r_\mathrm{m} &> 2^{1/3} r_\mathrm{c} \,, \end{aligned} \tag{1.4}$$

where we have used Equation 1.3 for Ω_*. Thus, the propeller can drive outflows if the magnetospheric radius is roughly 1.26 times the corotation radius. This may occur if, for example, the mass transfer from the binary companion declines, depleting the material in the disk and causing the magnetosphere to expand outward.

The transitional AMPs often exhibit episodic X-ray flaring with frequencies of one to a few Hz [Patruno et al., 2009, Bult and van der Klis, 2014] and in some systems, X-ray variability on timescales of minutes to hours has also been observed [Ferrigno et al., 2014]. Additionally, the spectra hint at the existence of outflows, but direct observations of outflowing matter in these transitional systems has yet to be achieved [Ferrigno et al., 2014, Bogdanov and Halpern, 2015]. Observations of these systems hint at the propeller regime playing a role in the inner disk dynamics, but the exact mechanism driving the flaring and X-ray variability in these systems is not yet fully understood.

1.3 Overview

In this work, we investigate several outstanding scientific questions associated with accreting magnetized systems. Namely we seek to address the following questions related

to accreting protostellar and post-main-sequence stars:

- What is the mechanism behind the launching and collimation of outflows in young stellar systems?
- What role does the stellar magnetic field play in launching outflows?
- In what astrophysical systems is the propeller regime of accretion important? What effect does it have on the star and disk?
- How does the structure of protoplanetary accretion disks affect the migration of planets?

We investigate these problems using hydrodynamic (HD) and magnetohydrodynamic (MHD) simulations of accretion onto a central body. In Chapter 2, we describe the numerical model and the codes which were developed to investigate these accretion phenomena; in Chapter 3, we study the emergence of magnetically launched and collimated jets driven from the disc-magnetosphere boundary; in Chapter 4, we discuss the episodic accumulation-accretion cycle and outflows launched in the propeller regime of accretion; and in Chapter 5, we investigate the migration of planets near a low-density disc cavity.

CHAPTER 2

THE NUMERICAL MODEL

2.1 Chapter Overview

The inner regions of accretion discs tend to be highly ionized and are well-described by the equations of magnetohydrodynamics (MHD). The accretion disc dynamics can be numerically modeled by specifying:

1. The governing partial differential equations (PDEs) which describe how the accreting gas behaves (i.e., the equations of hydrodynamics or MHD): $\partial_t \boldsymbol{U} + \partial_x \boldsymbol{F} = 0$.
2. An algorithm to (approximately) solve the partial differential equations.
3. The initial conditions of the system: $\boldsymbol{U}(x, 0) = \boldsymbol{U}^0(x)$.
4. The boundary conditions of the system: $\boldsymbol{U}(0, t) = \boldsymbol{U}_L(t)$ and $\boldsymbol{U}(L, t) = \boldsymbol{U}_R(t)$.

This class of model is known as the initial boundary value problem: in order to investigate the dynamics of the system, we evolve the initial conditions $\boldsymbol{U}(x, 0)$ in time, subject to certain boundary conditions [see Toro, 2009, for a review]. Here, the domain on which the problem is solved extends from $0 \leq x \leq L$. The initial conditions of the problem specify the initial state of the fluid and the boundary conditions permit us to simulate a finite region of space by truncating the modeled region at $x = 0$ and $x = L$. And the governing MHD equations tell us how the initial conditions will evolve in space and time. This system of coupled partial differential equations is difficult to solve analytically for almost all non-trivial initial conditions. Instead, we employ an algorithm to solve the equations numerically.

The algorithm utilized in this work to solve the equations of MHD is a finite-volume scheme known as Godunov's method and may be applied to solve any initial boundary value problem based on conservative PDEs [Godunov, 1959]. Godunov's method works by discretizing the spatial domain into grid cells; each variable (for example, the density) is correspondingly discretized such that it is piecewise constant across each cell. Since the variables are piecewise constant, there is a discontinuity at the edges of each grid cell, resembling a local shock problem (i.e., a Riemann problem).

Thus, the fluxes between the cells can be calculated by solving the Riemann problem at each cell boundary. Once the fluxes across the boundaries are known, the net flux into the cell is known and state variables in each cell can be updated by advancing the numerical model forward in time. We present the 1D MHD equations here for the sake of illustration, but the algorithm can be applied to 2D or 3D problems by computing the fluxes along each coordinate separately. A more detailed description of the Godunov method is presented in §2.3.

In order to compute the fluxes between each cell, we devise an approximate Riemann solver based on the HLLD solver proposed by Miyoshi and Kusano [2005]. Instead of the energy equations, the solver solves the entropy-conserving form of the MHD equations. This Riemann solver is discussed in-depth in §2.4.2. The details of our codes and the entropy-conserving Riemann solver are described in full in Koldoba et al. [August 2015].

In this chapter, we present a summary of the main aspects of the code: in §2.2 we discuss the underlying equations of MHD; in §2.3, we discuss the algorithm (Godunov's method) which is used to solve the equations of MHD; in §2.4.2, we cover the entropy-conserving Riemann solver which is used in our numerical algorithm to calculate the intercell fluxes; in §2.5, we briefly describe the initial and boundary conditions used in

our models; in §2.6, we present the various grid geometries utilized by our models; and in §2.7, we wrap up by discussing the parallelized implementation of the code.

2.2 The equations of MHD

The inner regions of accretion discs are typically highly ionized and the plasma is sufficiently collisional to be treated as a fluid. The state of the plasma is completely specified by the density ρ, pressure p, entropy per unit mass s, velocity $\boldsymbol{v}$, and magnetic field $\boldsymbol{B}$ of the fluid. The fluid is in Keplerian orbit around the star and in vertical hydrostatic equilibrium such that there is initial force equilibrium in all directions. The initial conditions are described in detail in §2.5. The set of equations which describe the evolution of such a system are known as the equations of ideal MHD. These equations consist of:

1. The continuity equation

$$\partial_t \rho + \nabla \cdot (\rho \boldsymbol{v}) = 0 \,, \tag{2.1}$$

   which describes the matter flux in the fluid.

2. The momentum conservation equation (also known as the equation of motion)

$$\rho \frac{D\boldsymbol{v}}{Dt} = -\nabla p + \boldsymbol{j} \times \boldsymbol{B} + \rho \boldsymbol{g} + \mathbf{F}_{\text{visc}} \tag{2.2}$$

   which describes how the fluid behaves in the presence of the pressure gradient, magnetic, gravitational and viscous forces. Here $D/Dt \equiv \partial_t + \boldsymbol{v} \cdot \nabla$ is the material derivative, $\boldsymbol{j}$ is the current, $\boldsymbol{g} = -\nabla\Phi$ is the external gravitational acceleration, and $\mathbf{F}_{\text{visc}}$ is the viscous force. We can drop the displacement current from Ampere's law to rewrite the magnetic term as

$$\boldsymbol{j} \times \boldsymbol{B} = \frac{\boldsymbol{B} \cdot \nabla \boldsymbol{B}}{4\pi} - \nabla \frac{B^2}{8\pi} \,. \tag{2.3}$$

The first term represents the magnetic tension while the second term represents the magnetic pressure force where the magnetic pressure is $p_{\rm mag} = B^2/8\pi$. Note that the although the magnetic pressure is isotropic, the net magnetic force is directional.

3. The entropy conservation equation

$$\frac{\partial \rho s}{\partial t} + \nabla \cdot (\rho \boldsymbol{v} s) = Q \tag{2.4}$$

where Q is an entropy source term, $s = p/\rho^\gamma$ is the entropy per unit mass and γ is the adiabatic index.

4. The induction equation

$$\frac{\partial \boldsymbol{B}}{\partial t} = \nabla \times (\boldsymbol{v} \times \boldsymbol{B}) + \eta_{\rm diff} \nabla^2 \boldsymbol{B} \tag{2.5}$$

which describes the coupling between the magnetic field and the fluid. Here $\eta_{\rm diff}$ is the diffusivity coefficient.

Equations 2.1-2.5 can be represented in a more compact form which is useful when discussing the implementation of the numerical MHD solver. In this form, the conserved variables and fluxes are condensed into two vectors [Skinner and Ostriker, 2010, Koldoba et al., August 2015]

$$\boldsymbol{U} = [\rho, \rho s, \rho \boldsymbol{v}, \boldsymbol{B}]^T \quad \text{and} \quad \boldsymbol{F}(\boldsymbol{U}) = [\rho \boldsymbol{v}, \rho \boldsymbol{v} s, \boldsymbol{M}, \boldsymbol{J}]^T \ , \tag{2.6}$$

where $\boldsymbol{J}$ is the induction tensor with components

$$J_{ij} = v_i B_j - v_j B_i \ , \tag{2.7}$$

and $\boldsymbol{M}$ is the momentum tensor with components

$$M_{ij} = \rho v_i v_j - \frac{B_i B_j}{4\pi} + \delta_{ij} p_{\rm tot} - V_{ij,\rm visc} \ . \tag{2.8}$$

Here δ_{ij} is the Kronecker delta function, $p_{\rm tot} = p + B^2/8\pi$ is the total pressure and $\boldsymbol{V}_{\rm visc}$ is the viscous tensor (see §2.2.1). Equation 2.6 allows us to succinctly rewrite the equations of MHD as

$$\partial_t \boldsymbol{U} + \nabla \cdot \boldsymbol{F}(\boldsymbol{U}) = \boldsymbol{Q} \tag{2.9}$$

where $\boldsymbol{Q}$ is the vector of non-ideal source terms

$$\boldsymbol{Q} = [0, Q, -\rho\nabla\Phi, -\eta_{\rm diff}\nabla^2\boldsymbol{B}]^T \ . \tag{2.10}$$

Appendix A shows the fully expanded equations for cylindrical coordinates as implemented in our numerical codes. These equations have seven real eigenvalues consisting of: two fast magnetosonic waves $\lambda_{1,7} = v_x \mp v_{fm}$; two Alfvén waves $\lambda_{2,6} = v_x \mp v_A$; two slow magnetosonic waves $\lambda_{3,5} = v_x \mp v_{sm}$; and the entropy wave (contact discontinuity) $\lambda_4 = v_x$. The fast and slow magnetosonic waves are longitudinal waves whereas the Alfén wave is a transverse wave.

2.2.1 Viscosity, diffusivity, and the α prescription

If the plasma is non-ideal, then the viscosity and diffusion terms become important. The viscosity tensor has the form

$$V_{ij,\rm visc} = \eta_{\rm visc}\left(\partial_{x_j} v_i + \partial_{x_i} v_j\right) \tag{2.11}$$

where $\eta_{\rm visc}$ is the dynamic viscosity. The tensor is evidently symmetric. In cylindrical coordinates, the viscous tensor is

$$\boldsymbol{V}^{\rm cyl}_{\rm visc} = -\eta_{\rm visc}\begin{bmatrix} 2\partial_r v_r & r\partial_r\Omega + \partial_\phi v_r/r & \partial_z v_r + \partial_r v_z \\ & 2(\partial_\phi\Omega + v_r/r) & r\partial_z\Omega + \partial_\phi v_z/r \\ & & 2\partial_z v_z \end{bmatrix} . \tag{2.12}$$

For a typical Keplerian accretion disc, the $r\phi$ and $z\phi$ terms dominate. We assume that the disc varies slowly in the ϕ direction and we drop the ∂_ϕ terms as well.

In our simulations, we do not consider the effects of viscous heating or radiative cooling based on the expectation that the two processes are in thermal equilibrium and we take $Q = 0$. Rather, the main role of viscosity is to facilitate the transport of angular momentum outward through the disc, thereby permitting matter to accrete inward toward the star. However, the physical mechanisms which drive angular momentum transport in accretion discs are still poorly understood, especially in cold regions of the disc where the ionization fraction is low. In order to model the viscosity in our numerical models, we often take the Shakura and Sunyaev [1973] α-viscosity prescription

$$\nu_{\rm visc} = \alpha_{\rm v} c_s H = \alpha_{\rm v} \frac{c_s^2}{\Omega_K}, \tag{2.13}$$

where $\nu_{\rm visc} \equiv \eta_{\rm visc}/\rho$ is the kinematic viscosity, $\alpha_v = 10^{-4} - 0.1$ is the α-viscosity coefficient, $c_s^2 \equiv \gamma p/\rho$ is the sound speed, $H \equiv c_s/\Omega_K$ is the local disc height and Ω_K is the local Keplerian velocity. The turbulent magnetic diffusivity is estimated in a similar manner

$$\eta_{\rm diff} \equiv \frac{c^2}{4\pi\sigma} = \alpha_{\rm d} c_s H = \alpha_{\rm d} \frac{c_s^2}{\Omega_K}\,, \tag{2.14}$$

where σ is the conductivity and $\alpha_{\rm d} = 0.01 - 0.1$ is the α-diffusivity coefficient [Bisnovatyi-Kogan and Ruzmaikin, 1976].

2.2.2 The gravitational potential of the star and planet

In our models, the mass of the disc is assumed to be much less than the stellar mass and the contribution of the disc mass to the local gravitational potential is neglected. Thus for an accreting star, the local gravitational potential is simply

$$\Phi_* = -\frac{G\mathrm{M}_*}{|\boldsymbol{x}|}\,, \tag{2.15}$$

where $\boldsymbol{x}$ is the position vector. If there is an external perturber (such as a planet) in orbit around the star, the potential becomes

$$\Phi = -\frac{G\mathrm{M}_*}{|\boldsymbol{x}|} - \frac{GM_p}{(|\boldsymbol{x}-\boldsymbol{x}_p|^2+\epsilon^2)^{1/2}} + \frac{GM_p}{|\boldsymbol{x}_p|^3}\boldsymbol{x}\cdot\boldsymbol{x}_p\ , \tag{2.16}$$

where $\boldsymbol{x}_p$ is the position of the planet and ϵ is a smoothing radius which smooths over the singularity in the potential at the planet's position. Here, the first term represents the potential of the star, the second term represents the potential of the planet and the third term accounts for the fact that the coordinate system (which is centered on the star) is non-inertial due to the presence of the planet [Nelson et al., 2000, Fromang et al., 2005]. The corresponding gravitational acceleration is

$$\boldsymbol{g} = -\nabla\Phi = -\frac{G\mathrm{M}_*}{|\boldsymbol{x}|^3}\boldsymbol{x} - \frac{GM_p}{(|\boldsymbol{x}-\boldsymbol{x}_p|^2+\epsilon^2)^{3/2}}(\boldsymbol{x}-\boldsymbol{x}_p) - \frac{GM_p}{|\boldsymbol{x}_p|^3}\boldsymbol{x}_p\ . \tag{2.17}$$

This is utilized in §5 to investigate the migration of planets near a disc cavity.

2.2.3 Dimensionless units

Within the numerical code, the equations of MHD are reparametrized with normalized variables such that they can be solved in dimensionless form. To further simplify the equations, we also take $GM_* = 1$ and $\mathcal{R} = 1$. Solving the equations of MHD in dimensionless form is advantageous because it allows the solution to be scale-invariant and permits us to apply the results to a wide variety of accreting stars. For each dimensionless variable $\tilde{Q}$, the physical value Q can be recovered by multiplying by the corresponding reference unit, Q_0: $Q = \tilde{Q}Q_0$. The dimensionless re-parametrizations depend on the specific problem being solved and are described in depth in each respective chapter.

In the following chapters, all of the values are given in terms of the dimensionless units, except where explicitly assigned physical units.

2.3 The Godunov method

For any non-trivial initial condition, the equations of MHD are far too complex to solve analytically. Instead, the equations are solved numerically by spatially and temporally discretizing the conserved quantities in order to closely approximate the exact solutions at each moment in time. For the 1D MHD equations, the general procedure is as follows:

Specify the initial conditions. For each problem we study, we first specify the initial conditions for the state variables at $t = 0$

$$\boldsymbol{S}(x, t = 0) = [\rho(x, 0), p(x, 0), s(x, 0), \boldsymbol{v}(x, 0), \boldsymbol{B}(x, 0)]^T \tag{2.18}$$

and compute the corresponding vector of initial conserved variables $\boldsymbol{U}(x, t = 0)$ from these initial state variables. These initial conditions differ depending on the problem being solved. For accretion discs, the disc is initialized in hydrostatic equilibrium and the stellar and disc fields are separately specified. These are described in §2.5.

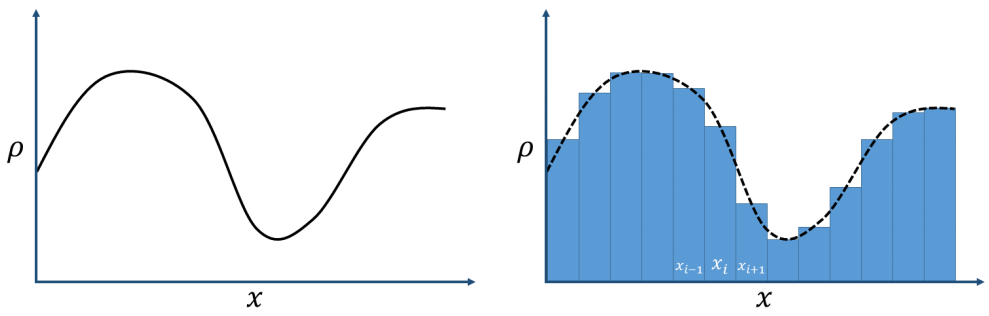

Figure 2.1: **Discretization of the initial conditions.** The left panel shows a schematic drawing of the initial conditions for the density. The right panel shows the piecewise discretized version of the initial conditions.

Discretize the simulation region. Next we discretize the spatial domain into N cells centered at $x_0, x_1, ..., x_{N-1}$ such that we have a grid with step size Δx. We spatially

discretize the conserved variables across the simulation region such that the values of the variables in each grid cell are piecewise constant (i.e. we average the functions over each cell to get the value for that cell)

$$\bar{\boldsymbol{U}}_i^0 = \frac{1}{x_{i+1/2} - x_{i-1/2}} \int_{x_{i-1/2}}^{x_{i+1/2}} \boldsymbol{U}(x, t = 0) dx \,. \tag{2.19}$$

Here the subscript i indicates the value corresponding to the i^{th} cell and the superscript 0 indicates that this is the 0^{th} timestep. This process is shown schematically in Figure 2.1.

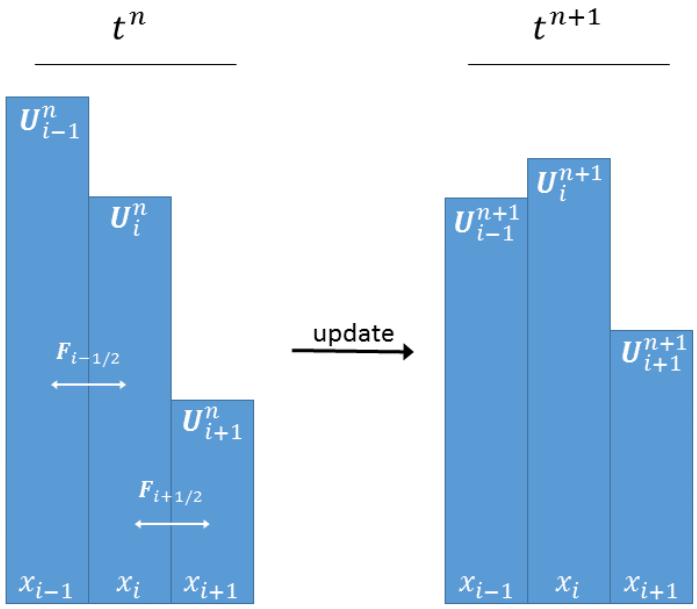

Figure 2.2: **Updating the conserved variables.** The fluxes between the cells are computed and used to update the states to the next timestep.

Compute the fluxes across the cell boundary. Now consider the i^{th} cell on the grid (centered at x_i) with two adjacent cells on either side centered at x_{i-1} and x_{i+1}. Since the discretized variables are piecewise constant in each cell, the values of the conserved

variables in these adjacent cells obey the step function

$$\boldsymbol{U}(x) = \begin{cases} \bar{\boldsymbol{U}}_{i-1} & \text{for } x < x_{i-1/2} \\ \bar{\boldsymbol{U}}_{i} & \text{for } x_{i-1/2} < x < x_{i+1/2} \\ \bar{\boldsymbol{U}}_{i+1} & \text{for } x_{i+1/2} < x \end{cases} , \tag{2.20}$$

where $x_{i-1/2}$ and $x_{i+1/2}$ are the locations of the boundaries between the cells (shown schematically in Figure 2.2). The discontinuities at each cell boundary resembles a local one-dimensional shock problem: therefore, the flux across the cell boundary at $x_{i+1/2}$ (i.e., $\boldsymbol{F}_{i+1/2}$) can be determined by solving the Riemann problem using $\boldsymbol{U}_i$ and $\boldsymbol{U}_{i+1}$ as initial values. The fluxes across the boundary $x_{i-1/2}$ can be determined analogously. Formulating the one-dimensional Riemann solver to compute the fluxes is a separate problem described later on in §2.4.2. In two and three-dimensional MHD problems, the fluxes are computed independently along each coordinate axis and combined to update the state.

Step forward in time. Given the fluxes $\boldsymbol{F}_{i-1/2}$ and $\boldsymbol{F}_{i+1/2}$ at the cell boundaries, we can step the conserved variables forward in time by Δt using the discretized form of Equation 2.9

$$\frac{\boldsymbol{U}_i^{n+1} - \boldsymbol{U}_i^n}{\Delta t} = \frac{\boldsymbol{F}_{i-1/2} - \boldsymbol{F}_{i+1/2}}{\Delta x} + \boldsymbol{Q} , \tag{2.21}$$

which can be more explicitly rewritten as

$$\boldsymbol{U}_i^{n+1} = \boldsymbol{U}_i^n + \frac{\Delta t}{\Delta x}[\boldsymbol{F}_{i-1/2} - \boldsymbol{F}_{i+1/2}] + \Delta t \boldsymbol{Q} . \tag{2.22}$$

This is illustrated in the right panel of Figure 2.2. By performing this procedure at all cell boundaries on the grid, the fluxes between the cells can be computed and used to update the state variables in each cell given a timestep [for an in-depth discussion, see Chapter 6 of Toro, 2009]. However, the algorithm which solves for the fluxes (i.e., solves the Riemann problem) at the cell boundaries must still be specified.

2.4 Solving the Riemann problem

2.4.1 An overview of the Riemann problem

The *Riemann problem* is the name for a general class of initial value problems consisting of a conservation equation (e.g. Equation 2.9) with piecewise constant initial conditions that have a single discontinuity at the origin

$$\boldsymbol{U}(x,0) = \begin{cases} \boldsymbol{U}_L & \text{if } x < 0 \\ \boldsymbol{U}_R & \text{if } x > 0 \end{cases} \tag{2.23}$$

One canonical example of a Riemann problem for the hydrodynamic Euler equations is the *shock tube problem* in which two gases with different pressures and densities sit in a tube separated by a wall or diaphragm. If the wall is suddenly removed, then there is an discontinuity at the origin which forms a wave system. The solution to the Riemann problem tells us how this wave system will evolve in time.

In the Godunov method, there is a discontinuity at the interface between every cell on the grid due to the discretization of the simulation region. Solving the Riemann problem at each interface permits us to compute the net flux into (or out of) the cell, thereby allowing us to update the variables in each cell in time.

The Riemann problem can be solved *exactly* for the Euler equations using a Newton-Raphson iteration scheme. However, for MHD problems, the computational expense of an analogous iterative method makes it intractable compared to faster approximate methods. In our codes, we utilize an approximate Riemann solver based on the HLLD Riemann solver first developed by Miyoshi and Kusano 2005 in order to solve the MHD equations [described in detail in Koldoba et al., August 2015]. Unlike Miyoshi and Kusano 2005, however, our Riemann solver solves the entropy conservation equation

instead of the energy conservation equation.

2.4.2 The Approximate Riemann Solver

Written out explicitly, the conservative variables and flux vectors in the one-dimensional ideal MHD equations take on the form

$$\boldsymbol{U} = \begin{pmatrix} \rho \\ \rho s \\ \rho v_x \\ \rho v_y \\ \rho v_z \\ B_y \\ B_z \end{pmatrix}, \quad \boldsymbol{F}(\boldsymbol{U}) = \begin{pmatrix} \rho v_x \\ \rho s v_x \\ \rho v_x^2 + p + (B_y^2 + B_z^2)/4\pi \\ \rho v_y v_x - B_x B_y/4\pi \\ \rho v_z v_x - B_x B_z/4\pi \\ v_x B_y - v_y B_x \\ v_x B_z - v_z B_x \end{pmatrix}. \tag{2.24}$$

For each coordinate axis on the grid, we independently solve the one-dimensional Riemann and combine the resulting fluxes at the end to update the cell values.

The Riemann Fan. The HLLD solver assumes five waves (and hence four intermediate states) in the Riemann fan separating the two initial states $\boldsymbol{U}_L$ and $\boldsymbol{U}_R$. The Riemann fan for our solver is diagrammed in Figure 2.3 which shows six states separated by the five waves which each correspond to one of the eigenvalues of the MHD equations §2.2. The HLLD solver exactly resolves: the contact discontinuity (entropy wave) which divides the left and right halves of the Riemann fan and propagates at velocity c; the two Alfvén waves propagating with speed a_L and a_R; and the two fast magnetosonic waves propagating at speeds b_L and b_R.

The solver assumes that these waves separate two initial states $\boldsymbol{U}_L$ and $\boldsymbol{U}_R$ and four

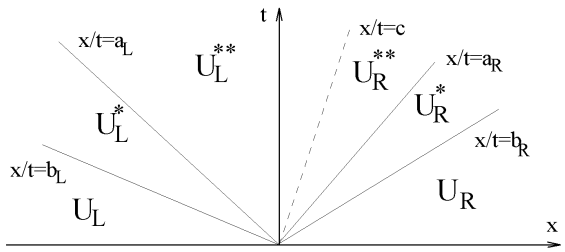

Figure 2.3: **The Riemann Fan.** The wave propagation diagram in the (x, t) plane for the HLLD solver [from Koldoba et al., August 2015].

intermediate states $\boldsymbol{U}_L^*, \boldsymbol{U}_L^{**}, \boldsymbol{U}_R^{**}, \boldsymbol{U}_R^*$ such that

$$\boldsymbol{U}(\xi) = \begin{cases} \boldsymbol{U}_L & \text{if } \xi \le b_L \\ \boldsymbol{U}_L^* & \text{if } b_L \le \xi \le a_L \\ \boldsymbol{U}_L^{**} & \text{if } a_L \le \xi \le c \\ \boldsymbol{U}_R^{**} & \text{if } c \le \xi \le a_R \\ \boldsymbol{U}_R^* & \text{if } a_R \le \xi \le b_R \\ \boldsymbol{U}_R & \text{if } b_R < \xi \end{cases}, \tag{2.25}$$

where $\xi = x/t$ is a self-similar wave-speed variable. These intermediate states are illustrated in the spacetime diagram shown in Figure 2.3. The Godunov intercell flux is defined as $\boldsymbol{F}_{i+1/2} \equiv \boldsymbol{F}(\boldsymbol{U}_{i+1/2}(0))$. Thus if the intermediate states are known, they can be used to compute the corresponding HLLD flux

$$\boldsymbol{F}_{i+1/2}^{\text{HLLD}} = \begin{cases} \boldsymbol{F}_L & \text{if } 0 < b_L \\ \boldsymbol{F}_L^* & \text{if } b_L \le 0 \le a_L \\ \boldsymbol{F}_L^{**} & \text{if } a_L \le 0 \le c \\ \boldsymbol{F}_R^{**} & \text{if } c \le 0 \le a_R \\ \boldsymbol{F}_R^* & \text{if } a_R \le 0 \le b_R \\ \boldsymbol{F}_R & \text{if } b_R < 0 \end{cases}. \tag{2.26}$$

The HLLD flux depends on the wave speeds between the adjacent cells as well as the values of the state variables in the intermediate states. In §2.4.3, we describe how the intermediate states are computed from $\boldsymbol{U}_L$ and $\boldsymbol{U}_R$.

The speeds of the left and rightmost waves are estimated in a manner similar to that prescribed by Davis [1988]

$$b_L = \min(0, v_{xL} - v_{fm,L}, v_{xR} - v_{fm,R}), \quad b_R = \max(0, v_{xL} + v_{fm,L}, v_{xR} + v_{fm,R}), \tag{2.27}$$

where

$$v_{fm} = \left(\frac{(v_A^2 + c_s^2) + \sqrt{(v_A^2 + c_s^2)^2 - 4\frac{B_x^2}{4\pi\rho} c_s^2}}{2} \right)^{1/2} \tag{2.28}$$

is the fast magnetosonic speed, $v_A = |B|/\sqrt{4\pi\rho}$ is the Alfvén speed and $c_s = \sqrt{\gamma p/\rho}$ is the sound speed. The velocity of the contact discontinuity c is estimated by applying the integral conservation laws over the Riemann fan

$$c = \frac{\left[\rho_L v_{xL}(v_{xL} - b_L) + (p_{\text{tot},L} - \frac{B_{xL}^2}{4\pi})\right] - \left[\rho_R v_{xR}(v_{xR} - b_R) + (p_{\text{tot},R} - \frac{B_{xR}^2}{4\pi})\right]}{\rho_L(v_{xL} - b_L) - \rho_R(v_{xR} - b_R)} \tag{2.29}$$

The jump conditions across the Alfvén waves can be solved if

$$a_{L/R} = c \mp \frac{|B_x|}{\sqrt{4\pi\rho^*_{L/R}}} \tag{2.30}$$

where the second term represents the Alfvén speed in the left or right state. It is assumed that $b_L \leq a_L \leq c \leq a_R \leq b_R$; if this condition is violated, a velocity correction is applied to b_R and b_L so that it satisfies the constraint. The correction procedure is described in depth in Koldoba et al. [August 2015].

2.4.3 Determining the intermediate states

We compute the values of the intermediate states ($\boldsymbol{U}^*_{L/R}$ and $\boldsymbol{U}^{**}_{L/R}$) and fluxes ($\boldsymbol{F}^*_{L/R}$ and $\boldsymbol{F}^{**}_{L/R}$) using the Rankine-Hugoniot jump conditions. For two discontinuous neighboring

states $\boldsymbol{U}_\alpha$ and $\boldsymbol{U}_\beta$ separated by a shock with speed S, the jump condition is simply

$$S = \frac{\boldsymbol{F}(\boldsymbol{U}_\beta) - \boldsymbol{F}(\boldsymbol{U}_\alpha)}{\boldsymbol{U}_\beta - \boldsymbol{U}_\alpha} \,. \tag{2.31}$$

Inserting the states and fluxes from Equation 2.25 and Equation 2.26 into Equation 2.31 gives

$$\begin{aligned}
\boldsymbol{F}_L^* &= \boldsymbol{F}_L + b_L(\boldsymbol{U}_L^* - \boldsymbol{U}_L) \\
\boldsymbol{F}_L^{**} &= \boldsymbol{F}_L^* + a_L(\boldsymbol{U}_L^{**} - \boldsymbol{U}_L^*) \\
\boldsymbol{F}_L^{**} &= \boldsymbol{F}_R^{**} + c(\boldsymbol{U}_L^{**} - \boldsymbol{U}_R^{**}) \\
\boldsymbol{F}_R^{**} &= \boldsymbol{F}_R^* + a_R(\boldsymbol{U}_R^{**} - \boldsymbol{U}_R^*) \\
\boldsymbol{F}_R^* &= \boldsymbol{F}_R + b_R(\boldsymbol{U}_R^* - \boldsymbol{U}_R) \,,
\end{aligned} \tag{2.32}$$

which relates the fluxes to the conserved variables in each state. Thus, the conservation law over the Riemann fan can be written as

$$\boldsymbol{F}_L - \boldsymbol{F}_R = c(\boldsymbol{U}_L^{**} - \boldsymbol{U}_R^{**}) - a_L(\boldsymbol{U}_L^{**} - \boldsymbol{U}_L^*) - b_L(\boldsymbol{U}_L^* - \boldsymbol{U}_L) + a_R(\boldsymbol{U}_R^{**} - \boldsymbol{U}_R^*) + b_R(\boldsymbol{U}_R^* - \boldsymbol{U}_R) \,. \tag{2.33}$$

In total, we have four unknown vectors, $\boldsymbol{U}_{L/R}^*, \boldsymbol{U}_{L/R}^{**}$, which must be solved for.

In the exact solution of the Riemann problem, the normal velocity is constant across the contact discontinuity. Similarly, in the HLLD solver, the normal velocities are assumed to be continuous across the Riemann fan such that

$$c = v_{xL}^* = v_{xL}^{**} = v_{xR}^{**} = v_{xR}^* \,. \tag{2.34}$$

Thus, the mass conservation term of the Rankine-Hugoniot relations can be rewritten as

$$\rho_\alpha = \rho_\beta \frac{S - v_{x\beta}}{S - v_{x\alpha}} \,, \tag{2.35}$$

where the α and β subscripts represent the values in the adjacent states. Combined with Equation 2.25 and Equation 2.34, this implies

$$\rho_L^* = \rho_L^{**} = \rho_L \frac{b_L - v_{xL}}{b_L - c} \qquad \text{and} \qquad \rho_R^* = \rho_R^{**} = \rho_R \frac{b_R - v_{xR}}{b_R - c} \,. \tag{2.36}$$

Similarly, the entropy conservation term in the Rankine-Hugoniot relations is

$$s_\alpha = s_\beta \frac{\rho_\beta (S - v_{x\beta})}{\rho_\alpha (S - v_{x\alpha})} \tag{2.37}$$

which combined with Equation 2.36 and Equation 2.34 gives

$$s_L = s_L^* = s_L^{**} \qquad \text{and} \qquad s_R = s_R^* = s_R^{**} \,. \tag{2.38}$$

Solving the y-momentum and y-induction jump conditions simultaneously gives

$$v_{yL}^* = v_{yL} + \frac{B_x B_{yL}}{4\pi} \frac{v_{xL} - c}{\rho_L^* (b_L - c)^2 - B_x^2/4\pi} \;\text{ and }\; B_{yL}^* = B_{yL} \frac{\rho_L (b_L - v_{xL})^2 - B_x^2/4\pi}{\rho_L^* (b_L - c)^2 - B_x^2/4\pi}. \tag{2.39}$$

Similarly, solving the z components gives

$$v_{zL}^* = v_{zL} + \frac{B_x B_{zL}}{4\pi} \frac{v_{xL} - c}{\rho_L^* (b_L - c)^2 - B_x^2/4\pi} \;\text{ and }\; B_{zL}^* = B_{zL} \frac{\rho_L (b_L - v_{xL})^2 - B_x^2/4\pi}{\rho_L^* (b_L - c)^2 - B_x^2/4\pi}. \tag{2.40}$$

The values for $v_{yR}^*, v_{zR}^*, B_{yR}^*$ and B_{zR}^* are analogous and can be found by substituting the subscript R in place of L in the above equations. The above equations fully specify $\boldsymbol{U}_L^*$ and $\boldsymbol{U}_R^*$.

To determine the transverse velocity and magnetic fields in the intermediate states $\boldsymbol{U}_L^{**}$ and $\boldsymbol{U}_R^{**}$, we consider the jump conditions across the contact discontinuity

$$c = \frac{\boldsymbol{F}(\boldsymbol{U}_L^{**}) - \boldsymbol{F}(\boldsymbol{U}_R^{**})}{\boldsymbol{U}_L^{**} - \boldsymbol{U}_R^{**}} \,. \tag{2.41}$$

For the magnetic field, we find

$$B_{yL}^{**} = B_{yR}^{**} \qquad \text{and} \qquad B_{zL}^{**} = B_{zR}^{**} \,, \tag{2.42}$$

which in turn implies that the transverse velocities are related by

$$v_{yL}^{**} = v_{yR}^{**} \qquad \text{and} \qquad v_{zL}^{**} = v_{zR}^{**} \,, \tag{2.43}$$

when $B_x \neq 0$. Since the left and right states are equal, we drop the L and R subscripts for these variables. Equation 2.42 and Equation 2.43 can be plugged into Equation 2.33

and solved to get

$$v_y^{**} = \frac{v_{yL}^* \sqrt{\rho_L^*} + v_{yR}^* \sqrt{\rho_R^*} + \sigma(B_{yR}^* - B_{yL}^*)/\sqrt{4\pi}}{\sqrt{\rho_L^*} + \sqrt{\rho_R^*}}, \tag{2.44}$$

$$v_z^{**} = \frac{v_{zL}^* \sqrt{\rho_L^*} + v_{zR}^* \sqrt{\rho_R^*} + \sigma(B_{zR}^* - B_{zL}^*)/\sqrt{4\pi}}{\sqrt{\rho_L^*} + \sqrt{\rho_R^*}}, \tag{2.45}$$

$$B_y^{**} = \frac{B_{yL}^* \sqrt{\rho_R^*} + B_{yR}^* \sqrt{\rho_L^*} + \sigma \sqrt{4\pi\rho_L^*\rho_R^*}(v_{yR}^* - v_{yL}^*)}{\sqrt{\rho_L^*} + \sqrt{\rho_R^*}}, \tag{2.46}$$

$$B_z^{**} = \frac{B_{zL}^* \sqrt{\rho_R^*} + B_{zR}^* \sqrt{\rho_L^*} + \sigma \sqrt{4\pi\rho_L^*\rho_R^*}(v_{zR}^* - v_{zL}^*)}{\sqrt{\rho_L^*} + \sqrt{\rho_R^*}}, \tag{2.47}$$

where $\sigma = \text{sign}(B_x)$ [Miyoshi and Kusano, 2005, Koldoba et al., August 2015]. We have now also fully specified $\boldsymbol{U}_L^{**}$ and $\boldsymbol{U}_R^{**}$. This set of equations allow us to compute the intermediate states $\boldsymbol{U}_L^*, \boldsymbol{U}_L^{**}, \boldsymbol{U}_R^{**}$ and $\boldsymbol{U}_R^*$ in the Riemann fan from the initial states $\boldsymbol{U}_L$ and $\boldsymbol{U}_R$ so long as $B_x \neq 0$. With all of the intermediate states specified, we utilize Equation 2.26 and Equation 2.32 to compute the HLLD flux for each cell on the grid.

2.4.4 Time integration

A two-step Runge-Kutta time integration scheme is utilized in our numerical code to step forward in time. The timestep Δt in the simulation is set by the Courant-Friedrichs-Levy (CFL) condition which limits the timestep by considering the wave-crossing time in all cells on the grid. The time integration proceeds in two stages: we first apply our HLLD solver to calculate the fluxes and update the state for a half timestep

$$\boldsymbol{U}_i^{n+1/2} = \boldsymbol{U}_i^n - \frac{\Delta t}{2\Delta x}\left(\boldsymbol{F}_{i+1/2}^n - \boldsymbol{F}_{i-1/2}^n\right) . \tag{2.48}$$

The intermediate half-timestep state, $\boldsymbol{U}_i^{n+1/2}$, is then used to compute the integral for the full timestep

$$\boldsymbol{U}_i^{n+1} = \boldsymbol{U}_i^n - \frac{\Delta t}{\Delta x}\left(\boldsymbol{F}_{i+1/2}^{n+1/2} - \boldsymbol{F}_{i-1/2}^{n+1/2}\right) , \tag{2.49}$$

where $\boldsymbol{F}_{i-1/2}^{n+1/2}$ and $\boldsymbol{F}_{i+1/2}^{n+1/2}$ are the HLLD fluxes computed from $\boldsymbol{U}_i^{n+1/2}$.

2.5 Initial and boundary conditions

The initial and boundary conditions of our models vary depending on the specific problem being studied and the grid geometry of the model. However, in general the accretion discs in our model share common high-level features. Here we discuss the high-level features which are common in most of the models; the specific details of each problem are discussed in the respective chapters.

2.5.1 Structure of accretion discs

In all of the models presented in this work, the disc is initially axisymmetric and in hydrostatic equilibrium. In order to specify the initial state of the disc, we must specify the density ρ, pressure p, and the velocity $\boldsymbol{v}$. We define the midplane values of density and pressure as power laws in the radial direction

$$\rho_{\text{mid}}(r) = \rho_{\text{disc}} \left(\frac{r}{r_0} \right)^{-n} , \qquad p_{\text{mid}}(r) = p_{\text{disc}} \left(\frac{r}{r_0} \right)^{-l} , \tag{2.50}$$

where ρ_{disc} and p_{disc} are the gas density and pressure at some reference radius r_0. Since the disc plasma is an ideal gas, we can relate the above quantities to the disc temperature using the ideal gas law

$$T_{\text{mid}}(r) = \frac{\mu m_p}{k_B} \frac{p_{\text{mid}}}{\rho_{\text{mid}}} = T_{\text{disc}} \left(\frac{r}{r_0} \right)^{n-l} \quad \text{where} \quad T_{\text{disc}} \equiv \frac{\mu m_p}{k_B} \frac{p_{\text{disc}}}{\rho_{\text{disc}}} . \tag{2.51}$$

The slopes of these profiles are given by

$$\frac{\partial p_{\text{mid}}}{\partial r} = -\frac{l}{r} p_{\text{mid}}(r) , \quad \frac{\partial \rho_{\text{mid}}}{\partial r} = -\frac{n}{r} \rho_{\text{mid}}(r) , \quad \frac{\partial T_{\text{mid}}}{\partial r} = \frac{n-l}{r} T_{\text{mid}}(r) . \tag{2.52}$$

Initially, the poloidal components of the velocity are small (i.e., $v_r = v_z = 0$) and the equation of motion (Equation 2.2) for the plasma in the accretion disc reduces to

$$\rho \boldsymbol{v} \cdot \nabla \boldsymbol{v} = -\rho \nabla \Phi - \nabla p , \tag{2.53}$$

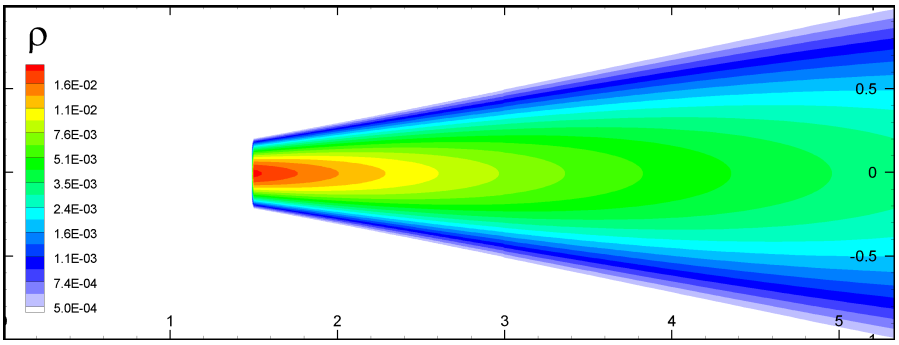

Figure 2.4: **Poloidal slice of the initial volume density for n = 1.5.**

where $\Phi(r, z) = -G\mathrm{M}_*/R$ is the gravitational potential of the star. The radial component of Equation 2.53 gives

$$\rho\frac{v_\phi^2}{r} = \rho\frac{G\mathrm{M}_*}{R^2}\frac{r}{R} + \frac{\partial p}{\partial r}\,. \tag{2.54}$$

Thus, the azimuthal velocity along the disc midplane is

$$v_\phi(r, z = 0) = \sqrt{\frac{G\mathrm{M}_*}{r} + \frac{r}{\rho}\frac{\partial p}{\partial r}} = \sqrt{\frac{G\mathrm{M}_*}{r} - l\frac{p_{\mathrm{mid}}(r)}{\rho_{\mathrm{mid}}(r)}}\,, \tag{2.55}$$

where we have plugged in the expression for the radial pressure gradient from Equation 2.52. In general, $l > 0$ and the disc is slightly sub-Keplerian due to the radial pressure support from the orbiting gas. The z-component of the equation of motion provides an expression for vertical hydrostatic equilibrium

$$\frac{\partial p}{\partial z} = -\rho\frac{G\mathrm{M}_*}{R^2}\frac{z}{R}\,.$$

A general solution to this equation takes the form

$$\begin{aligned}\rho(r, z) &= \rho_{\mathrm{mid}}(r)\exp\left(\frac{\Phi(r, 0) - \Phi(r, z)}{T_{\mathrm{mid}}(r)}\right),\\ p(r, z) &= p_{\mathrm{mid}}(r)\exp\left(\frac{\Phi(r, 0) - \Phi(r, z)}{T_{\mathrm{mid}}(r)}\right).\end{aligned} \tag{2.56}$$

A poloidal slice of this density profile is plotted in Figure 2.4 for $n = 1.5$. The entropy per unit mass can then be calculated from the initial density and pressure distributions $s = p/\rho^\gamma$.

2.5.2 Stellar magnetic fields

Young stars are expected to have highly convective interiors and can have strong magnetic fields up to a few kilogauss in magnitude. The magnetic topologies of these stars are often complex, consisting of combinations of non-aligned dipole, quadrupole and octupole components [Donati et al., 2007, 2008, Donati and Landstreet, 2009]. The dipole component of the field takes the form

$$\boldsymbol{B}_{\rm dip} = \frac{3(\boldsymbol{\mu}\cdot\boldsymbol{R})\boldsymbol{R} - \boldsymbol{\mu}R^2}{R^5}\,, \tag{2.57}$$

where $\boldsymbol{\mu}$ is the magnetic dipole moment of the star. This component is expected to play the most dominant role in the disc-magnetosphere interaction as the magnitude of the dipole component field falls off slower with distance compared to the higher order components. The disk may also be threaded by a large-scale ordered magnetic field separate from the stellar dipole. In our numerical code, the magnetic fields are split into a fixed dipole component and a current-induced component $\boldsymbol{B} = \boldsymbol{B}_{\rm dip} + \boldsymbol{B}_{calc}$ [Tanaka, 1994].

2.5.3 Boundary conditions

The boundary conditions of each model vary depending on the grid geometry on which the model is implemented as well as the specific problem being studied. In general, the problems which we investigate have an internal boundary on the star and an external boundary at the outer edges of the simulation region. The inner boundary on the stellar surface has free boundary conditions for the hydrodynamic variables (density, pressure and entropy) such that $d\ldots/dn = 0$ where n is the direction normal to the stellar surface. As we do not consider outflows due to stellar winds, matter is not permitted to leave the star by requiring that the poloidal velocity $v_p \leq 0$ at the stellar boundary. Additionally

we assume that the poloidal component of the magnetic field $\boldsymbol{B}_p$ is frozen to the surface of the star while the toroidal components obey free boundary conditions.

The fluid variables at the external boundaries obey free boundary conditions for all variables, except in the region adjacent to the accretion disc. At the external boundaries, we impose the condition that $v_p \geq 0$ so that no matter can flow back into the simulation region once it leaves. The boundaries in the disc region depend on the specific problem being investigated and are discussed in-depth in each respective chapter.

2.6 Grid geometries

The numerical codes have been implemented on several different grid geometries which are conducive to solving astrophysical problems. In general, the problems we study involve a dense accretion disc in orbit around a central star: these sorts of problems are well suited for coordinate systems with axial symmetry such as cylindrical or spherical coordinates. In this section, we describe several of the coordinate systems on which the solver is implemented.

2.6.1 Two-dimensional geometries

Figure 2.5 shows several two-dimensional geometries on which the solver is implemented. The leftmost panel shows an implementation of the axisymmetric spherical coordinate system $\boldsymbol{R} \equiv (R, \theta)$ where R is the spherical radius and θ is the polar angle. The axisymmetry condition implies that $\partial_\phi \ldots = 0$ for any variable computed on the grid. The grid is uniform in the polar direction and the size steps in the radial direction are chosen such that the poloidal-plane cells are curvilinear rectangles with approxi-

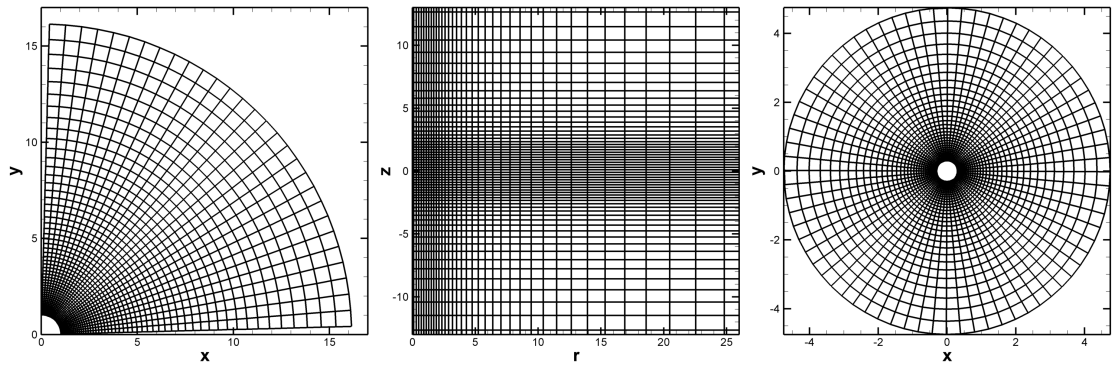

Figure 2.5: **Various 2D grid geometries.** *Left panel:* (R, θ) axisymmetric spherical coordinates; *Middle panel:* (r, z) axisymmetric cylindrical coordinates; *Right panel:* (r, ϕ) polar coordinates

mately equal lengths on each side. This choice results in high spatial resolution near the star where the disc-magnetosphere interaction takes place while also permitting a large simulation region. Unlike the other coordinate systems which utilize an HLLD-type solver, an entropy conserving Roe-type solver [analogous to that in Brio and Wu, 1988] is used to solve the equations of MHD. This coordinate system is useful for investigating the disc-magnetosphere interaction and has been used extensively to study winds and outflows launched from the disc-magnetosphere boundary [see §3, Romanova et al., 2004, 2005, Ustyugova et al., 2006, Romanova et al., 2009, Königl et al., 2011, Lii et al., 2012].

The middle panel of Figure 2.5 shows a grid based on axisymmetric cylindrical coordinates $\boldsymbol{r} \equiv (r, z)$ where r is the cylindrical radius and z is the distance from the midplane. Mesh compression is implemented on the grid such that the grid resolution at the midplane and near the star is higher than that far outside the disc midplane or far out in the disc. This enables us to more finely resolve the accretion dynamics in the regions of interest. As the grid resolution is quite high in the midplane, the fastest-growing MRI modes can be resolved, permitting us to study realistic accretion driven by the MRI

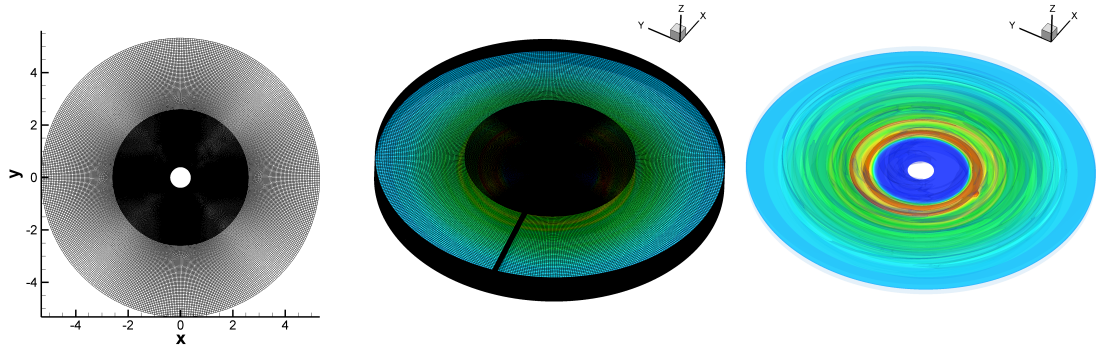

Figure 2.6: **The 3D cylindrical grid.** *Left panel:* the (r, ϕ) plane; *Middle panel:* *Right panel:*

turbulence [discussed in §4, Romanova et al., 2011, Lii et al., 2014] as well as outflow phenomena driven by the disc-magnetosphere interaction [Dyda et al., 2013, 2015a,b].

The rightmost panel of Figure 2.5 shows the grid in polar $\boldsymbol{r} = (r, \phi)$ coordinates. This grid is primarily aimed toward solving problems involving planet migration and solves the hydrodynamic equations for the surface density Σ instead of the volume density ρ. This grid has been used to study the migration of planets in a magnetized disc and near disc cavities [see §5, Comins et al., forthcoming, Lii et al., forthcoming].

2.6.2 The three-dimensional cylindrical code

In addition to the 2D geometries, we utilize a 3D grid in cylindrical $\boldsymbol{r} = (r, \phi, z)$ coordinates, shown in Figure 2.6. Unlike the 2D plane-polar grid, the 3D cylindrical grid has mesh compression in the region adjacent to the star to allow for finer resolution of the disc-magnetosphere interaction as well as planet migration in the inner regions of the disc. The leftmost panel of Figure 2.6 illustrates the mesh compression in the (r, ϕ) plane while the middle panel shows the structure of the grid in 3D. The rightmost panel

of Figure 2.6 shows a time snapshot from a simulation of a planet migrating in a disc with a central disc cavity [Lii et al., forthcoming]. Like the 2D polar grid, this coordinate system is well suited for solving problems involving planet migration as well as problems involving waves and warps in the disc.

2.7 Parallelization and computing facilities

The MHD codes are massively parallelized and optimized to run on many-processor systems. The code is parallelized by sub-dividing the grid into blocks in the radial and azimuthal directions (and vertical direction in the 3D cylindrical geometry). The computation for each block is assigned to a processor and the boundaries between adjacent blocks are synchronized at each timestep. A typical simulation run may use anywhere between 24 and 1024 processors, depending on the dimensions of the grid.

The data products from the simulations are output as unformatted binary files. The advantage of using a language agnostic binary format is that given the array sizes, the data products can be read into any language without the use of external libraries. Each data product may have a size ranging from a few MB to tens of GB in size depending on the scale of the problem being studied; the full datasets have corresponding sizes of a few hundred MB to a few TB. To minimize the storage costs, we perform on-the-fly analysis as the simulation is in progress and output the resulting data. This permits high time cadence measurements of quantities such as accretion and outflow rates or the torque on an orbiting planet without incurring the cost of storing many data files.

Most of the results shown in this work have been obtained using the NASA Center for Climate Simulation's Discover supercomputer and the NASA Advanced Supercomputing Division's Pleiades supercomputer. The data products are automatically down-

loaded from the supercomputing facilities to our local server every few hours where it is analyzed and archived. The local server is also used for the debugging and testing of the code.

CHAPTER 3

THE MAGNETIC LAUNCHING AND COLLIMATION OF JETS FROM THE DISC-MAGNETOSPHERE BOUNDARY

3.1 Background and overview

In this chapter, we discuss a mechanism for the launching and collimation of outflows during epochs of high accretion onto a magnetized star. In particular, we focus on young stars where accretion is known to occur in episodic bursts. The results shown in this chapter are presented in Lii et al. [2012].

Stars like the Sun are born out of dense clouds of gas and dust undergoing collapse due to their own self-gravity. In the early stages of collapse, the central protostar is orbited by a dense accretion disc and is enshrouded by a dense envelope which obscures the accretion dynamics near the young star. In these early stages, the accreting envelope has roughly the same mass as the nascent star. However, after a few million years, the mass of the envelope becomes depleted, the infalling material is cleared and the young disc-accreting star emerges from the obscuring cloud. Young stars with masses $M_* < 2M_\odot$ in this phase of evolution are known as classical T Tauri stars (cTTs), appellated after their prototype star T Tauri. This stage of protostellar evolution is observationally characterized by high variability as well as strong emission lines and infrared excesses which trace the disc accretion onto the star. These stars are often also accompanied by high velocity collimated outflows which emerge from the inner regions of their accretion discs. At the same time, planet formation and migration processes proceed in the accretion disc. The star remains in this stage for a few million years, before the disc is eventually photoevaporated away as the young star moves along the Hayashi track towards the main sequence.

Young stars produce strongly collimated high-speed outflows (jets) which are a key mechanism in transporting mass, energy and angular momentum out of the disc and facilitating accretion onto the young protostellar core. The formation of a collimated jet requires tandem launching and collimation mechanisms which are robust enough to explain the strongly collimated outflows observed in many young stellar systems. A number of theoretical models have been proposed to explain the mechanism which launches the matter from the disc [see review by Ferreira et al., 2006]. One class of launching mechanisms is the magnetocentrifugal driving mechanism in which the disc matter is accelerated up along inclined field lines from the inner few AU of the disc, resulting in an extended disc wind [Blandford and Payne, 1982, Königl and Pudritz, 2000]. A second class of models involves outflows driven from the the disc-magnetosphere boundary, either as an X-wind type outflow [Najita and Shu, 1994, Shu et al., 1994, Cai et al., 2008] or as a magnetically launched conical wind [Romanova et al., 2009]. The matter may also be magnetically launched from the inner disc [Lovelace et al., 1991] or launched from the star as a strong stellar wind [Matt and Pudritz, 2008]. Observations of stars with strong outflows show that the typical outflow velocities are of the order of the Keplerian velocity of the inner disc region, favoring the models where the outflow originates from the disc-magnetosphere boundary or the inner regions of the disc.

Recent observational evidence suggests that the helical magnetic field lines frozen into the rotating outflow can self-collimate the matter into a jet [Carrasco-González et al., 2010, Lovelace et al., 1987]. The outflow may also become collimated by interaction with a large-scale external poloidal field threading the disc [Matt et al., 2003, Fendt, 2009] or by interaction with a dense ambient medium surrounding the young star [Lovelace et al., 1991, Frank and Mellema, 1996, Carrasco-González et al., 2015].

Spectral measurements show that a significant number of cTTs's exhibit signs of out-

flows from their discs [Edwards et al., 2003, 2006, Gómez de Castro and von Rekowski, 2011] with early observations indicating a correlation between the outflow and mass accretion rates of cTTs's [Cabrit et al., 1990, Hartigan et al., 1995]. Surveys of nearby molecular clouds show that the observed accretion rates in many young stars are too low to account for the observed initial mass function, suggesting that accretion proceeds in episodic bursts [Evans et al., 2009, Enoch et al., 2009]. These sorts of episodic bursts are observed in FUor and EXor-type stars which exhibit outbursts in between epochs of quiescence [Herbig, 1977, 2007, 2008, Caratti o Garatti et al., 2011]. These sudden outbursts are believed to be associated with sudden rises in the accretion rate due to the infall of circumstellar material and are often accompanied by collimated outflows [Reipurth, 1985, Sandell and Weintraub, 2001]. Even with recent technological improvements to telescopes, direct imaging of the inner disc region is still hampered by the insufficient resolution of ground- and space-based observatories [see reviews by Ray et al., 2007, Frank et al., 2014] and observations have only recently shown that the jets become collimated at distances *less than* about 10 AU from the star [Hartigan et al., 2004, Coffey et al., 2008]. In lieu of direct imaging of the inner disc, astronomers have relied on numerical simulations to study the structure and dynamics of the disc-magnetosphere boundary.

Simulations Early simulations performed by Hayashi et al. [1996] and Miller and Stone [1997] achieved single-episode outflows from the disc-magnetosphere boundary lasting a few dynamical timescales. As simulations grew more sophisticated, longer runs performed by Goodson et al. [1997, 1999], Hirose et al. [1997], Matt et al. [2002]; and Küker et al. [2003] showed several episodes of field line inflation and outflows. However, none of these early simulations produced robust outflows which lasted long enough to establish the outflow behavior and dynamics. Long lasting outflows have

been achieved by treating the disc as a *boundary condition* and launching matter into the corona [e.g. Romanova et al., 1997, Ouyed and Pudritz, 1997, Ustyugova et al., 1999, Krasnopolsky et al., 1999, Fendt and Elstner, 2000, Matsakos et al., 2008, Fendt, 2009, Staff et al., 2010]. However, in order to understand the launching and collimation mechanisms of the outflows, the simulations must include a realistic, low-temperature accretion disc and solve the full magnetohydrodynamic (MHD) equations in both the disc and coronal space. Recently, there has been much work in this direction with the modeling of outflows launched from realistic discs threaded by large scale magnetic fields [Casse and Keppens, 2002, 2004, Zanni et al., 2007, Murphy et al., 2010].

Our group first obtained long lasting outflows from realistic accretion discs for the case of rapidly rotating stars in the propeller regime of accretion [Romanova et al., 2005, Ustyugova et al., 2006]. These simulations showed a two-component outflow in which most of the matter is carried away through a conical-shaped wind while most of the energy and angular momentum flows into a low-density, high-velocity axial jet. This axial jet is magnetically-dominated and well collimated by the toroidal magnetic field. More recently, we observed single-component, long lasting conical outflows in the more general case of slowly rotating stars Romanova et al. [2009]. The conical outflows are driven from the disc-magnetosphere boundary by magnetic pressure and unlike X-winds, these outflows do not require equality of the magnetospheric and corotation radii and can originate even from slowly rotating stars. However, the conical winds showed only weak collimation within the simulation region.

In this chapter, we present axisymmetric MHD simulations of long-lasting, collimated jets launched from the disc-magnetosphere boundary of a magnetized star with an aligned dipole. Building upon the previous work on conical winds by Romanova et al. [2009], we simulate an accretion disc with a higher accretion rate in a larger simulation

region and observe the emergence of a magnetically driven, magnetically collimated jet. In §3.2 we describe the numerical methods and initial and boundary conditions used in the simulations. Then, in §3.4, we give an overview of the simulations and describe the reference run which we use for analysis of the launching and collimation mechanisms. In §3.5 we describe the fluxes, velocities and forces in the jet and investigate the jet launching and collimation mechanisms. Lastly, in §3.6 we discuss the relation of this work to previous results as well as the application of our simulations to several types of rapidly accreting young stars.

3.2 The numerical model

Here, we briefly describe the main aspects of our numerical model. We utilize the axisymmetric Godunov-type code in the spherical coordinate system as described in detail in §2.6.1. The code includes the equations for viscosity and diffusivity in the plasma as described in §2.2.1 and is identical to the setup utilized in Romanova et al. [2009].

Grid The code uses a spherical coordinate system (r, θ, ϕ) where θ is the colatitude and ϕ is the azimuth angle. Axisymmetry imposes the additional condition $\partial/\partial\phi = 0$ on the equations of MHD[1]. Since we use a Godunov scheme, all numerically calculated variables are cell centered on the grid, except for the magnetic vector potential which is calculated on the nodes. The simulations are performed in the region $R_* < r < R_{\rm out}$, $0 \leq \theta \leq \pi/2$ and reflected across the axisymmetry axis for plotting (the "z-axis" in cylindrical coordinates). The grid is uniform in the θ direction and the size steps in the radial

[1]The equations of axisymmetric MHD in spherical coordinates can be found in Ustyugova et al. [2006].

direction are chosen such that the poloidal-plane cells are curvilinear rectangles with approximately equal lengths on each side. This choice results in high spatial resolution near the star where the disk-magnetosphere interaction takes place while also permitting a large simulation region. In the simulations presented in this paper, we choose the number of grids in the θ and r directions to be $N_\theta = 50$ and $N_r = 120$, respectively. This corresponds to $d\theta = \pi/N_\theta = 1.8^\circ$ and a total region radius of about 42 R_*. The smallest grid size at the surface of the star is $(\pi/100)R_*$ on a side.

3.2.1 Dimensionless variables

Within the numerical code, the equations of MHD are reparametrized with normalized variables (e.g. $\tilde{\rho} = \rho/\rho_0$, $\tilde{B} = B/B_0$, $\tilde{v} = v/v_0$, etc.) and solved in a dimensionless form. To further simplify the equations, we also take $GM_* = 1$ and $\mathcal{R} = 1$. The dimensionless equations permit us to apply the general results to a wide variety of accreting stars. Sample reference values for EX Lupi (EXor), FU Orionis (FUOR) and CTTS class stars are shown in Table 3.1. In order to convert the dimensionless units into real values, multiply the dimensionless value by the corresponding reference value in Table 3.1. For example, to calculate $\tilde{t} = 1000$ for a typical CTTS, multiply by the reference time ($t_{0,\mathrm{CTTS}}$ = 0.366 days) to get t = 366 days.

For the remainder of the chapter, all values and variables are given in terms of the normalized units (with tildes implicit) except where explicitly assigned physical units.

3.2.2 Numerical method

To numerically integrate the MHD equations, we split the physical processes into four blocks: (1) an “ideal MHD" block in which we calculate the dynamics of the plasma and magnetic field without dissipative processes; two “diffusion" blocks (2) and (3) in which we calculate the diffusion of the poloidal and azimuthal components of the magnetic field for frozen values of the plasma velocity and thermodynamic parameters (density and pressure); and a “viscosity" block (4) in which we calculate the viscous dissipation due to the $r\phi$ and $\theta\phi$ components of the viscous stress tensor. Integration of the equations in time is performed with a two-step Runge-Kutta method. To determine the fluxes between the cells, we use an approximate solution of the Riemann problem analogous to the Roe solver described in Brio and Wu [1988], except that we take the energy conservation equation in the entropy form. The dynamical variables are determined in the cells while the vector-potential of the magnetic field, A_ϕ, is determined on the corner nodes. We guarantee the absence of magnetic charge by calculating A_ϕ at each time step and then using it to obtain the poloidal components of the magnetic field (B_r, B_θ) in a divergence-free form [Tóth, 2000]. This ensures that the divergence-free condition $\nabla \cdot B = 0$ is always satisfied to within machine accuracy everywhere in the simulation region. We set a floor density of $\rho_{\rm flr} = 2.5 \times 10^{-7}$ throughout the simulation region to prevent the density from vanishing near the axis. While the jet is being launched, this adds a small amount of matter to the grids nearest the axis.

3.2.3 Boundary conditions

The external boundary at $R = R_{\rm out}$ is divided into a coronal region ($0 \leq \theta \leq \theta_d$) which has outflow boundary conditions and a disc region ($\theta_d \leq \theta \leq \pi/2$) which has inflow

boundary conditions. The disc height at the boundary is initially in hydrostatic equilibrium. Starting at $t = 0$, we permit low-temperature, high-density matter to flow in through the disc boundary region with a fixed density profile set by $\rho_{\rm d}$. The matter velocity along the disc boundary is set to be slightly sub-Keplerian such that $v_r < 0$ and the matter will flow into the simulation region. All other hydrodynamic variables have Neumann-type free boundary conditions in the disc region, $\partial_r \ldots = 0$.

In the coronal region, the boundary conditions are also free for all hydrodynamic variables. However, we prohibit matter from flowing into the simulation region from this portion of the boundary. We solve the transport equation for the magnetic flux function Ψ so that the magnetic flux flows out of the region together with matter.

The boundary conditions on the equatorial plane and on the rotation axis are symmetric and axisymmetric, respectively. Across the equator, the scalar variables are symmetric in z (e.g., $\rho(z) = \rho(-z)$) except for the vertical component of the velocity which is reflected $v_z(z) = -v_z(-z)$. On the axisymmetry axis, we enforce the axisymmetry boundary conditions by requiring that the toroidal variables obey $B_\phi(-r) = -B_\phi(r)$, $v_\phi(-r) = -v_\phi(r)$, et cetera. This imposes the explicit requirement that the toroidal variables must cross 0 on the axis. Nonetheless, we note that there is a region near the axisymmetry axis ($\theta = 0$ to θ_c) where the azimuthal angular velocity v_ϕ/r may take on spurious values. This can in turn result in spurious values of B_ϕ near the axis even though $B_\phi(\theta = 0) = 0$. However, these anomalous values do not affect the collimation of the jet. In our simulations θ_c spans about two polar grid cells or about 3.6°.

The inner boundary $R_{\rm in} = {\rm R}_*$ lies on the stellar surface. We assume that the radial component of the magnetic field is frozen to the surface of the star: B_r is held fixed while B_θ and B_ϕ obey the free boundary conditions $\partial_r B_\theta = 0$ and $\partial_r B_\phi = 0$. The plasma pressure and entropy also obey free boundary conditions on the stellar surface;

at each timestep, the density on the surface is recalculated from these two free variables. The matter velocity components are calculated using free boundary conditions and then adjusted to be parallel to the magnetic field vectors on the stellar surface. We do not consider outflows due to stellar winds and therefore we only permit matter to flow inward onto the star.

3.3 Reference Units

We take the reference mass M_0 to be the mass M_* of the star and the reference radius to be the radius of the star, $R_0 = R_*$. Time in units of $t_0 = 2\pi R_0/v_0$ (the Keplerian rotation period at $r = R_0$). The magnetic field is a dipole field and its value at the equator, B_*, is chosen such that the accretion disc (with typical accretion rates for young stars) can compress the magnetosphere almost to the stellar surface. The reference magnetic field is $B_0 = B_*/\mu$, where μ is the dimensionless magnetic moment. The reference velocity is $v_0 = (GM/R_0)^{1/2}$, the Keplerian velocity at the surface of the star. The reference force per unit mass is v_0^2/R_0. The reference density is taken to be $\rho_0 = B_0^2/v_0^2$. The reference temperature is $T_0 = P_0/(\mathcal{R}\rho_0) = v_0^2/\mathcal{R}$, where $\mathcal{R}$ is the gas constant. The reference mass accretion rate is $\dot{M}_0 = \rho_0 v_0 R_0^2$. The reference energy flux is $\dot{E}_0 = \dot{M}_0 v_0^2$. The reference angular momentum flux is $\dot{L}_0 = \dot{M}_0 v_0 R_0$. The reference current is $I_0 = cR_0B_0$. Table 3.1 shows examples of reference values for several different types of young accreting stars.

3.3.1 Turbulent viscosity and diffusivity

To estimate the turbulent viscosity ν_t, we adopt the Shakura and Sunyaev [1973] α model which approximates the viscosity coefficient as $\nu_t = \alpha_\nu c_s^2 \xi/\Omega_K$, where $c_s = (P/\rho)^{1/2}$ is

Table 3.1: **Reference units for three types of types of young, accreting stars.**

	cTTs	EXors	FU Ori
initial			
$M_*[M_\odot]$	0.8	0.8	0.5
R_* $[R_\odot]$	2	2	2.5
t_* [days]	1.90	1.90	3.37
B_* [G]	100	800	2500
derived			
R_0 [cm]	1.39×10^{11}	1.39×10^{11}	1.74×10^{11}
t_0 [days]	0.366	0.366	0.648
v_0 [cm s^{-1}]	2.76×10^{7}	2.76×10^{7}	1.95×10^{7}
B_0 [G]	10	100	250
f_0 [dynes/gm]	5.48×10^{3}	5.48×10^{3}	2.19×10^{3}
I_0 [G cm^2/s]	2.09×10^{22}	1.67×10^{23}	6.52×10^{23}
I_0 [A]	6.96×10^{12}	5.57×10^{13}	2.18×10^{14}
ρ_0 [g cm^{-3}]	1.31×10^{-13}	8.39×10^{-11}	1.64×10^{-10}
n_0 [cm^{-3}]	7.83×10^{10}	5.01×10^{12}	9.79×10^{13}
$\dot{M}_0$ [$M_\odot$ yr^{-1}]	1.11×10^{-9}	7.12×10^{-8}	1.54×10^{-6}
$\dot{E}_0$ [erg s^{-1}]	5.35×10^{31}	3.43×10^{33}	3.70×10^{34}
$\dot{L}_0$ [erg s^{-1}]	2.70×10^{35}	1.73×10^{37}	3.29×10^{38}
T_d [K]	9178	9178	4589
T_c [K]	9.18×10^{6}	9.18×10^{6}	4.59×10^{6}

the isothermal sound speed and Ω_K is the Keplerian angular velocity. Unlike the viscosity presented in §2.2.1, the density threshold coefficient ξ is included in order to turn off the viscosity in the non-accreting low-density regions outside the disc where the MRI (which provides the viscosity in the disk) is not efficient. We similarly estimate the turbulent diffusivity coefficient in Equation 2.5 and Equation 2.14 as $\eta_{\rm diff} = \alpha_d c_s^2 \xi / \Omega_K$ [Bisnovatyi-Kogan and Ruzmaikin, 1976]. Both α_v and α_d are dimensionless coefficients which are treated as parameters in our model. The coefficient ξ sets a density threshold for the viscosity and diffusivity

$$\xi = \begin{cases} 0 & \text{if } \rho \leq \rho_{\rm d}/4 \\ \frac{\rho - \rho_{\rm d}/4}{\rho_{\rm d} - \rho_{\rm d}/4} & \text{if } \rho_{\rm d}/4 < \rho \ < \rho_{\rm d} \\ 1 & \text{if } \rho \geq \rho_{\rm d} \end{cases} \tag{3.1}$$

where ρ_d is the disc density parameter at the external boundary (see Table 3.2). The density threshold coefficient ξ varies between 0 to 1 and acts to smoothly "turn on" viscosity and diffusivity for regions with $\rho > \rho_d/4$. Figure 3.1 shows the viscosity

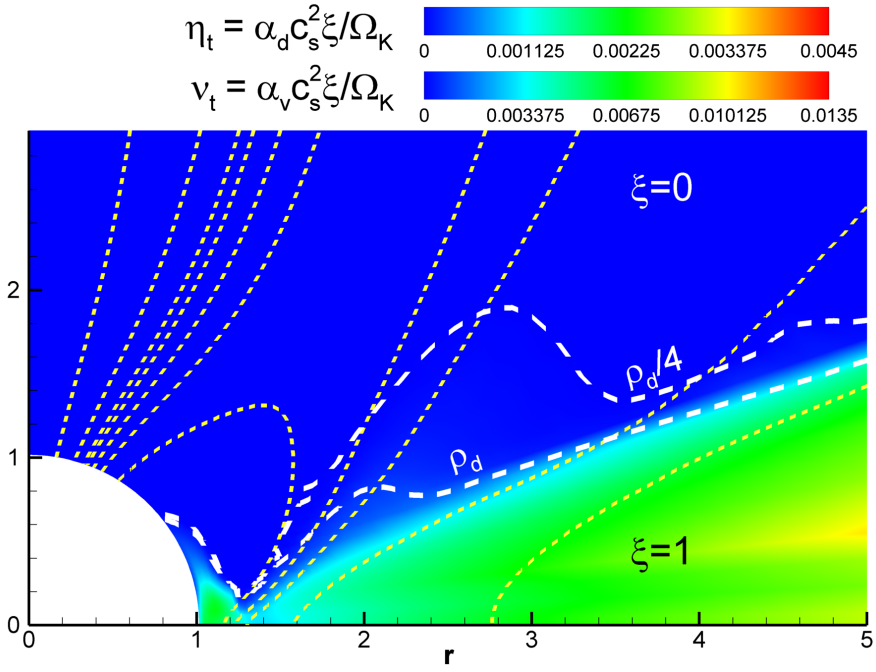

Figure 3.1: **Zoomed-in plot of the diffusivity and viscosity profiles near the star at t = 860.** In the $\xi = 0$ region, the turbulent viscosity ν_t and diffusivity η_t are turned-off. Above the $\rho_d/4$ density threshold, both are smoothly turned on as $\xi \rightarrow 1$ and we solve the non-ideal MHD equations in the disc.

and diffusivity profiles of the inner disc of the reference simulation at $t = 860$. The reference case uses coefficents of $\alpha_d = 0.1$ and $\alpha_\nu = 0.3$ for the turbulent diffusivity and viscosity. At each timestep, the turbulent diffusivity and viscosity profiles are evolved and reapplied to every point on the grid to ensure self-consistency of the simulation. Above the $\rho_d/4$ ($\xi > 0$) threshold, viscosity becomes important and we include η_t and ν_t by numerically integrating the non-ideal MHD equations using an explicit conservative Godunov-type numerical scheme. Outside the disc where the density is low, $\xi = 0$ and we solve the equations of ideal MHD.

Table 3.2: **Summary of model parameters.** All cases shown produce well collimated jets. The bolded line is the reference case which we use for analysis in this paper.

N_θ, N_r	α_ν	α_d	$\rho_{\rm d}$	$\rho_{\rm c}$	$R_{\rm out}$	μ
30, 55	0.3	0.1	5	10^{-3}	16.5	3
30, 66	0.3	0.1	0.1	10^{-4}	27	10
30, 66	0.3	0.1	1	10^{-3}	27	10
30, 66	0.3	0.1	10	10^{-3}	27	10
30, 66	0.3	0.1	1	10^{-3}	27	10
30, 66	0.6	0.3	10	10^{-3}	27	10
30, 80	0.3	0.1	10	10^{-3}	58	10
30, 80	0.6	0.3	10	10^{-3}	58	10
50, 100	0.3	0.1	5	10^{-3}	22	10
50, 100	0.3	0.1	10	10^{-3}	22	10
50, 120	0.3	0.03	5	10^{-3}	42	10
50, 120	0.3	0.1	3	10^{-3}	42	10
50, 120	0.3	0.1	5	10^{-3}	42	3
50, 120	**0.3**	**0.1**	**5**	$\mathbf{10^{-3}}$	**42**	**10**
50, 120	0.3	0.1	5	10^{-3}	42	15
50, 120	0.3	0.1	5	10^{-3}	42	25
50, 120	0.3	0.1	10	10^{-3}	42	10

3.4 Results

In order to investigate formation of jets from the disc-magnetosphere boundary, we perform dozens of simulations with varying initial parameters and grid sizes. The simulations have a total of 5 free parameters: α_ν and α_d, the dimensionless viscosity and diffusivity coefficients; $\rho_{\rm d}$ and $\rho_{\rm c}$, the densities of the disc and corona at the outer boundary; and μ, the stellar magnetic dipole moment. A sample of the runs which successfully produced strongly collimated jet-like outflows is shown in Table 3.2.

We observe three general classes of outflows: one-time episodic outflows, stable weakly collimated conical-type outflows, and stable collimated jets. The one-time episodic outflows occur when the accreting matter strongly compresses the stellar field

lines, driving transient outflows from the disc-magnetosphere boundary. In this case, the matter and magnetic pressures quickly re-equilibrate, halting the driving mechanism and suppressing the outflow. The conical winds are similar to those previously studied in Romanova et al. [2009] and are driven by the compressed magnetic field at the disc-magnetosphere boundary. In this chapter, we are interested in particular in the last class of observed outflow: the stable collimated jet.

3.4.1 Strongly collimated outflows

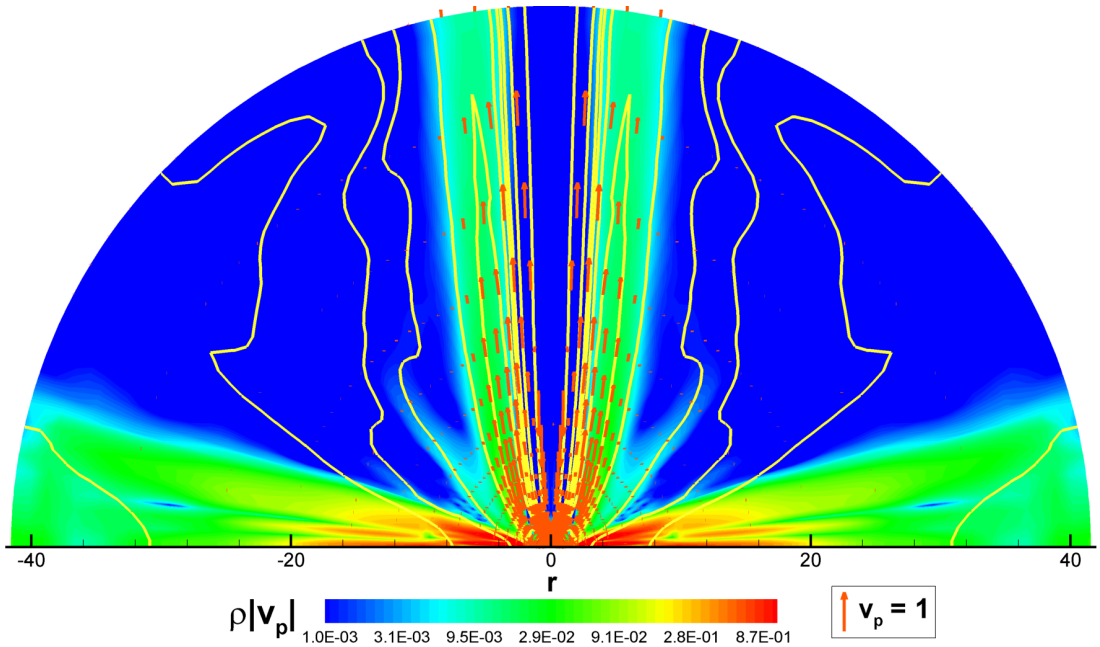

Figure 3.2: **The jet at time** $t = 860$**.** The background shows the poloidal matter flux density $\rho \left|\mathbf{v}_p\right|$ and the lines show contours of the magnetic flux function Ψ which is a proxy for the poloidal magnetic field. The red vectors show the poloidal matter velocity $\mathbf{v}_p$.

Figure 3.2 shows one of the simulations which produces a strongly collimated jet: throughout the remainder of the chapter, we will use this run as a reference case to perform additional analysis. The background contours represent the poloidal matter

flux $\rho\left|\mathbf{v}_p\right|$ and the lines represent contours of the magnetic flux function Ψ, which obeys the relation $\boldsymbol{B} \cdot \nabla\Psi = 0$. In the poloidal plane, therefore, the Ψ contours represent the poloidal magnetic field lines. The reference simulation uses a spherical grid with $N_\theta = 50$ cells in the θ direction and $N_r = 120$ cells in the radial direction with the parameters: $\alpha_v = 0.3$, $\alpha_d = 0.1$, disc density $\rho_{\rm d} = 5$, and coronal density $\rho_{\rm c} = 0.001$ (a summary of the parameters is shown as the bolded line in Table 3.2). For analysis of the launching and collimation mechanisms, we study the simulation at $t = 860$ when the jet is well established.

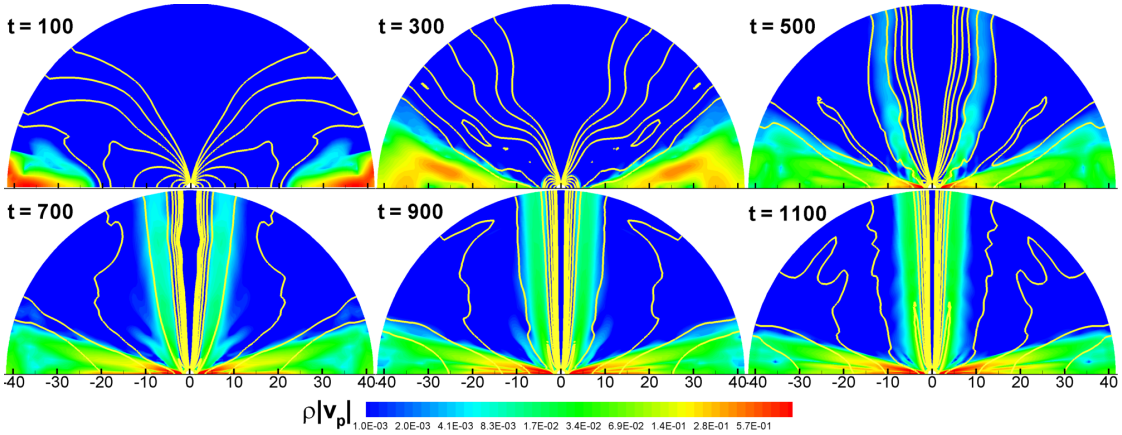

Figure 3.3: **Formation and collimation of the jet at different times t.** The $\rho\left|\mathbf{v}_p\right|$ background contour and field lines are plotted on the same scale as the contours in Figure 3.2.

Figure 3.3 shows snapshots of the reference simulation at six moments in time At $t = 100$, the matter flowing in from the boundary begins compressing and inflating the dipole field around the star. By $t = 300$, the disc is only a few stellar radii away from the star; the close proximity of the disc permits matter to accrete directly onto the star by flowing along the closed dipole field lines. At the same time, the inflated field lines in the corona undergo forced reconnection, ejecting plasmoids into the stellar corona.

The strong magnetic gradient at the disc-magnetosphere boundary launches matter

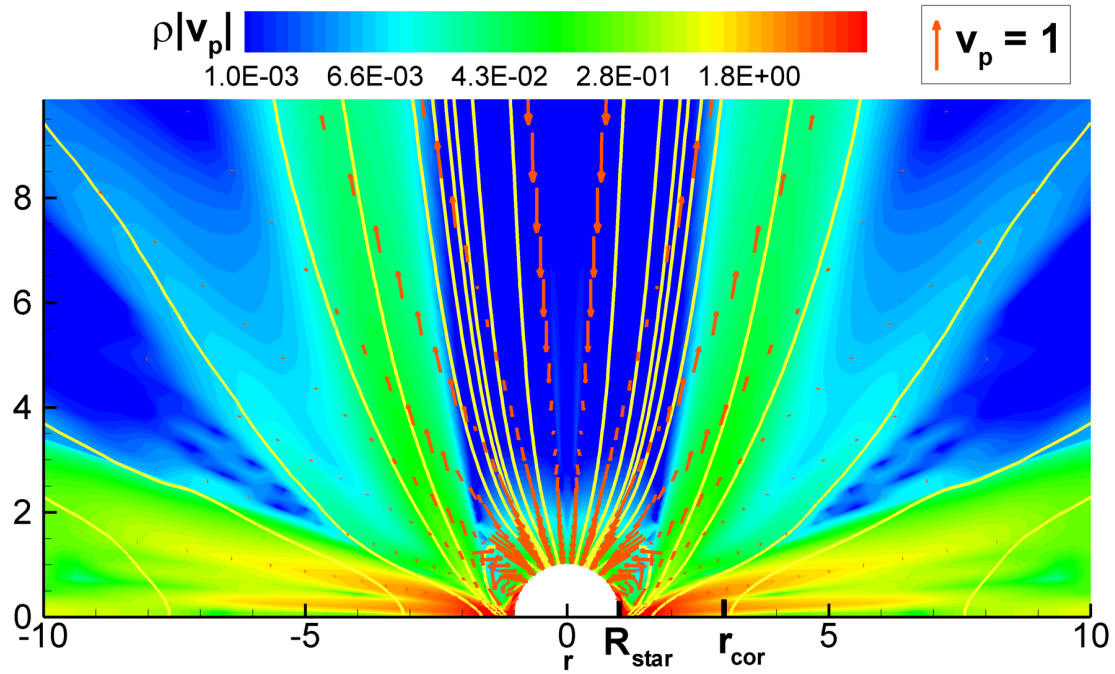

Figure 3.4: **A zoomed-in plot of the inner disc region at the time** $t = 860$**.** The plotted contours show the same scales as in Figure 3.2.

along the inflated dipole field lines. The outflow first emerges from the open field lines at the disc-magnetosphere boundary starting around $t = 350$ and becomes stable and well established by $t = 500$. As the jet stabilizes, the magnetic reconnection within the jet halts and the matter flows smoothly. Figure 3.4 shows a zoomed-in view of the outflow at $t = 860$, illustrating the proximity of the launching region to the star. As the outflow becomes stronger, we observe a gradual magnetic collimation of the outflowing matter into a jet (see frames $t = 700$ to $t = 1100$ of Figure 3.3).

Figure 3.5 shows a three-dimensional rendering of the jet at $t = 860$. Three poloidal matter flux surfaces are shown along with tightly wound helical magnetic field lines—represented by the red ribbons—which play a key role in collimating the outflow (this is discussed later in §3.5.3). The jet has the shape of an inverted tapered cone with a cylindrical radius of $1 - 4\ R_*$ at the base of the jet and $3 - 8\ R_*$ at the top. For this

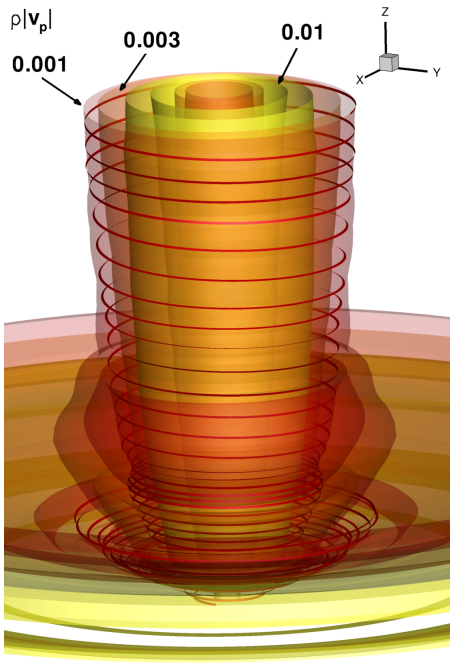

Figure 3.5: **3D view of the poloidal matter flux density $\rho\left|\mathbf{v}_p\right|$ contours of the jet at $t = 860$.** Three matter flux density surfaces are plotted: $\rho\left|\mathbf{v}_p\right|$ = 0.001, 0.003, and 0.01. The red streamtraces show the strongly wound magnetic field lines in the corona of the star which collimate the outflowing matter.

reference case, we measure a half-opening angle of $\Theta \approx 4^\circ$ at the top of the simulation region.

3.4.2 Properties of the outflow

In order to describe the relative magnitudes of the matter and magnetic pressures around the star, we use the standard plasma parameter β and the kinetic plasma parameter β_1:

$$\beta = \frac{p}{B^2/8\pi}, \qquad \beta_1 = \frac{p + \rho\mathbf{v}^2}{B^2/8\pi}. \tag{3.2}$$

The kinetic plasma parameter β_1 takes into account the ram pressure of the gas, $\rho\mathbf{v}^2$ in addition to the thermal gas pressure, p. Regions with $\beta, \beta_1 \gg 1$ are matter pressure

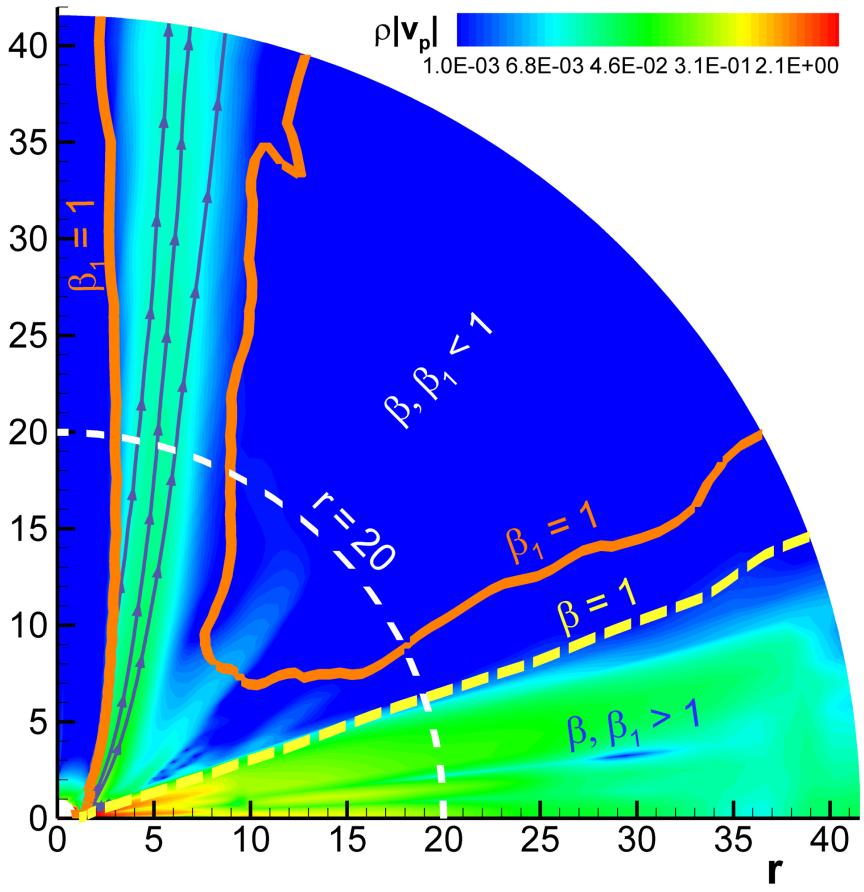

Figure 3.6: $\rho\left|\mathbf{v}_p\right|$ **contours overplotted with the** $\beta = 1$ **and** $\beta_1 = 1$ **lines.** The region interior to the β_1 line is matter dominated. The dashed white line shows the radius where the θ cross-sections shown in Figure 3.7 are taken. Also plotted are a few of the velocity streamlines in the jet.

dominated while regions with $\beta, \beta_1 \ll 1$ are dominated by the magnetic pressure. Figure 3.6 shows the $\beta, \beta_1 = 1$ lines for the $t = 860$ reference case. The conventional plasma parameter β is much less than unity everywhere except within the disc; hence if we use the plasma β criterion, we find that the jet is completely magnetically dominated. However, if the ram pressure is taken into account and β_1 is used instead, then we find that $\beta_1 \gtrsim 1$ inside the jet: in other words, the magnetic pressure is only a few times smaller than (or comparable to) the effective matter pressure, indicating that the magnetic field is important in driving and collimating the jet even at large distances from the star.

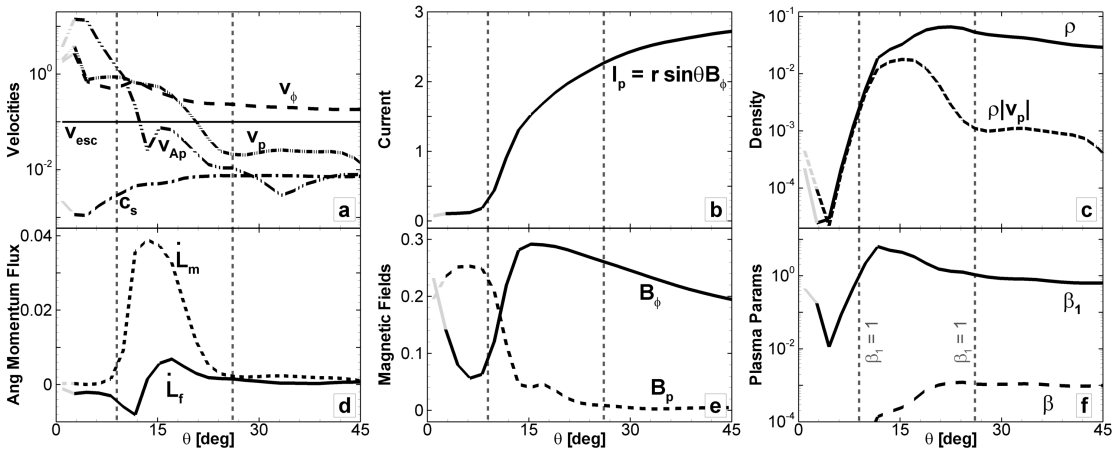

Figure 3.7: **Cross-sections of the jet in the θ direction at $r = 20$ and $t = 860$ (shown as dashed line in Figure 3.6).** The dashed vertical lines indicate the β_1=1 surfaces which approximately represent the boundaries of the jet. We indicate the region where numerical artifacts may play a role by greying out the two grids closest to the axis. **Panel (a)** shows the velocity cross-section in the jet. v_ϕ and v_p are the velocities in the toroidal and poloidal directions, respectively; $v_{\rm esc}$ is the escape velocity at $r = 20$; c_s is the sound speed; and $v_{\rm Ap}$ is the poloidal Alfvén speed. **Panel (b)** shows the poloidal current I_p in the jet. **Panel (c)** shows the density ρ and matter flux $\rho\left|\mathbf{v}_p\right|$ profiles in the jet. **Panel (d)** shows $\dot{L}_m$ and $\dot{L}_f$, the angular momentum fluxes from matter and magnetic fields, respectively. **Panel (e)** plots the magnetic field components in the poloidal B_p and toroidal B_ϕ directions. And lastly, **Panel (f)** shows the plasma β parameters in the jet (described in Equation 3.2).

Figure 3.7 shows cross-sections of the jet in the θ direction for angles $\theta = 0°$–$45°$ at the surface $r = 20$ (shown in Figure 3.6). The dashed vertical lines represent the $\beta_1 = 1$ surfaces which *approximately* delimit the boundaries of the jet. We indicate the region where numerical artifacts may play a role by greying out the two grids closest to the axis. Figure 3.7f shows the β and β_1 profiles of the jet, with $\beta \approx 10^{-4} - 10^{-3}$ and $\beta_1 \approx 1 - 6$ inside, indicating that the jet is "weakly" matter dominated. Figure 3.7a shows the velocity cross-section of the jet: within the jet, the matter is supersonic and the poloidal matter velocity v_p is larger than the poloidal Alfvén speed $v_{\rm Ap} = |\mathbf{B}_p|/\sqrt{4\pi\rho}$,

except at the left edge of the jet where they are comparable. The poloidal velocities in the jet range from $v_p \approx 1$ on the inner edge of the jet to $v_p \approx 0.1$ on the outer edge.

Panel 3.7a also shows that the toroidal matter velocity v_ϕ is very large even outside the jet, contributing to the winding of the magnetic field lines in the corona. Figure 3.7b shows the profile of the normalized poloidal current $I_p = r \sin\theta B_\phi$ flowing out of the simulation region through the jet (see §3.6.1 for analysis of the current flow). Figs. 3.7c and 3.7d show the matter and angular momentum flux profiles in the jet: the angular momentum transport is dominated by the outflowing matter[2] (this is further discussed in §3.5.1). Panel 3.7e shows the magnetic field distribution; note that the toroidal field is much larger than the poloidal field everywhere except on the inside edge of the jet, where we observe spurious values of B_ϕ. Note, however, that the collimating magnetic force is proportional to the transverse gradient of $I_p^2 = (r \sin\theta B_\phi)^2$ which is well behaved near the symmetry axis, as shown in Figure 3.7b [Lovelace et al., 1989]. Therefore, the axis values of B_ϕ do not affect the collimation of the jet. Rather, the dominant collimating force arises far from the axis between $\theta \sim 5-15^\circ$ where both B_ϕ and I_p are well behaved. The gradients of $(r \sin\theta B_\phi)^2$ and $\boldsymbol{B}_{\rm p}^2$ both contribute to the magnetic force and in §3.5.3, we discuss in detail how these magnetic fields launch and collimate the outflow.

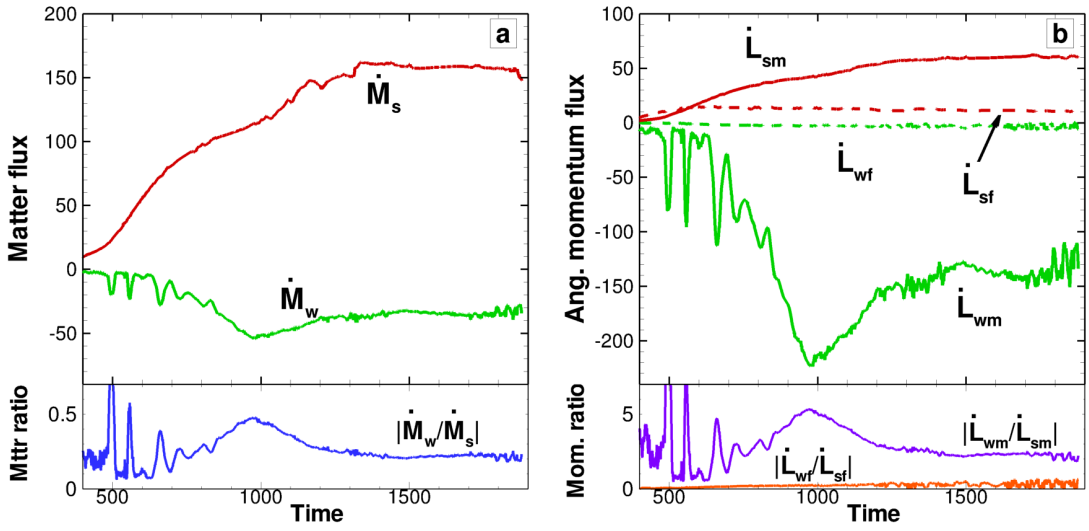

Figure 3.8: **Matter and angular momentum fluxes onto the star and into the outflow.** *Panel (a)*: Matter flux from the disc onto the star $\dot{M}_s$ and into the jet $\dot{M}_w$ as a function of time. The bottom plot shows the absolute value of the ejection-to-accretion ratio $|\dot{M}_w/\dot{M}_s|$ as a function of time. *Panel (b)*: Angular momentum flux rates added onto the star by matter $\dot{L}_{sm}$ and by the magnetic fields $\dot{L}_{sf}$. Also plotted is the angular momentum loss rate due to matter carried away by the jet $\dot{L}_{wm}$ and by the magnetic fields $\dot{L}_{wf}$. The bottom plot shows the ratios of angular momentum fluxes leaving in the jet to the angular momentum fluxes onto the star.

3.5 Fluxes, forces, and velocities in the jet

3.5.1 Matter and angular momentum flux

Matter flux

To measure the total accretion rates, we integrate the the matter and angular momentum fluxes over the star's surface ($r = 1$) and over a surface at $r = 20$. The mass accretion

[2]In contrast, the opposite is true at small radii ($r \lesssim 5$) and angular momentum is primarily transported away by the magnetic field.

rate through a given surface is given by

$$\dot{M} = \int d\mathbf{S} \cdot \rho \mathbf{v}_p = \int dS \rho v_r \,, \tag{3.3}$$

where $d\mathbf{S}$ is an outward facing surface area element and v_r is the radial component of the velocity. On the stellar surface, we measure the accretion rate $\dot{M}_\mathrm{s}$ by only considering the inward ($v_r < 0$) matter flux; conversely, for the outer surface at $r = 20$, we measure the outflow rate in the jet $\dot{M}_\mathrm{w}$ by only considering the outward $v_r > 0$ matter flux. Figure 3.8a shows the inward $\dot{M}_\mathrm{s}$ across the stellar surface and outward $\dot{M}_\mathrm{w}$ across the $r = 20$ surface as a function of time. The total matter flux onto the star $\dot{M}_\mathrm{s}$ slowly increases from the time the disc first reaches the star ($t = 300$) until it stabilizes around $t = 1300$. Similarly, the total matter flux through the jet stabilizes slightly earlier at $t = 1200$.

Angular momentum flux

The angular momentum flux density consists of three components: angular momentum carried by the matter $\mathbf{F}_\mathrm{Lm}$, by the magnetic field $\mathbf{F}_\mathrm{Lf}$, and by viscous transport $\mathbf{F}_\mathrm{Lv}$. The total angular momentum flux density is therefore

$$\mathbf{F}_\mathrm{L} = \mathbf{F}_\mathrm{Lm} + \mathbf{F}_\mathrm{Lf} + \mathbf{F}_\mathrm{Lv},$$

where

$$\mathbf{F}_\mathrm{Lm} \equiv r \sin\theta \rho v_\phi \mathbf{v}_p \,, \quad \mathbf{F}_\mathrm{Lf} \equiv -r \sin\theta \frac{B_\phi \mathbf{B}_p}{4\pi} \,, \quad \mathbf{F}_\mathrm{Lv} \equiv -\nu_t \rho (r \sin\theta)^2 \nabla\Omega \,, \tag{3.4}$$

with the last term non-zero only inside the disc. As with the matter flux, we integrate the angular momentum fluxes at the star ($r = 1$) and at the $r = 20$ surface,

$$\dot{L} = \int d\mathbf{S} \cdot \mathbf{F}_\mathrm{L} = \int d\mathbf{S} \cdot (\mathbf{F}_\mathrm{Lm} + \mathbf{F}_\mathrm{Lf} + \mathbf{F}_\mathrm{Lv}). \tag{3.5}$$

Figure 3.8b shows the integrated angular momentum flux as a function of time. $\dot{L}_{sm}$ and $\dot{L}_{sf}$ measure the angular momentum being *added* to the star by matter and magnetic

fields, respectively. The accreting matter adds angular momentum directly ($\dot{L}_{sm}$) and spins up the star. The magnetic fields also allow the matter to spin up the star indirectly: the magnetospheric radius $r_m \approx 1.1$ (calculated by equating the magnetic and gas pressure in the disc) is smaller than the corotation radius $r_{cor} = 3$ and hence the inner disc drags the stellar dipole field, causing the star to spin up at a nearly constant rate ($\dot{L}_{sf}$).

At the surface at $r = 20$, only the outward angular momentum carried by the jet is calculated. The outward angular momentum transport due to magnetic fields, $\dot{L}_{\rm wf}$, is negligible compared to the the angular momentum being carried away by the matter, $\dot{L}_{\rm wm}$. Like the matter flux, the angular momentum flux in matter becomes steady around $t = 1200$. Roughly a third of the disc's angular momentum exits the system through the jet, while only a small fraction of the incoming angular momentum is added to the star. The majority of the disc's angular momentum is transported by viscosity back and out through the disc itself.

3.5.2 Velocities in the jet

Figure 3.6 shows a few of the velocity streamlines flowing from the base of the jet to the edge of the simulation region. The figure shows that the launching region of the jet is localized to the very inner disc. To probe the structure of the jet in detail, we analyze the velocities within the jet at $t = 860$. Figure 3.9 shows velocities along a representative field line running through the jet. The field line originates from the disc at $r = 1.24$ and extends upward through the jet to the outer boundary of the simulation region (for a visual representation, see the denoted field line in Figure 3.10).

We define the new coordinate s which traces the linear distance along the poloidal

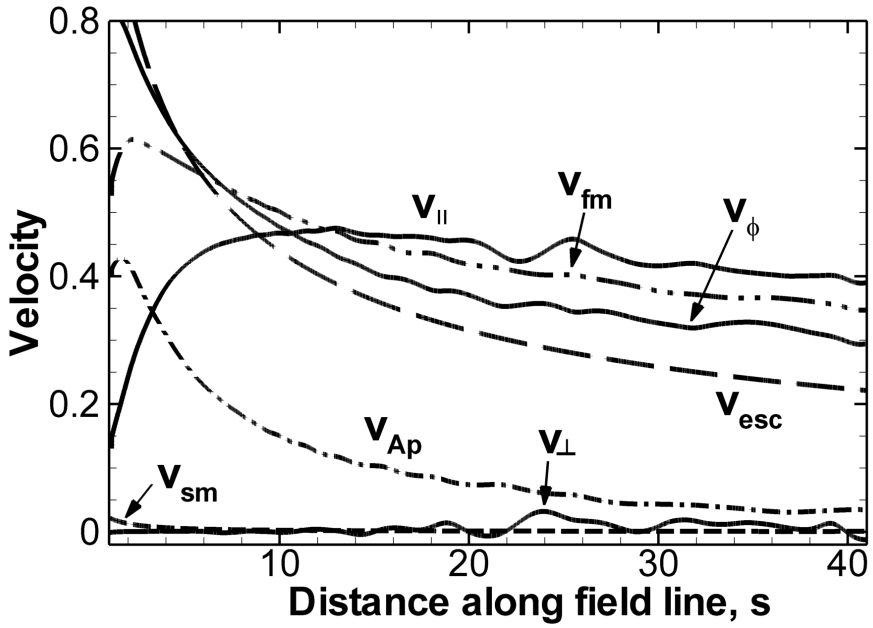

Figure 3.9: **Velocities as a function of distance along a representative field line.** The field line is anchored in the disc at $r = 1.24$ and extends through the jet to the outer boundary of the simulation region. A total of eight velocities are plotted. Starting from the left: $v_{\rm sm}$ is the slow magnetosonic velocity, v_{Ap} is the poloidal Alfvén velocity, $v_{\|}$ is the velocity of matter tangential to the field line, $v_{\perp}$ is the velocity of matter perpendicular to the field line, $v_{\rm fm}$ is the fast magnetosonic velocity, v_{ϕ} is the toroidal matter velocity along the field line, and lastly, $v_{\rm esc}$ is the local escape velocity.

field line with $s = 0$ at the base[3]. Figure 3.9 shows that very close to the star, $v_{\|}$—the matter velocity tangential to the field line—is small; however, $v_{\|}$ quickly rises above the slow magnetosonic $v_{\rm sm}$, Alfvén $v_{\rm Ap}$, and fast magnetosonic $v_{\rm fm}$ speeds as the matter moves away from the star, indicating that the flow is matter dominated past $s \approx 13$; most of the acceleration occurs before the matter crosses the fast magnetosonic surface. Fitting a power law to the region of strong acceleration gives $v_{\|} \propto s^{0.71}$; past $s \sim 5$, the acceleration mechanism weakens and the slope flattens such that $v_{\|} \propto s^{0.16}$. Near the disc, the toroidal component of the velocity, v_{ϕ}, is close to the Keplerian velocity meaning that the matter in the jet initially corotates with the disc. However, outside the

[3]Since the representative field line is nearly vertical, $s \approx r\cos\theta$

disc, v_ϕ falls off as $s^{-0.33}$ and $v_\parallel$ exceeds v_ϕ at $s \approx 12$ due to the continued acceleration of the matter.

Far away from the star, the tangential velocity is nearly double the escape velocity $v_{\rm esc}$ and the matter in the jet easily escapes from the system. In contrast, the perpendicular velocity $v_\perp$ in the jet is quite small, indicating that matter diffuses across the magnetic field very slowly.

3.5.3 Launching and collimation mechanisms

Forces in the jet

The force per unit mass tangent to the poloidal magnetic field line $\boldsymbol{B}_p$ can be calculated according to

$$\begin{aligned} f_{\rm tot,\parallel} &= \hat{\mathbf{b}} \cdot (\boldsymbol{f}_{\rm P} + \boldsymbol{f}_{\rm G} + \boldsymbol{f}_{\rm C} + \boldsymbol{f}_{\rm M}) \\ &= -\frac{1}{\rho}\frac{\partial P}{\partial s} - \frac{\partial \Phi}{\partial s} + \frac{v_\phi^2}{r\sin\theta}\sin\Theta + \frac{1}{4\pi\rho}\hat{\mathbf{b}} \cdot [(\nabla \times \boldsymbol{B}) \times \boldsymbol{B}]. \end{aligned} \tag{3.6}$$

Here, $\hat{\boldsymbol{b}}$ is the unit vector tangent to the field line, $\boldsymbol{f}_{\rm P}, \boldsymbol{f}_{\rm G}, \boldsymbol{f}_{\rm C}$, and $\boldsymbol{f}_{\rm M}$ are the pressure, gravitational, centrifugal and magnetic forces, respectively; Θ is the angle between the poloidal magnetic field line and the axisymmetry axis; Φ is the gravitational potential; s is the previously defined coordinate which traces the distance along the poloidal field line [see derivation in Ustyugova et al., 1999].

The pressure gradient force, $f_{\rm P,\parallel} = -(1/\rho)(\partial P/\partial s)$, dominates within the disc. The matter in the disc is approximately in Keplerian rotation such that the sum of the gravitational and centrifugal forces roughly cancel ($\boldsymbol{f}_{\rm G+C} \approx 0$). Near the slowly rotating star, however, the matter is strongly coupled to the stellar magnetic field and the disc orbits

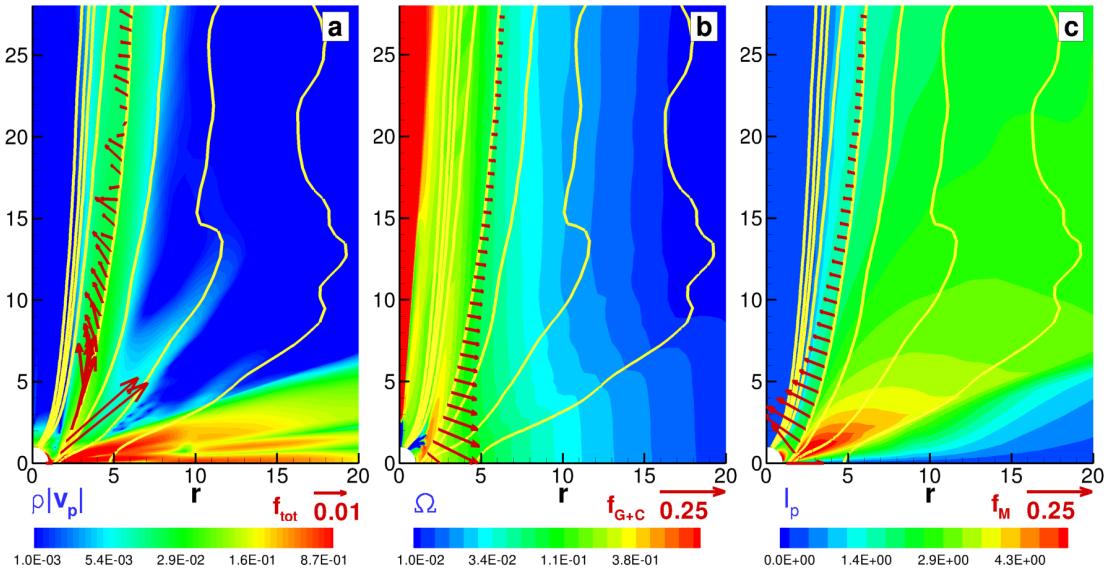

Figure 3.10: **Forces along a field line in the jet.** *Panel (a)* shows the poloidal matter flux density $\rho\left|\mathbf{v}_p\right|$ as a background overplotted with poloidal magnetic field lines. The vectors show the magnitude of the *total* force $\mathbf{f}_{\rm tot}$ along a representative field line originating from the disc at $r = 1.24$. *Panel (b)* plots the angular velocity Ω as the background. The vectors show the magnitude of the *gravitational + centrifugal* forces $\mathbf{f}_{\rm G+C}$ along the representative field line. *Panel (c)* shows the poloidal current I_p as the background. The vectors show the magnitude of the *magnetic* force $\boldsymbol{f}_{\rm M}$ along the representative field line.

at sub-Keplerian speeds, giving $\boldsymbol{f}_{\rm G+C} \lesssim 0$. The tangential magnetic force (the last term of Equation 3.6) can be expanded as

$$f_{\rm M,\parallel} = \frac{1}{4\pi\rho}\hat{\mathbf{b}}\cdot[(\nabla\times\boldsymbol{B})\times\boldsymbol{B}] = -\frac{1}{8\pi\rho(r\sin\theta)^2}\frac{\partial(r\sin\theta B_\phi)^2}{\partial s} \tag{3.7}$$

[Lovelace et al., 1991]. Note that $r\sin\theta B_\phi$ is the normalized poloidal current flowing through a surface of radius r from polar angle zero to θ.

The force per unit mass *perpendicular* to the poloidal field line is given by

$$f_{\mathrm{tot},\perp} = -(v_p^2 - v_{\mathrm{Ap}}^2)\frac{\partial\Theta}{\partial s} - \frac{1}{\rho}\frac{\partial}{\partial n}\left(P + \frac{\boldsymbol{B}_p^2}{8\pi}\right) - \frac{1}{8\pi\rho(r\sin\theta)^2}\frac{\partial(r\sin\theta B_\phi)^2}{\partial n} + \frac{v_\phi^2}{r\sin\theta}\cos\Theta - \frac{\partial\Phi}{\partial n}\,, \tag{3.8}$$

where n is a coordinate normal to the poloidal field line [Ustyugova et al., 1999]. In §3.5.2 we showed that far from the disc, the poloidal velocity in the jet v_{p} dominates over the poloidal Alfvén speed v_{Ap} (see Figure 3.9), permitting us to ignore the Alfvén term. Additionally, far outside the disc, the pressure gradient term is negligible and the gravitational force is small compared to the other forces. With these simplifications, Equation 3.8 reduces to

$$f_{\mathrm{tot},\perp} = -v_{\mathrm{p}}^2\frac{\partial\Theta}{\partial s} - \frac{1}{8\pi\rho}\frac{\partial\mathbf{B}_p^2}{\partial n} - \frac{1}{8\pi\rho(r\sin\theta)^2}\frac{\partial(r\sin\theta B_\phi)^2}{\partial n} + \frac{v_\phi^2}{r}\frac{\cos\Theta}{\sin\theta}. \tag{3.9}$$

Once the jet begins to collimate, the curvature term $-v_{\mathrm{p}}^2\partial\Theta/\partial s$ also becomes negligible. The magnetic force may act to either collimate or decollimate the jet, depending on the relative magnitudes of the toroidal $(r\sin\theta B_\phi)^2$ gradient (which collimates the outflow) and poloidal $\boldsymbol{B}_p^2$ gradient (which decollimates the outflow); in our simulations, the collimation of the matter implies that the magnetic hoop stress is larger than the poloidal field gradient. Thus the main perpendicular forces acting in the jet are the collimating effect of the toroidal magnetic field and the decollimating effect of the centrifugal force.

Figure 3.11 shows the dependence of Θ—the angle between the reference poloidal magnetic field line and the axisymmetry axis—on the distance along the field line s. For the poloidal field line in the reference case, we measure a half-opening angle $\Theta \approx 4^\circ$ for $s > 25$.

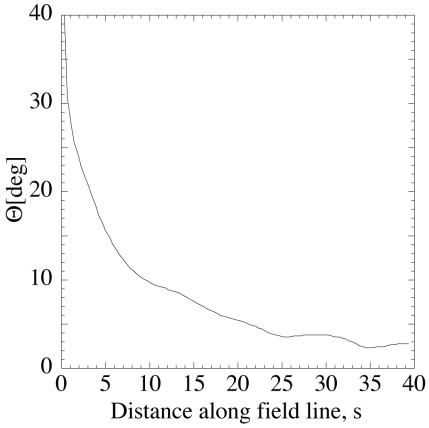

Figure 3.11: **Dependence of Θ on the distance along the field line.**

Analysis of the forces

Here, we analyze the role that the magnetic, gravitational, centrifugal, and pressure forces play in launching and collimating the outflow. Figure 3.10 shows vectors denoting the magnitude and direction of the various forces along a field line running through the jet: this field line is the same as the one used previously for analysis of the velocities in §3.5.2 and is anchored in the disc at $r = 1.24$. Figure 3.12 shows the tangential and perpendicular projections of the individual forces onto this field line.

Launching mechanism The top row of Figure 3.12 shows several different views of the tangential projections of the forces onto the representative field line. In order to accelerate the matter and launch an outflow, the sum of the tangential forces in the jet $f_{\mathrm{tot},\parallel}$ must be positive overall. The tangential projections of the gravitational and centrifugal forces are nearly equal and opposite everywhere in the jet (i.e. $f_{\mathrm{G+C},\parallel} \approx 0$) except near the star where gravity dominates and acts to hold the matter in the disc (e.g. Panel 3.12Ia). In contrast, the magnetic pressure force $f_{\mathrm{M},\parallel}$ acts in opposition to gravity and serves to accelerate the matter out of the disc along the magnetic field lines. Panel

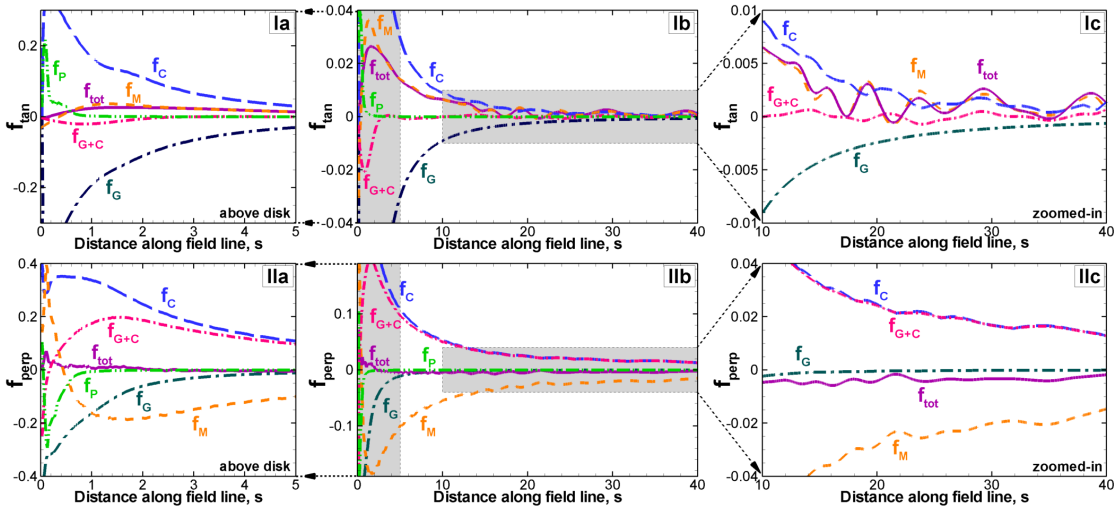

Figure 3.12: **Force components along a field line in the jet.** *Panels (Ia), (Ib) & (Ic)* show the *tangential* projection of the forces along the representative field line in: (Ia) the region just above the disc; (Ib) the whole simulation region; (Ic) the region far above the disc. A positive tangential force indicates acceleration away from the equatorial axis (i.e. the disc plane). *Panels (IIa), (IIb), & (IIc)* show similar plots of the *perpendicular* projection of the forces along the representative field line. A positive normal force indicates acceleration away from the axisymmetry axis.

Ib shows that the gas pressure force $f_{\mathrm{P},\|}$ is small outside the disc and plays no role in launching the outflow. Since $f_{\mathrm{G+C},\|}$ and $f_{\mathrm{P},\|}$ are both negligible far from the star, the magnetic force dominates within the jet giving $f_{\mathrm{tot},\|} \approx f_{\mathrm{M},\|}$.

The effect of the various forces can be seen in the three panels of Figure 3.10: $f_{\mathrm{G+C}}$ pulls the matter downward toward the disc (Figure 3.10b) while the the magnetic force f_{M} acts to drive matter out from the disc (Figure 3.10c). When these forces are summed together, the resulting force f_{tot} shown in Figs. 3.10a and 3.12Ib is positive overall; note that even far from the disc, $f_{\mathrm{tot},\|} > 0$ and the matter is continually accelerated. Since the centrifugal force is completely canceled by gravity, the jet is driven by a purely magnetic force and hence the launching mechanism is purely magnetic as well. This mechanism

is similar to the inner disc wind model discussed in Lovelace et al. [1991] and observed in simulations of conical winds in Romanova et al. [2009].

Collimation mechanism As discussed previously in §3.5.3, the collimation of the jet is related to the balance between the decollimating effect of the centrifugal force and the collimating effect of the magnetic hoop-stress; in order to collimate the jet, the sum of these perpendicular forces must be negative overall. The bottom row of Figure 3.12 shows the *normal* projection of the various forces onto the representative field line. Very close to the star, the perpendicular component of the centrifugal force is large and the net force is positive, pushing some of the matter into a "spur" (see Figure 3.10a). However past $s = 2.5$, the centrifugal force weakens as the matter moves away from the rotation axis, allowing the magnetic hoop-stress to collimate the matter into a jet. Figure 3.10 shows this very clearly: the centrifugal force in Figure 3.10b acts opposite to the magnetic force in Figure 3.10c. When the two forces are summed (Figure 3.10a), the forces largely cancel and the residual points inward toward the axis, serving to collimate the outflow into a jet. Note that the scale of the vectors in Figure 3.10a is much smaller than the scale in in Figs. 3.10b and 3.10c: the collimation is a delicate balance between the magnetic and centrifugal forces in the jet.

3.6 Discussion

3.6.1 Current flow in the simulation region

It is important understand the nature of the current flows in the simulation region. For general axisymmetric MHD flows the poloidal magnetic field ($[B_r, B_\theta]$ in spherical co-

ordinates) can be written as

$$\boldsymbol{B}_p = \nabla \times (A_\phi \hat{\boldsymbol{\phi}}) = \frac{\hat{\boldsymbol{r}}}{r^2 \sin\theta} \frac{\partial \Psi}{\partial \theta} - \frac{\hat{\boldsymbol{\theta}}}{r \sin\theta} \frac{\partial \Psi}{\partial r}, \tag{3.10}$$

where $\Psi(r, \theta) = r \sin\theta A_\phi(r, \theta)$ is the "flux function" for the poloidal magnetic field and A_ϕ is the vector potential [e.g., Lovelace et al., 1986]. The Ψ = const lines label the poloidal field in that $\boldsymbol{B}_p \cdot \nabla\Psi \equiv 0$.

For axisymmetric *and* non-relativistic MHD flows, Ampère's law gives the poloidal current density (in cgs units) as

$$\mathbf{J}_p = \frac{c}{4\pi} \nabla \times (B_\phi \hat{\phi}) = \frac{\hat{\mathbf{r}}}{r^2 \sin\theta} \frac{\partial H}{\partial \theta} - \frac{\hat{\boldsymbol{\theta}}}{r \sin\theta} \frac{\partial H}{\partial r}\ , \tag{3.11}$$

where $H(r, \theta) = cr \sin\theta B_\phi(r, \theta)/4\pi$ acts as the "flux function" for the poloidal current density in that $\mathbf{J}_p \cdot \nabla H \equiv 0$ [e.g., Lovelace et al., 1986].

In cgs units, the total poloidal current through a spherical cap, r = const and colatitude from 0 to θ, is simply

$$I_{p,\mathrm{cgs}} = 2\pi \int_0^\theta r^2 \sin\theta d\theta J_{pr} = 2\pi H(r, \theta) = \frac{c}{2} r \sin\theta B_\phi(r, \theta), \tag{3.12}$$

where $J_{pr} = \hat{\mathbf{r}} \cdot \mathbf{J}_p$. In all the plots we show the normalized current, $I_p = r \sin\theta B_\phi(r, \theta)$, which is proportional to $I_{p,\mathrm{cgs}}$. For the dipole-type field symmetry about the equatorial plane assumed in our simulations, $\Psi(r, \theta) = \Psi(r, \pi - \theta)$; that is, Ψ is an even function about the equatorial plane. This requires that the toroidal magnetic field be an odd function, $B_\phi(r, \theta) = -B_\phi(r, \pi - \theta)$ so that $B_\phi(r, \pi/2) = 0$ [Lovelace et al., 1987]. Thus we necessarily have

$$I_p(r, \pi/2) = 0. \tag{3.13}$$

Thus, our MHD simulations guarantee that the net current flow through the upper (or lower) hemisphere is exactly zero. A current outflow in a jet with, for example, $\theta < 1$ is exactly balanced by a current inflow in the region $\pi/2 - \theta < 1$. However, in the

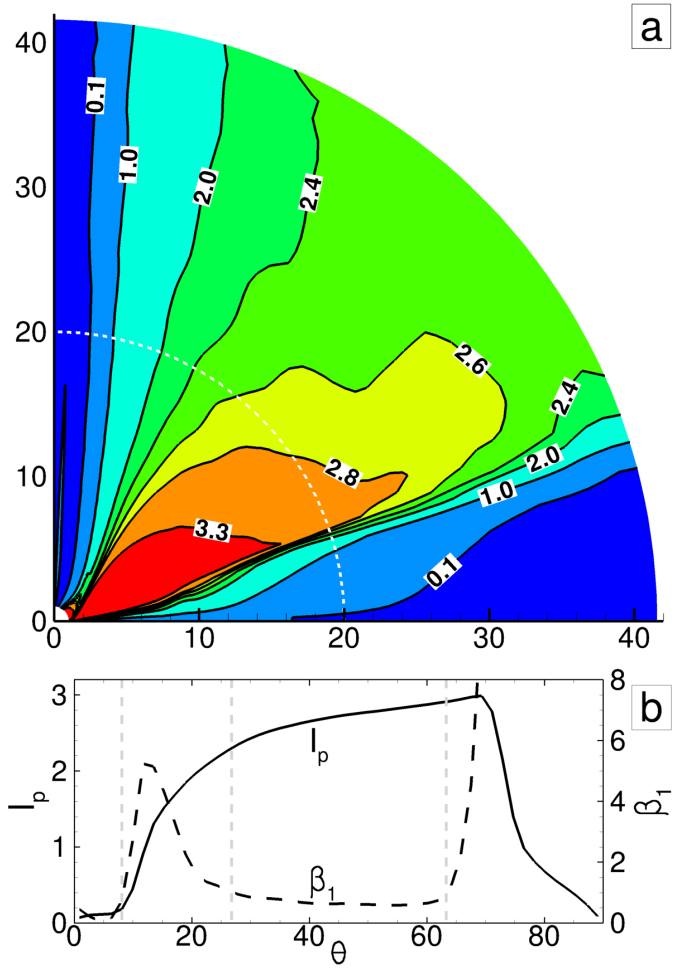

Figure 3.13: **Currents in the simulation region.** *Panel (a)*: The color background shows the values of $I_p(r,\theta)$ and the lines are current density lines. The numbers on the contours denote the local value of the current in normalized units. *Panel (b)*: The θ cross-section of the current and β_1 at $r = 20$, (see dashed line in the top panel). The dotted vertical lines represent the $\beta_1 = 1$ surfaces.

general case of *no* symmetry about the equatorial plane, we may have $I_p(r,\pi/2) \neq 0$ [see Lovelace et al., 2010].

The top panel of Figure 3.13 shows the poloidal current, $I_p(r,\theta)$, surfaces inside the simulation region. The values of I_p in normalized units are shown on the lines. Figure 3.13b shows that the largest current flow is between the jet and the disc with a value $I_p = 3$, corresponding to 2.1×10^{13} Ampères for a disc around a cTTs (see Table 3.1).

The current flow inside the jet is almost parallel to the jet, and is smaller than the current within the disc. The current carried by the jet flows out through the outer spherical boundary. At the same time, an equal amount of "return" current flows inward through the outer boundary and along the surface of the disc. The jet current and its return current have opposite signs and they repel as a result of their magnetic interaction mediated by the toroidal magnetic field B_ϕ. This repulsion between the jet and its return current has been clearly observed and discussed in previous MHD simulations by Ustyugova et al. [2000] and Nakamura et al. [2008]. The toroidal magnetic field is responsible for collimating the jet as discussed in §3.5.3. At the same time the toroidal field gives an outward radial force on the annular return current pushing it away from the jet axis.

3.6.2 Applications to young accreting stars

The dimensionless form of the simulations permit us to apply the results to a variety of stars of different sizes, from neutron stars to classical T Tauri stars. In Romanova et al. [2009], applications of the conical winds to different types of stars were discussed in detail and more recently, a model similar to the one presented in this paper has been applied to rapidly accreting FU Orionis-type stars [Königl et al., 2011]. In our simulations, the disc compresses the magnetosphere almost to the surface of the star, and the model is well suited for understanding young stars undergoing periods of enhanced accretion such as FUORs, EXors and magnetized cTTs's.

EXors The young star EX Lupi is the prototype of EXor-class stars in which the accretion rate may be enhanced up to $\dot{M} \sim 10^{-6} - 10^{-5} \mathrm{M}_\odot/\mathrm{yr}$ resulting in the ejection of powerful outflows [e.g. Herbig, 1989, Coffey et al., 2004, Brittain et al., 2007]. EXor outbursts are characterized by emission line spectra and last a few months to years, re-

curring on roughly equivalent timescales. The accretion rate obtained in our simulations is $\dot{M} = \widetilde{\dot{M}}\dot{M}_0$ (where $\widetilde{\dot{M}} \approx 160$ is the dimensionless accretion rate obtained in simulations, see Figure 3.8). The reference accretion rate $\dot{M}_0$ (and the dimensional accretion rate) strongly depend on the magnetic field of the star. For EXors, we assume $B_* = 800$ G and obtain $\dot{M} \sim 1.1 \times 10^{-5} \mathrm{M}_\odot/\mathrm{yr}$. Table 3.1 shows the other reference values for this case.

FUors The model is also well suited for describing FU Orionis-type (FUor-type) stars for which the accretion rate is very high, $\dot{M} \sim 10^{-5} - 2 \times 10^{-4} \mathrm{M}_\odot/\mathrm{yr}$, and the disc can strongly compress the magnetosphere. Unlike EXor events, FUor events are characterized by absorption in their spectra and can last many (≥ 10) years. The absorption in their spectra suggests a massive infall of matter onto the star, but the cause of this sudden infall is not understood. In Königl et al. [2011] the properties of the wind (density, velocities) were compared with those derived from the blue-shifted spectral features observed in the wind of FU Ori [Calvet et al., 1993, Hartmann and Calvet, 1995] and reasonable agreement was found. Table 3.1 shows an example of the reference values for FUors. Here, we increased the magnetic field of the star up to $B_* = 2.5 \times 10^3$ G in order for the magnetosphere to be able to stop the disc near the star. For this B_*, we obtain an accretion rate of $\dot{M} = \widetilde{\dot{M}}\dot{M}_0 = 2.5 \times 10^{-4} \mathrm{M}_\odot/\mathrm{yr}$ [4].

cTTs The model can be also applied to young stars—such as protostars and cTTs's—with much lower accretion rates. Compared to FUor-class stars, cTTs's show relatively small accretion rates of $\dot{M} \approx 10^{-7} - 10^{-8} \mathrm{M}_\odot/\mathrm{yr}$. Typical magnetic field strengths around T Tauri stars are on the order of one to a few kilogauss [see Yang and Johns-Krull, 2011]. However, the stellar field may be dominated by higher-order components of the

[4] Note that Königl et al. [2011] adopted a larger stellar radius and a smaller $\dot{M}$, finding $B_* = 2.1$ kG.

magnetic field while the dipole field (which dominates in the disc) may be comparatively weak [Donati et al., 2007, Gregory et al., 2008, Donati et al., 2011]. Taking this into consideration, we choose a weak equatorial dipole field of $B_* = 100$ G as a cTTs reference value and obtain a disc accretion rate of $\dot{M} = \widetilde{\dot{M}}\dot{M}_0 = 1.8 \times 10^{-7} \mathrm{M}_\odot/\mathrm{yr}$.

The ejection-to-accretion ratio obtained in our model, $\dot{M}_{\rm wind} \approx 0.2\dot{M}_{\rm accr}$ (see Figure 3.8), is somewhat larger than the typical values observed in cTTs's ($\lesssim$0.1) or FUors ($\sim$0.1) [Hartmann and Kenyon, 1996, Coffey et al., 2008]. In our simulations, the jets are successfully launched when the initial outflow is able to penetrate through the matter-dominated corona. The coronal density in our simulations is low (typically $\sim 10^{-4}$ of $\rho_{\rm d}$). Despite this, the corona is initially matter-dominated because the dipole magnetic field strength falls off rapidly with distance. The many simulations which produced collimated jets (see Table 3.2) show that the magnetic launching mechanism is robust and can drive jets from discs with a wide range of densities and accretion rates. However, only the most powerful outflows can penetrate through the matter-dominated corona. It is possible that we observe a selection effect in which only most powerful jets successfully penetrate through the dense corona, and in reality (when the coronal density is even lower), weaker jets can be launched. In that case, we expect the matter ejection-to-accretion ratio $\dot{M}_{\rm wind}/\dot{M}_{\rm accr}$ to be lower.

3.6.3 Collimation in different simulations

In Table 3.2, we show a sample of the simulations which produce collimated jets. The simulations exhibit a wide range of degrees of collimation with half-opening angles ranging between $\Theta = 4^\circ$ and $\Theta = 20^\circ$. The collimation observed in the jets is stronger

than in the conical winds studied in Romanova et al. [2009][5].

The key difference between the simulations presented in Romanova et al. [2009] and the new simulations presented here is the size of the simulation region: the new simulation region is nearly triple the size of the regions in the previous work. The larger simulation region in our model setup results in a higher accretion rate[6]. In addition, in the larger region, incoming disc matter collects and compresses a larger portion of the star's magnetic flux toward the star. Both factors lead to a higher magnetic pressure at the disc-magnetosphere boundary and to a correspondingly higher magnetic force. This results in the emergence of a more powerful, more magnetized outflow, leading to stronger collimation of the jet. We measure magnetization level with the kinetic plasma parameter β_1 which takes the ratio of the thermal plus ram pressure to the magnetic pressure (Equation 3.2). In all of the cases shown in Table 3.2, the jets are matter-dominated (i.e. $\beta_{1,\rm jet} > 1$). However, in strongly matter-dominated jets ($\beta_{1,\rm jet} \gtrsim 10$), weaker collimation is observed—for example, in the conical winds observed in Romanova et al. [2009], $\Theta \sim 30^\circ$ and $\beta_{1,\rm jet} = 10 - 30$. In contrast, when the outflow is only slightly matter-dominated (like in the reference case of this paper where $\beta_{1,\rm jet} \approx 1 - 6$, $\Theta \approx 4^\circ$) then collimation is strong.

3.6.4 Comparison with observation

Recent observations of several cTTs's with outflows have shown that ~10 AU away from the star, the outflows have already become collimated. However, in almost all of the cases the degree of collimation is low, with opening angles of ~20–30° at distances

[5]We should note that even in the case of the conical winds, the half-opening angle at the boundary reaches $20^\circ - 25^\circ$ at the end of the simulation run (see Figure 3.3, $t = 700$ panel) which is marginally close to the least collimated jets observed in current simulations.

[6]At the external boundary we fix the density of the incoming matter and hence $\dot{M}$ increases with the size of the simulation region.

10–50 AU [e.g. Hartigan et al., 2004]. These outflows eventually become very well collimated at larger distances, with opening angles of $2-5^{\circ}$ further away from the star [Dougados et al., 2000]. The jets in our simulations exhibit much faster collimation—$4-20^{\circ}$ at 0.4 AU and are likely most relevant to the highly accreting phase of young magnetized stars such as FUors or EXors where the outflow is expected to be launched locally from a highly compressed disc-magnetosphere boundary. However, observational coverage of jets around FUors and EXors is still sparse and there exist few constraints on the sub-AU structure of outflows from these highly accreting stars. However, comparisons of the our model with spectrally-derived properties of the wind in FU Ori star show that the simulations do agree with observed outflow velocities [Königl et al., 2011].

Alencar et al. [2005] performed a spectral analysis of the H_{α}, H_{β}, and NaD emission in the magnetosphere and at the base of the outflow in the highly accreting cTTs RW Aur A [$\dot{M} \sim 10^{-7.5}$ to 10^{-6} $M_{\odot}$/yr, Hartigan et al., 1995, White and Ghez, 2001]. Their results suggest that the high-velocity microjet in RW Aur A is likely launched as a "narrow wind" from a disc region between 2.2–5 R_{*}around the star, consistent with the launching region observed in our simulations. Their spectral fits also show that the field lines at the base of the outflow are inclined at $\Theta = 30-40^{\circ}$, consistent with the jet launching angle in our models (see Fig 3.11).

High velocity outflows launched from the inner disc (such as the collimated jets in our simulations) may explain the central component of jets with a layered "onion-skin" structure where the highest velocity, well collimated portion of the outflow flows close to the axis [Bacciotti et al., 2000]. If the disc is also threaded by an ordered magnetic field, then an extended disc wind may be responsible for the outer, less-collimated, low-velocity layers [Ouyed and Pudritz, 1997, Ferreira et al., 2006, Fendt and Elstner, 2000].

However, the simulations show a broad range of collimation and it is possible that the more weakly collimated jets are related to these outer layers as well.

3.7 Chapter summary

Through 2.5D MHD simulations, we have achieved robust, fully collimated jets emerging from the disc-magnetosphere boundary of an accreting magnetized star. We observe purely magnetic launching and collimation mechanisms: the cold matter at the disc-magnetosphere boundary is driven upward by the magnetic pressure and collimated by the helically wound magnetic field lines extending up from the disc. Approximately one-fifth of the incoming disc matter exits the system through the jet; the jet also advects some angular momentum out of the disc but the majority is transported outward through the disc by viscous stress. The degree of collimation in the jet is likely connected to the level of magnetization within the jet: our simulations show that strongly matter dominated jets with $\beta_1 \gtrsim 10$ are less collimated than the weakly matter dominated outflows where $\beta_1 \gtrsim 1$. In the reference simulation presented in this chapter, the matter in the jet is only slightly matter-dominated ($\beta_1 \gtrsim 1$) resulting in a magnetic field that strongly collimates the jet to a half-opening angle of $\Theta \approx 4^\circ$ at the top of the simulation region. Previous simulations by our group performed in a smaller simulation region showed the emergence of weakly collimated conical winds with a larger β_1 in the outflow (R09). The high levels of magnetization necessary to produce a strongly collimated jets may arise around stars such as EXors or FUORs where a high accretion rate strongly compresses the magnetosphere.

Observations suggest that the jets from protostellar systems become collimated at distances less than 10 AU away from the star (the present resolution limit) [Hartigan

et al., 2004, Coffey et al., 2008]. Our simulations show that the jet is launched and collimated on scales which are on the order of tens of stellar radii. However, the jets presented here may represent just the well collimated, high-velocity core of the "onion-skin" type outflows observed around young stars.

CHAPTER 4

PROPELLER-DRIVEN OUTFLOWS AND THE ACCUMULATION-ACCRETION CYCLE

4.1 Background and overview

In this chapter, we build upon the magnetically-driven MHD outflows investigated in Chapter 3 and study the emergence of centrifugally-driven outflows launched from the disc-magnetosphere boundary stars accreting in the propeller regime of accretion. The results shown in this chapter are presented in Lii et al. [2014].

The *propeller regime* is a regime of star-disc interaction in which the star and its magnetosphere rotate faster than the inner edge of the accretion disc $\Omega_* > \Omega_K(r_{\rm cor})$ [Illarionov and Sunyaev, 1975, Lovelace et al., 1999]. The propeller regime may arise in a number of accreting magnetized systems ranging from young newly-formed protostars to accreting millisecond pulsars to white dwarfs in cataclysmic variables [Stella et al., 1986, Cui, 1997, Alpar, 2001, Patruno et al., 2009, Wynn et al., 1997, Papitto et al., 2013]. In these systems, the accretion processes in the inner disc are dependent on the relative locations of the disc-magnetosphere boundary[1] $r_{\rm m}$ and the corotation radius $r_{\rm c} \equiv (GM_*/{\Omega_*}^2)^{1/3}$. If the stellar magnetosphere rotates slower than the inner disc, then $r_{\rm m} < r_{\rm c}$ and the disc matter accretes onto the star as a funnel flow [Lamb et al., 1973, Elsner and Lamb, 1977, Romanova et al., 2002]. In the opposite regime where $r_{\rm m} > r_{\rm c}$, the angular velocity of the magnetosphere is larger than the Keplerian angular velocity of the inner disc and the system is in the propeller regime of accretion. In this regime, the matter in the inner disc is inhibited from accreting onto the star and acquires angular

[1] Defined as the location where the magnetic stress in the magnetosphere is equal to the matter stress in the disc (see §4.4.1)

momentum from the stellar magnetosphere, leading to super-Keplerian rotation of the matter. This may in turn launch a propeller-driven outflow [Lovelace et al., 1999]. All types of accreting magnetized stars may enter this regime if the accretion rate in the disc decreases on a timescale shorter than the spin re-equilibration timescale.

The propeller regime has been studied analytically using magnetohydrodynamics [MHD, e.g. Davies et al., 1979, Li and Wickramasinghe, 1997, Lovelace et al., 1999, Ikhsanov, 2002, Rappaport et al., 2004, Ekşi et al., 2005] as well as numerically in MHD simulations [Wang and Robertson, 1985, Romanova et al., 2004, 2005, Ustyugova et al., 2006, Romanova et al., 2009, Zanni and Ferreira, 2013]. Numerical studies by Romanova et al. [2005, henceforth referred to as R05] and Ustyugova et al. [2006, U06] confirmed that propelling stars can launch strong magnetocentrifugal outflows as understood in Lovelace et al. [1999]. The simulated outflows are found to have two main components: (1) a conical-shaped, predominately centrifugally-driven magnetospheric wind (the "propeller wind") into which much of the disc matter flows and (2) a high-velocity, magnetically-driven and collimated axial jet (the "Poynting jet") into which a significant amount of energy and angular momentum flows. These previous simulations incorporated an α-prescription [Shakura and Sunyaev, 1973] to model the viscosity and magnetic diffusivity of the disc matter. Additionally, the simulations were performed on a spherical grid assuming top-bottom symmetry across the equatorial plane as well as axisymmetry about the rotation axis. In a similar set of simulations, Romanova et al. [2009] found that a conical-shaped outflow can be launched by magnetic pressure even in *slowly rotating* stellar systems [see also Königl et al., 2011, Lii et al., 2012]. Lovelace et al. [2010] performed full-region 2.5D simulations without top-bottom symmetry and found that a rapidly rotating star with an asymmetric stellar magnetic field can drive *one-sided* conical outflows. Further, they found that the outflows may be one-sided even when the stellar field is initially symmetric about the equatorial plane. More recently, a

study of the conical winds by Zanni and Ferreira [2013] showed that these conical-type outflows (which the authors term "magnetospheric ejections") are a ubiquitous feature of accreting magnetized stars. Together, these works demonstrate that the propeller regime may play a crucial role in the spin evolution and outflow launching in these systems.

The dynamics of the accretion disc play a critical role in star formation: the disc serves to remove angular momentum from the inner regions, thereby allowing for continual accretion onto the star. However, the exact mechanism for angular momentum transport is not clear: conventional molecular viscosity is too small to produce observed young star accretion rates. Rather, the magnetic fields likely play a critical role in the angular momentum transport. In regions of the disc where the ionization fraction is large enough, magnetic turbulence driven by the magneto-rotational instability (MRI) can serve as a viscosity generating mechanism [Balbus and Hawley, 1991]. The MRI mechanism operates as follows. A radial magnetic field line connects two adjacent annuli in a Keplerian disc; however, since the disc is Keplerian, the annuli orbit at different velocities and the field line is sheared by the differential rotation. The magnetic tension force opposes the shearing, resulting in a negative torque on the inner annulus and a positive torque on the outer annulus. This means that the matter in the inner annulus loses angular momentum (and hence accretes inward) while the outer annulus gains angular momentum and moves outward. As the annuli move apart from each other, the magnetic field line becomes further stretched and the effect is enhanced, resulting in an instability. For matter dominated discs with a weak seed field, the MRI can act as a dynamo process and amplify the weak seed field into a strong toroidal magnetic field. However, if the magnetic field becomes too large (i.e. $\beta \lesssim 10$), the MRI wavelength starts to exceed the disc height and the instability is suppressed.

In this chapter, we investigate the propeller regime and the dynamics of propeller

outflows, extending past work by utilizing our high spatial resolution code in axisymmetric cylindrical coordinates. The high resolution mesh provides a detailed view of the star-disc interaction and resolves the MHD turbulence generated by MRI. The MRI-driven turbulence facilitates disc accretion and for this reason neither the α-viscosity nor α-diffusivity coefficients are included in the numerical algorithm. Earlier, this code was used to study MRI-driven accretion onto slowly rotating stars [Romanova et al., 2011]. Here we study propeller-driven outflows in the *strong propeller* regime in which $r_{\rm mag} \gtrsim 2^{1/3} r_{\rm cor}$. Below this threshold, the linear velocity of the magnetosphere is lower than the local escape velocity and the centrifugal force is insufficient to accelerate the gas out of the system. Instead, the system enters the *trapped disc* regime in which the disc matter is blocked from accreting and continuously recycled instead of being ejected from the disc [e.g. D'Angelo and Spruit, 2012].

The simulations presented in this chapter show that stars accreting in the strong propeller regime will undergo non-steady, episodic accretion. This accretion cycle can be accompanied by centrifugally-driven outflows launched from the disc-magnetosphere boundary. In §4.2, we discuss the numerical model. In §4.4, we investigate the propeller-driven outflows found in our models: in §4.4.2 we investigate the centrifugally-dominated launching mechanism and the propeller wind, in §4.4.3 we study the magnetically-dominated Poynting outflow, and in §4.4.4 we analyze the angular momentum transport and measure the spin-down rates for each of the stars. Lastly, in §4.6, we discuss the effect of the MRI, the structure of the outflows and compare our results to previous studies.

4.2 The numerical model

In order to study the propeller regime, we utilize the mesh based Godunov MHD code in 2.5D axisymmetric cylindrical coordinates described previously in §2.6.1. For this study, no viscosity or diffusivity terms are included in the MHD equations and hence we investigate only accretion driven by the resolved MRI-turbulence. This code has been previously utilized to study MRI-turbulent accretion onto a magnetized star [see tests and other details in Romanova et al., 2011, Koldoba et al., August 2015].

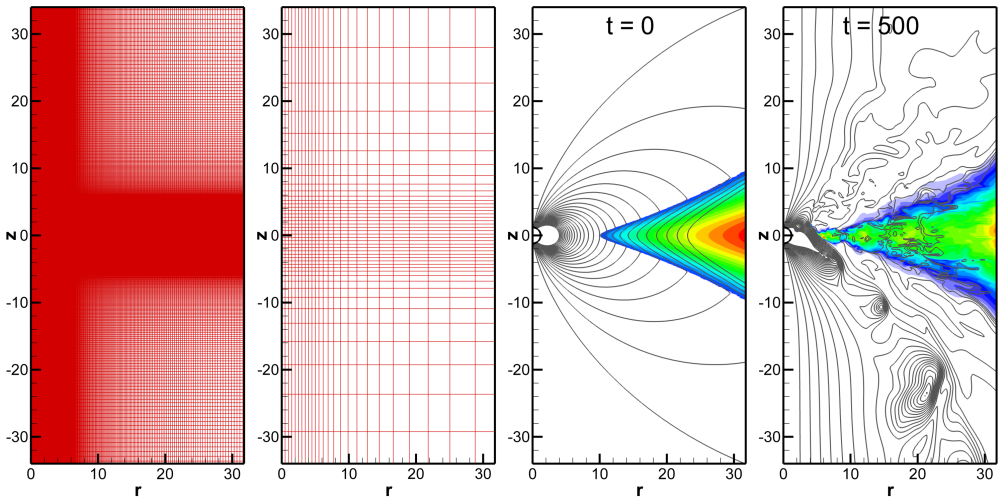

Figure 4.1: **The 2.5 axisymmetric cylindrical grid.** From left to right: (1) grid used in simulations, (2) same grid but with 1/10th of the grid lines shown for clarity; (3) initial distribution of density (background) and magnetic flux (lines); (4) same but for time $t = 500$.

Grid description: The axisymmetric grid is in cylindrical (r, z) coordinates with mesh compression towards the disc and towards the z-axis such that there are a larger number of cells in the disc plane and near the star (see Figure 4.1, left panel). In the models presented here, we use a non-uniform grid with dimension 250×432 cells corresponding to a grid that is 66 by 140 stellar radii in size (0.61 AU by 1.3 AU if $R_* = 2R_\odot$). At $r = 20$, the number of grid cells which cover the disc in the vertical direction is about

Table 4.1: **Reference units for three different types of accreting stars.** Typical values of the stellar mass M_*, radius R_*, magnetic field B_*, and dimensionless magnetic moment ($\tilde{\mu} = 10$) for each star are chosen and the other reference values are derived from these parameters.

	cTTs	White Dwarf	Neutron Star
initial			
M_* [$M_\odot$]	0.8	1	1.4
R_*	$2R_\odot$	5000 km	10 km
B_* [G]	3000	5×10^5	5×10^8
derived			
R_0 [cm]	2.78×10^{11}	10^9	2×10^6
B_0 [G]	35	6.25×10^3	6.25×10^6
v_0 [cm s^{-1}]	1.95×10^7	3.64×10^8	9.64×10^9
t_0	1.04 d	17.28 s	1.30 ms
Ω_0 [s^{-1}]	7.02×10^{-5}	0.364	4.82×10^3
f_0 [dy g^{-1}]	1.37×10^3	1.33×10^8	4.64×10^{13}
p_0 [dy cm^{-2}]	1.22×10^3	3.91×10^7	3.91×10^{13}
ρ_0 [g cm^{-3}]	3.21×10^{-12}	2.94×10^{-10}	4.20×10^{-7}
T_0 [K]	4.63×10^6	1.61×10^8	1.13×10^{12}
μ_0 [G cm^3]	7.54×10^{35}	6.25×10^{30}	5×10^{25}
$\dot{M}_0$ [$M_\odot$ yr^{-1}]	7.70×10^{-8}	1.70×10^{-9}	2.57×10^{-10}
$\dot{L}_0$ [g cm^2 s^{-2}]	2.64×10^{37}	3.91×10^{34}	3.12×10^{32}

200.

Reference units: The simulations are performed in dimensionless units and are applicable to stars over a wide range of scales. There are four free parameters: we choose the values of the stellar mass M_*, radius R_*, magnetic field B_* and dimensionless magnetic moment $\tilde{\mu}$ and derive reference values from these parameters. The magnetic moment $\boldsymbol{\mu} = \tilde{\mu}\mu_0\hat{z}$ is used to initialize the stellar dipole field (see Equation 2.57). In this chapter, we take $\tilde{\mu} = 10$ in all of the models. The reference units are as follows: length $R_0 = 2R_*$, magnetic moment $\mu_0 = B_0 R_0^3$, magnetic field $B_0 = B_*/\tilde{\mu} \times (R_*/R_0)^3$ (the equatorial field dipole strength at $r = R_0$) , velocity $v_0 = \sqrt{GM_*/R_0}$ (the Keplerian orbital velocity at $r = R_0$), time $t_0 = 2\pi R_0/v_0$ (the Keplerian orbital period at $r = R_0$), angular velocity

Table 4.2: **Model parameters.** In dimensionless units, r_c is the corotation radius, Ω_* is the angular velocity of the star, and P_* is the period of stellar rotation.

r_c	Ω_*	P_*
1.3	0.674	1.48
1.5	0.544	1.84
2.0	0.353	2.83

$\Omega_0 = v_0/R_0$, pressure $p_0 = B_0^2$, density $\rho_0 = p_0/v_0^2$, temperature $T_0 = p_0/\rho_0 \times m_H/k_B$ where m_H is the mass of hydrogen and k_B is the Boltzmann constant, force per unit mass $f_0 = v_0^2/R_0$, accretion rate $\dot{M}_0 = \rho_0 v_0 R_0^2$ and angular momentum flux $\dot{L}_0 = \dot{M}_0 v_0 R_0$. Table 4.1 shows sample reference values for three different types of accreting stars: to apply the simulation results to a particular class of star, multiply the dimensionless value by the reference value.

For the remainder of this chapter, all values and variables are given in terms of the dimensionless units, except where they have explicitly assigned physical units. In all following plots, time and distance are always given in units of t_0 and R_0.

The models are set up as a rapidly rotating star with a dipole magnetic field (shown in the third panel of Figure 4.1). This field threads an accretion disc with matter density and pressure distributions in hydrostatic equilibrium. In addition to the dipole magnetic field, there is a "tapered" magnetic component which threads the disc and assists the development of the MRI. A detailed description of the initial and boundary conditions can be found in §4.3.

4.3 Initial and boundary conditions

Initial conditions: In this work, the initial conditions for the hydrodynamic variables are similar to those taken in our previous works [e.g. Romanova et al., 2002, 2011] where the initial density and entropy distributions have been calculated from the force-balance of different forces which include gravity, centrifugal and pressure forces. The disc is initially cold and dense with temperature T_d and density ρ_d. The corona is hot and rarified with temperature $T_c = 10^3 T_d$ and density $\rho_c = 10^{-3}\rho_d$. At the start of the simulations, the inner edge of the disc is placed at $r_d = 10$ and the star rotates with $\Omega_i = 0.032$ (corresponding to $r_c = 10$) such that the magnetosphere and inner disc initially corotate. This condition helps to ensure that the magnetosphere and disc are initially in near-equilibrium at the disc-magnetosphere boundary. From 0 to $100t_0$, the star is gradually spun up from Ω_i to the final state with angular velocity Ω_* (given in Table 4.2). The initial pressure distribution in the simulation is determined from the Bernoulli equation

$$F(p) + \Phi + \Phi_c = b_0 = \text{constant}, \tag{4.1}$$

In this equation, $\Phi = -GM_*/(r^2 + z^2)^{1/2}$ is the gravitational potential, $\Phi_c = -kGM/r$ is the centrifugal potential where k is a Keplerian parameter[2], b_0 is the Bernoulli constant and

$$F(p) = \begin{cases} \mathcal{R}T_d \ln(p/p_b), & \text{if } p > p_b \text{ and } r > r_d, \\ \mathcal{R}T_c \ln(p/p_b), & \text{if } p \le p_b \text{ or } r \le r_d, \end{cases} \tag{4.2}$$

where p_b is the pressure at the boundary which separates the disc from the corona. We assume the system is intially barotropic and determine the density from the pressure

$$\rho(p) = \begin{cases} p/\mathcal{R}T_d, & \text{if } p > p_b \text{ and } r > r_d, \\ p/\mathcal{R}T_c, & \text{if } p \le p_b \text{ or } r \le r_d. \end{cases} \tag{4.3}$$

[2]We take k slightly greater than unity to balance the disc pressure gradient (k=1+0.02).

To initialize the MRI, 5% velocity perturbations are added to v_ϕ inside the disc.

Initial magnetic field configuration: Initially, the disc is threaded with the dipole magnetic field of the star. We also add a small "tapered" poloidal field inside the disc (see third panel in Figure 4.1) which is given by

$$\Psi = \frac{B_0 r^2}{2} \cos\left(\pi \frac{z}{2h}\right), \;\; h = \sqrt{\left(\frac{GM_*}{\Phi_c(r) - E}\right)^2 - r^2},$$

where h is half-thickness of the disc and E is a constant of integration in the initial equilibrium equation [see Romanova et al., 2002, 2011]. This tapered field helps to initialize the MRI in the in the disc and has the same polarity as the stellar field at the disc-magnetosphere boundary.

Boundary Conditions: *Stellar surface:* all variables on the surface of the star have "free" boundary conditions such that $\partial(...)/\partial n = 0$ along the entire surface, where n is the normal vector to the stellar surface. We prohibit the outflow of matter from the star (i.e. we do not allow for stellar winds) and adjust the matter velocity vectors to be parallel to the magnetic field vectors. This models the frozen-in condition on the star. *Top and bottom boundaries:* all variables have free boundary conditions along the top and bottom boundaries. In addition, we implement outflow boundary conditions on the velocity to prohibit matter from flowing back into the simulation region once it leaves. *Outer side boundary:* the side boundary is divided into a "disc region" ($|z| < z_{\rm disc}$) and a "coronal region" ($|z| > z_{\rm disc}$), with

$$z_{\rm disc} = h(R_{\rm out}) = \sqrt{\left(\frac{GM_*}{\Phi_c(R_{\rm out}) - E}\right)^2 - R_{\rm out}^2},$$

where $R_{\rm out}$ is the external simulation radius. The matter along the disc boundary ($|z| < z_{\rm disc}$) is allowed to flow in with a small radial velocity

$$v_r = -\delta \frac{3}{2} \frac{p}{\rho v_K(R_{\rm out})}, \;\; \delta = 0.02,$$

and with a poloidal magnetic field corresponding to the calculated magnetic field at $r = R_{\rm out}$. The remainder of the variables are allowed to have free boundary conditions. The coronal boundary ($|z| > z_{\rm disc}$) has the same boundary conditions as the top and bottom boundaries.

4.4 Results: accretion and outflows in the propeller regime

The primary aim of this chapter is to analyze propeller-driven outflows. For this reason, we focus on three main cases of stars in the strong propeller regime of accretion where $r_{\rm m}$ is a few times $r_{\rm c}$: we take $r_{\rm c} = 1.3$, 1.5, and 2 (see Table 4.2 for the other parameters). For typical cTTs, these corotation radii would correspond to rapid rotators with rotational periods of 1.5, 1.9, and 2.9 days, respectively. In this regime, the rapid rotation of the star and its associated magnetosphere creates a centrifugal barrier at the disc-magnetosphere boundary which inhibits accretion and drives strong outflows. In contrast, in the regime where $r_{\rm m} \lesssim 2^{1/3} r_{\rm c}$, the centrifugal barrier inhibits the accretion but is insufficient to accelerate matter past the local escape velocity, resulting in a trapped disc which is neither accreted nor ejected [D'Angelo and Spruit, 2012]. Here, we focus on the regime of faster rotation which produces more continuous outflows.

4.4.1 Episodic accretion and magnetospheric oscillations

The inner disc dynamics are largely determined by the interaction between the disc and the stellar field lines at the disc-magnetosphere boundary. In the propeller regime in particular, the centrifugal barrier inhibits continuous accretion onto the rapidly rotating star; instead, accretion proceeds through an episodic accumulation-accretion cycle in

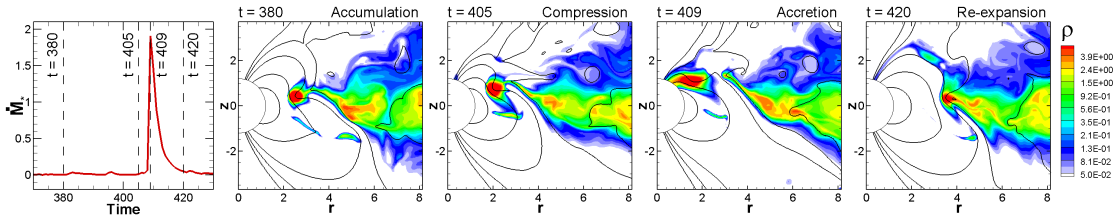

Figure 4.2: **Episodic accretion.** *Leftmost panel:* Accretion rate onto the star $\dot{M}_*$ during one cycle of the accretion-accumulation process in the r_c=2 model. *Right panels:* Four corresponding time slices illustrating one cycle in the same model.

which episodes of matter accumulation are followed by a brief burst of simultaneous matter ejection and accretion. As shown in Figure 4.2, this mechanism proceeds in three main phases:

1. **Accumulation (t = 380):** The matter accreting through the disc is blocked from accreting onto the star by the centrifugal barrier. Instead, it accumulates at the disc-magnetosphere boundary. As the matter piles up, the ram pressure increases and gradually compresses the stellar magnetosphere inward towards the star. At the same time, the accumulated matter gradually diffuses into the magnetosphere.

2. **Compression and accretion (t = 405–409):** The matter continues to compress the magnetosphere toward the star until the gravitational acceleration exceeds the opposing centrifugal acceleration. At this point, the matter accretes onto the star as a funnel flow.

3. **Re-expansion (t = 420):** With the accumulated reservoir of matter depleted, the magnetosphere is no longer compressed and quickly expands outward, shutting off the accretion and restarting the cycle anew.

This episodic accretion results in a "spiky" accretion rate, evident in the left panel of Figure 4.2 and in Figure 4.4, in which any accretion onto the star occurs in quasi-periodic

bursts with frequencies of up to a hundred dynamical timescales. The matter in the disc accumulates at the disc-magnetosphere boundary due to the strong centrifugal barrier as well as the very low diffusivity in this region. If the diffusivity were higher, the accretion may become smoother and a higher fraction of the accreting matter may be ejected (see analysis in §4.5).

The Magnetospheric Radius The process of accumulation and accretion results in oscillations of the magnetospheric and inner disc radii. The star's magnetospheric radius $r_{\rm m}$ may be estimated using a few different methods as illustrated in the top panel of Figure 4.3. One intuitive method is to estimate $r_{{\rm m}\beta_1}$ as the location where the magnetic and matter pressures are equal, corresponding to the region where the kinetic plasma parameter $\beta_1 = 8\pi(P + \rho v^2)/B^2 = 1$ [Romanova et al., 2002]. Alternatively, $r_{{\rm m}\beta}$ may be defined as the region where the plasma parameter $\beta = 8\pi P/B^2 = 1$ [Bessolaz et al., 2008]. The latter definition tracks the region where matter flows from the disc to the funnel flow and is most applicable to the case where the magnetosphere and inner disc rotate with nearly the same angular velocity [see also Kulkarni and Romanova, 2013].

These empirically measured radii can also be compared to theoretically-derived estimates of the magnetospheric radius $r_{{\rm m}A} = kr_A$ where $r_A = (\mu^4/2GM_*\dot{M}^2)^{1/7}$ is the Alfvén radius for spherical accretion [Ghosh and Lamb, 1978], $\dot{M}$ is the disc accretion rate, and k is a coefficient of order unity. This coefficient has been estimated from comparisons of numerical simulations and theoretical formulae [e.g., Long et al., 2005, Zanni and Ferreira, 2013]. The bottom panel of Figure 4.3 shows the empirical and theoretical measures of $r_{\rm m}$ as a function of time alongside the stellar accretion rate, $\dot{M}_*$, for the case of the model with $r_{\rm c}$= 2. To estimate the theoretical $r_{\rm m}$ we take $k = 0.7$ to best match the empirically derived radii. Additionally, the disc accretion rate is estimated by height averaging and smoothing $\dot{M}$ through the disc at $r = 7$. The theoretical esti-

mate approximately coincides with the measured values; however, it does not exhibit the strong oscillations exhibited by the empirical measurements as $\dot{M}$ is measured further out in the disc.

The cyclic accumulation-accretion process causes the magnetosphere to oscillate strongly with the sharpest transitions corresponding to each burst of accretion onto the star. As shown in the top panel of Figure 4.3, the magnetospheric radius obtained from the $\beta_1 = 1$ criterion, $r_{\mathrm{m}\beta_1}$, best describes the true position of r_{m} in the propeller regime (although it does not substantially differ from $r_{\mathrm{m}\beta}$). This is likely because the matter ram pressure ρv^2 provides an additional, non-negligible contribution to the total matter pressure in this regime. Nonetheless, in all of the models, both measured radii are larger than the corotation radii, indicating that the simulations are all well within the propeller regime of accretion.

The accumulation-accretion observed here is fundamentally similar to the episodic accretion cycle identified by Sunyaev and Shakura [1977], developed by Spruit and Taam [1993] and studied in-depth by D'Angelo and Spruit [2010]. These previous works solely consider accretion in the equatorial plane, whereas in our axisymmetric simulations, the disc matter may accrete around the magnetosphere. Additionally, these works do not consider the strong propeller regime. Nonetheless, the physical mechanism underlying the accumulation-accretion cycle is quite similar.

4.4.2 The matter dominated wind

Each burst of accretion onto the star is associated with a corresponding burst of matter ejection: this is most evident in the $r_{\mathrm{c}} = 2$ model (rightmost panel of Figure 4.4) which shows a strong correlation between $\dot{M}_*$ and $\dot{M}_{wind}$ and exhibits very little outflow at

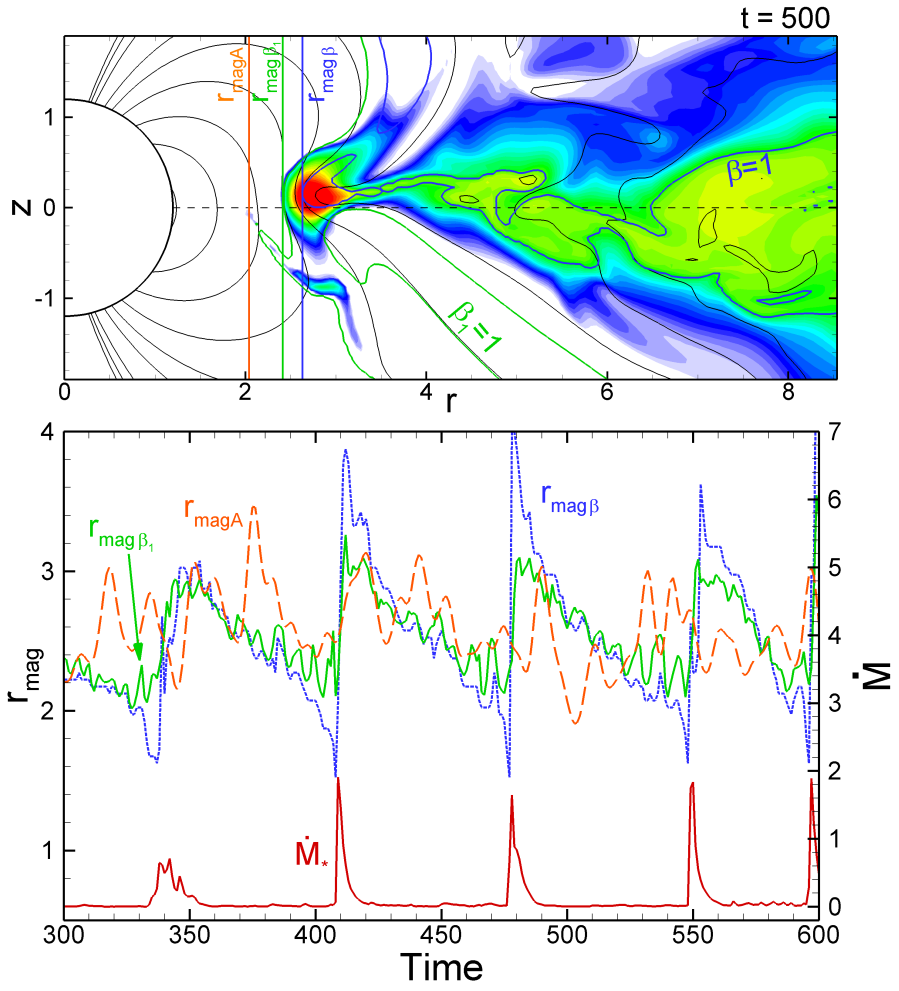

Figure 4.3: **The magnetospheric radius.** *Top panel:* A snapshot from the r_c= 2 model showing the location of the magnetospheric radius as measured using the Alfén radius r_A (r_{mA}), the kinetic plasma parameter β_1 ($r_{m\beta_1}$), and the plasma parameter β ($r_{m\beta}$). *Bottom panel:* The same three measures of the magnetospheric radius and the accretion rate onto the star, $\dot{M}_*$, as a function of time in the r_c=2 model (see text for description).

other times. In the faster rotating models (r_c = 1.3, 1.5), we also observe a second, more continuous outflow which is launched during the *accumulation phase* when there is no accretion onto the star. Together, these comprise the two primary modes of outflow driven by the rapidly rotating star: the first is a quasi-steady outflow launched in the accumulation phase and the second is a transient burst of matter associated with the accretion phase. In §4.4.2 and 4.4.2 we investigate these outflows in the non-accreting

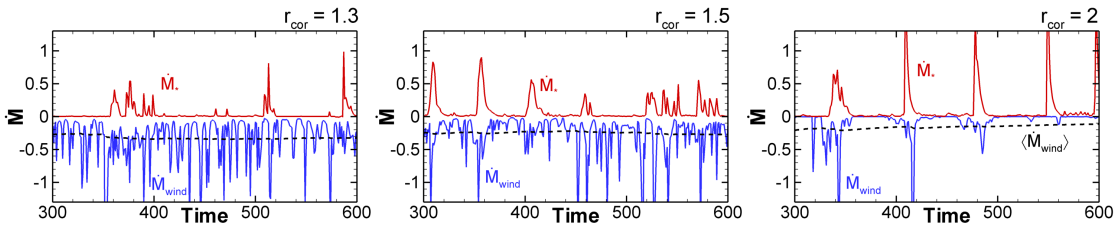

Figure 4.4: **Matter fluxes in the three models.** The red lines show the accretion rate onto the star, $\dot{M}_*$, and the dark blue lines show the outflow rates $\dot{M}_{\rm wind}$. For reference, the time averaged outflow rates $\langle \dot{M}_{\rm wind} \rangle$ are also plotted as black dashes.

and accreting phases separately.

The matter flux into the wind, $\dot{M}_{\rm wind}$, is measured by integrating the flux through a cylindrical surface with radius $r = 20$ and height $z = 40$ centered on the star. For the outflow we only consider the fast component of the flow where $v_p \geq 0.2$. To investigate the long-term accretion and outflow rates, we calculate the time averaged accretion rate

$$\langle \dot{M}(t) \rangle = \frac{\int_{t_i}^{t} dt' \dot{M}(t')}{\int_{t_i}^{t} dt'} \,. \tag{4.4}$$

The time averaged $\langle \dot{M}_{\rm wind} \rangle$ is shown as a dashed line in Figure 4.4: evidently, the rotation rate is inversely correlated to the outflow rate. We find ejection efficiencies $\langle \dot{M}_{\rm wind} \rangle / (\langle \dot{M}_{\rm wind} \rangle + \langle \dot{M}_* \rangle)$ of 0.87, 0.74, and 0.51 for the $r_{\rm c} = 1.3$, 1.5, 2 models, respectively. The faster rotators are highly efficient and eject most of the accreting matter into an outflow before it can reach the star. In contrast, the weaker $r_{\rm c} = 2$ propeller only launches an outflow during the brief accretion phase and $\langle \dot{M}_* \rangle \approx \langle \dot{M}_{\rm wind} \rangle$ for this case. In the following sections, we study the outflow launching mechanism and investigate the dependence of $\dot{M}_{\rm wind}$ on Ω_*.

Outflow in the accumulation phase

The first outflow mode is a continuous, quasi-steady wind launched in the *accumulation phase* of the episodic accretion cycle. Figure 4.5 shows three time snapshots of this wind in the r_c=1.3 model, which is the fastest rotator we consider in this chapter. The outflow undergoes a cyclic accretion-ejection mechanism similar to the mechanism described by Goodson and Winglee [1999]. During the accumulation phase of the episodic accretion cycle, a fraction of the accumulated matter diffuses into the outer magnetosphere. There, the matter picks up angular momentum from the faster-rotating stellar field lines as it is brought into corotation with the star. As the matter approaches corotation, it becomes super-Keplerian and begins to flow out along the inclined field lines of the compressed dipole (t = 310). It flows away, inflates the magnetosphere (e.g. t = 312) and is accelerated out along the magnetic field lines by the centrifugal force. Once the matter is ejected, the field lines reconnect and truncate the outflow (t = 314) until more matter can penetrate and again inflate the magnetosphere. This cyclic inflation-reconnection results in the ejection of discrete plasmoids, similar to the clumpy winds observed in previous studies of propeller outflows [e.g R05, U06, and Zanni and Ferreira, 2013]. The $\dot{M}_{\rm wind}$ in Figure 4.4 shows that the strength of the accumulation-phase outflow is largely dependent on the spin period of the star, with faster rotators ejecting much more matter out of the disc. The accretion-ejection mechanism observed in our models differs from that described by Goodson and Winglee [1999] in that the field lines in the outflow are inflated by the ejection of the matter instead of the differential rotation between the star and disc. In our models, the stellar field lines are largely decoupled from the disc due to the weak diffusivity.

As in previous studies of propeller outflows, a half-opening angle of roughly 45° is observed at the base of the propeller wind with evidence of gradual collimation at larger

distances in the strongest outbursts. The bottom panels of Figure 4.5 show snapshots of the angular velocity Ω alongside the poloidal velocity vectors $\mathbf{v}_p$ and stellar magnetic field lines. The large contrast in the angular velocities of the magnetosphere and inner disc is evident in the figure. Additionally, the reservoir of matter which builds up at the disc-magnetosphere boundary can be seen in the geometry of the magnetic field lines.

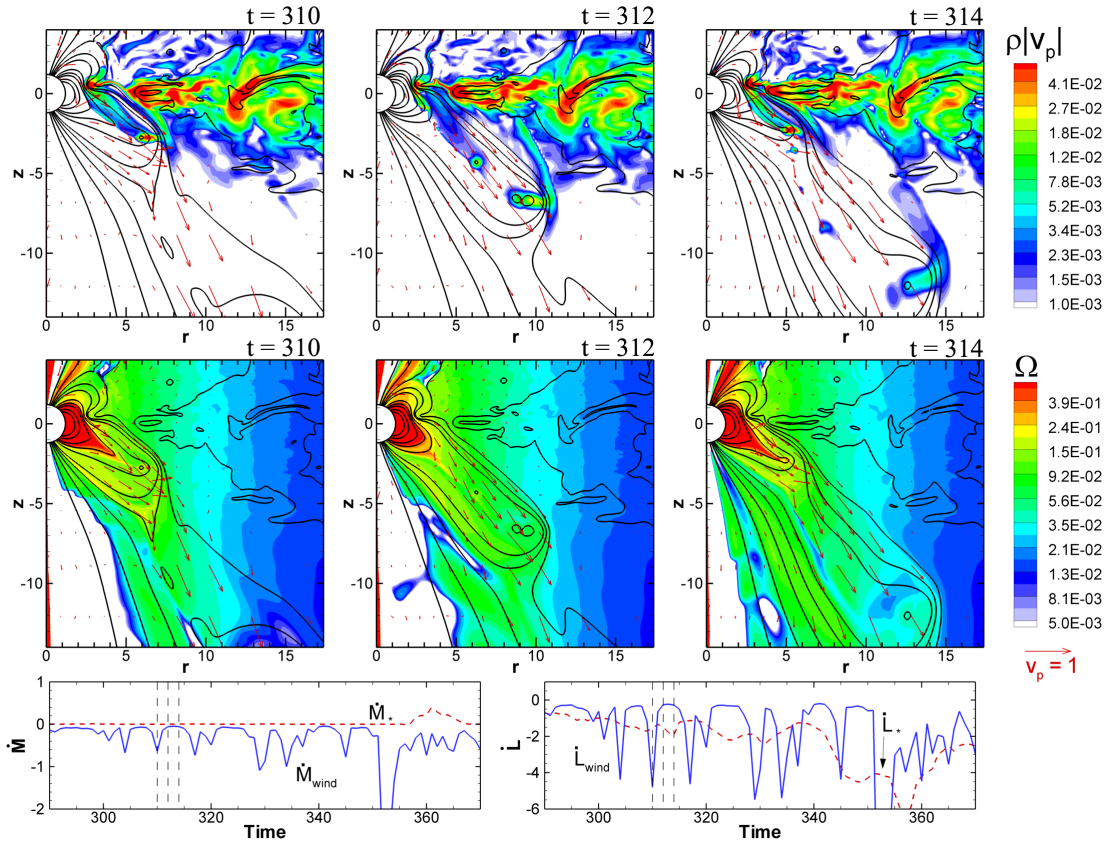

Figure 4.5: **The non-accreting outflow mode.** *Top panels:* three snapshots of the r_c=1.3 simulation region showing the plasmoids launched during the non-accreting phase of the episodic accretion cycle. The matter flux density ρv_p is plotted with field lines and velocity vectors superimposed. *Middle panels:* the angular velocity Ω of the matter at those same three moments in time. *Bottom panels:* matter and angular momentum fluxes onto the star and into the wind. The vertical dotted lines denote times corresponding to the three snapshots shown.

Outflow in the accreting phase

In addition to the quasi-steady outflows in the non-accreting stage, the simulations also show a transient burst associated with the brief episode of accretion at the end of the episodic accretion cycle. Figure 4.6 shows this outflow as a series of four snapshots from the same r_c= 1.3 model as above. In contrast to the continuous, quasi-steady outflow present in the accumulation phase, this stronger outflow occurs as a one-off burst which is launched in tandem with the accretion of the accumulated matter onto the star.

The leftmost panels of Figure 4.6 show the state of the simulation as it approaches the end of the episodic accretion cycle (t = 351). The matter reservoir at the disc-magnetosphere interface has compressed the magnetosphere far enough inward that the gravitational acceleration exceeds the centrifugal acceleration, allowing accretion to proceed onto the star. As the matter falls onto the star, it deflects the magnetosphere to one side and forms a transient funnel flow (t = 356). At the same time, some of the accreting matter diffuses into the magnetosphere and quickly picks up angular momentum from the field lines. As it is accelerated away, the matter inflates the magnetosphere allowing much of the remaining matter to flow away as well. Once the reservoir of matter compressing the magnetosphere is depleted by the ejection and accretion, the magnetosphere re-expands, halting the funnel flow of matter and reverting the outflow back to the initial non-accreting state. This episodic accretion event creates a transient rise in the outflow rate occurring on a few dynamical timescales of the very inner disc (shown in bottom panels of Figure 4.6). Since this outflow tends to be stronger, it also tends to be more collimated than the weaker outflow in the accumulation phase: at the base of the outflow, we measure half-opening angles ranging from 20–40° (compared to $\sim 45°$ in the non-accreting phase).

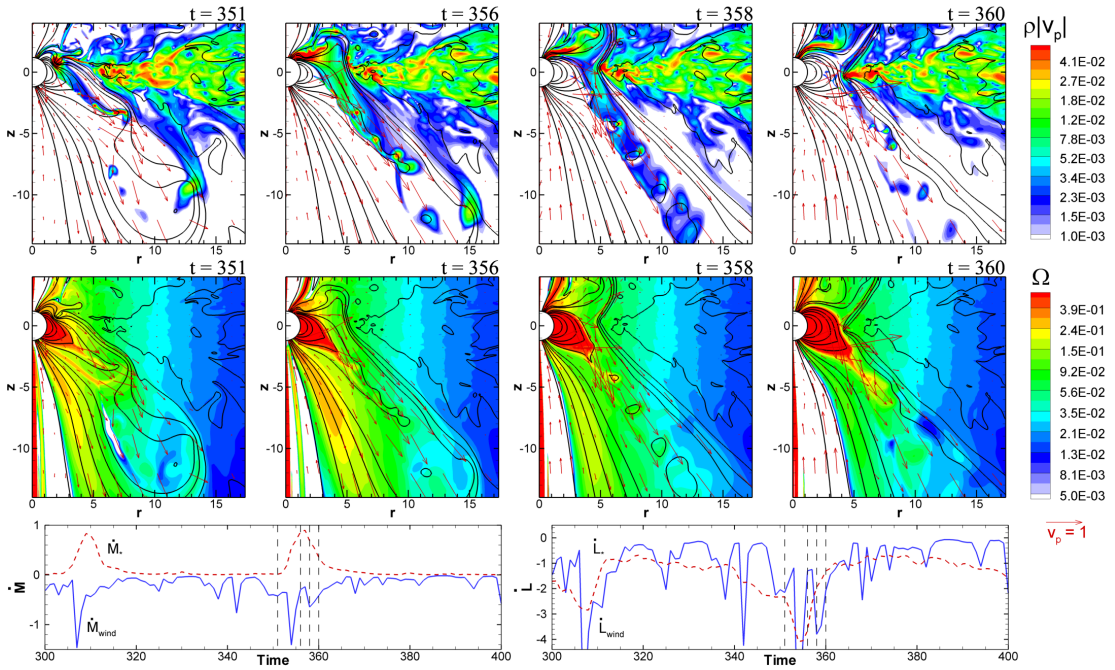

Figure 4.6: **The accreting outflow mode.** *Top panels:* four time snapshots of the propeller outflow during an accretion event. A large amount of matter is ejected into the outflow when accumulated matter funnel flows around the magnetosphere from the disc onto the star. *Middle panels:* the angular velocity Ω, velocity vectors and magnetic field lines at the same four moments in time. *Bottom panels:* the mass and angular momentum fluxes onto the star and into the wind. The vertical dashed lines correspond to the four time snapshots.

4.4.3 The magnetically-dominated outflow

We observe a second outflow component in addition to the matter-dominated propeller wind. This second component is magnetically dominated and better collimated than the propeller wind, originating along the field lines which extend out from star's polar regions. Like the propeller wind, the magnetic component is powered by the rotation of the star; the stellar rotation induces helicity in the polar field lines which in turn create a magnetic pressure gradient which accelerates the low-density matter upward away from the star. At the same time, the magnetic hoop stress collimates the outflow into a

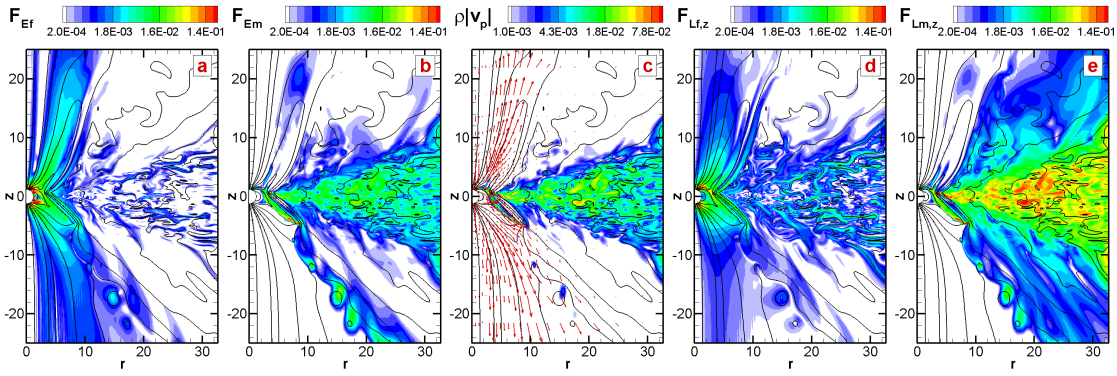

Figure 4.7: **Energy and angular momentum flux densities.** *Panels* **a** *and* **b***:* energy flux density carried by the magnetic fields, $\mathbf{F}_{Ef}$, and by matter, $\mathbf{F}_{Em}$. The lines show the magnetic field lines. *Panel* **c***:* the contours show the poloidal matter flux, ρv_p, and the red arrows show the poloidal velocity vectors. *Panels* **d** *and* **e***:* angular momentum flux density carried by the magnetic fields, $\mathbf{F}_{Lf,z}$, and matter, $\mathbf{F}_{Lm,z}$. All of the plots show the r_c=1.3 model at t=400 during the accretion-ejection phase of the cycle.

magnetic tower [Ustyugova et al., 2000, Lovelace et al., 2002].

At the edge of the simulation region, the magnetic outflow is well collimated with half-opening angles of 5-15°. The inner, magnetically-dominated core of the outflow exhibits stronger collimation than the outer regions of the outflow where there is more matter. To study the energy fluxes in the two outflow components, we measure the energy flux densities associated with the field

$$\mathbf{F}_{\rm Ef} = \frac{c}{4\pi}\mathbf{E}\times\mathbf{B} = \frac{|\mathbf{B}|^2\mathbf{v_p} - (\mathbf{B}\cdot\mathbf{v})\mathbf{B_p}}{4\pi}\,, \tag{4.5}$$

and the matter

$$\mathbf{F}_{\rm Em} = \left(\frac{\rho v^2}{2} + \frac{\gamma P}{\gamma - 1}\right)\mathbf{v_p}\,, \tag{4.6}$$

where $\mathbf{E} = -\mathbf{v}\times\mathbf{B}/c$ and $\gamma = 5/3$ for the ideal plasma in our models. Figure 4.7 shows a snapshot of the r_c=1.3 model at $t = 400$ during the accretion phase of the accumulation-accretion cycle. At this moment, the burst of accretion has resulted in a corresponding

episode of enhanced outflow. Figure 4.7a shows the energy flux in the magnetic fields at this moment in time, highlighting the magnetic outflow from the star. As matter accretes onto the star, the enhanced magnetic outflow accelerates some of the accreting matter into a high velocity ($|\mathbf{v}_p| \lesssim 2$), collimated jet. During the accretion phase when the outflow is strongest, the outflow of magnetic energy is enhanced by a factor of a few over the non-accreting phases. Figure 4.7b shows that the matter-dominated wind also carries away a substantial amount of energy from the inner disc during the brief accretion-ejection episode. Like the jet, the matter-dominated component also transports a substantial amount of magnetic energy which helps to collimate the wind as it flows out. The fast outflow associated with the magnetic jet is evident in in Figure 4.7c. The low-density matter in these polar regions is accelerated out by the magnetic pressure gradient associated with the B_ϕ component of the helical field. The outflowing field also helps to transport angular momentum directly out of the star. In §4.4.4, we discuss the role which the magnetic fields play in the spindown of the star.

4.4.4 Propeller spin down and angular momentum outflow

In the propeller regime, the star loses much of its angular momentum through the propeller and magnetic outflows. The angular momentum transfer from the star is measured by integrating the angular momentum flux densities over the stellar surface

$$\dot{L}_z = \dot{L}_{m,z} + \dot{L}_{f,z} = \int d\mathbf{S} \cdot (\mathbf{F}_{\mathrm{Lm,z}} + \mathbf{F}_{\mathrm{Lf,z}}) \, . \tag{4.7}$$

Here the normal vector for the surface $d\mathbf{S}$ points inward towards the star and $\mathbf{F}_{\mathrm{Lm,z}}$ and $\mathbf{F}_{\mathrm{Lf,z}}$ are the angular momentum flux densities carried by the matter and magnetic field, given by

$$\mathbf{F}_{\mathrm{Lm,z}} = r\rho v_\phi \mathbf{v}_p \, , \qquad \mathbf{F}_{\mathrm{Lf,z}} = -r\frac{B_\phi \mathbf{B}_p}{4\pi} \, . \tag{4.8}$$

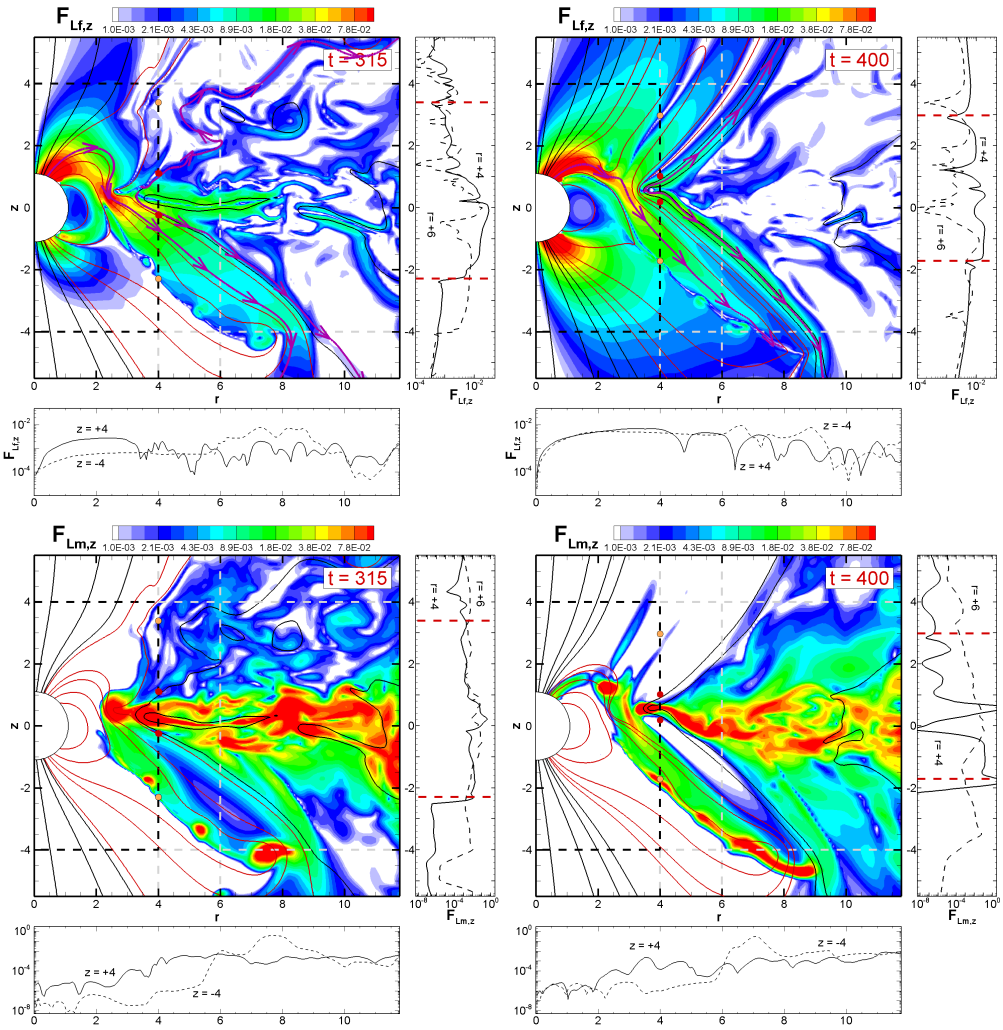

Figure 4.8: **Angular momentum flux density.** The *top panels* show contours of $\mathbf{F}_{\rm Lf,z}$ at two different times corresponding to the accumulation phase (t=315) and accretion phase (t=400) of the episodic accretion cycle. The lines trace the magnetic field lines and the purple streamtraces show the direction of the magnetic angular momentum flux. The sub-plots below and to the right of the main panels correspond to cross-sectional cuts taken at z= +4, -4 and r=4, 6 (indicated by the dashed horizontal and vertical lines in the main plots). The red dots along the r=4 vertical line delimit the disc region while the orange dots indicate the location of the neutral lines. The *bottom panels* show the same times but with contours of $\mathbf{F}_{\rm Lm,z}$.

Figs. 4.7d and 4.7e show the angular momentum fluxes carried by magnetic fields and matter at $t = 400$ in the $r_{\rm c}$=1.3 model. The angular momentum flux due to the MRI

is evident in Figure 4.7d which shows $\mathbf{F}_{\mathrm{Lf,z}}$ (see §4.6.1 for an in-depth discussion of the MRI). At the star, the angular momentum flux is entirely mediated by the magnetic fields; the star induces helicity in magnetic field lines which in turn brake the rotation of the star, leading to stellar spindown. The $\mathbf{F}_{\mathrm{Lm,z}}$ plotted in Figure 4.7e shows that, aside from the disc itself, there is a substantial amount of angular momentum flux in the matter outflowing in the propeller wind (originating from the disc-magnetosphere boundary) and in the slow disc wind (originating from the extended disc).

Figure 4.8 shows a zoomed in view of the angular momentum flux distributions near the star at both $t = 400$ (during the accretion-ejection phase of the cycle) and $t = 315$ (during the accumulation phase) of the r_{c}=1.3 model. The top panels show the angular momentum transported by the magnetic fields, $\mathbf{F}_{\mathrm{Lf,z}}$, alongside cross-sections taken at z=+4, -4 and r=4, 6 at the two different times. During the accumulation phase, matter from the inner disc penetrates into the outer magnetosphere and the star loses angular momentum through the matter-loaded field lines (streamlines in Figure 4.8). As this matter is brought into corotation with the magnetosphere, its rotational velocity exceeds the local escape velocity and it is ejected from the system. In this manner, the star efficiently transfers its angular momentum into the propeller outflow and spins down [see also analysis of Zanni and Ferreira, 2013, for the case of $r_{\mathrm{c}} \approx r_{\mathrm{m}}$]. During the accumulation phase (t=315, left panel), approximately two-thirds of the magnetic angular momentum flux out of the star goes into the propeller wind while the remaining one-third flows along the polar field lines. The vertical cross-sectional cuts through r=4 and r=6 show that $\mathbf{F}_{\mathrm{Lf,z}}$ is largest at the tip of the inner disc and in the propeller outflow. Outside of these regions, the angular momentum flux in the field falls off sharply.

The overall outflow of angular momentum increases during the short burst of accretion and ejection at the end of each cycle. This can be seen clearly in the top two panels

of Figure 4.8. During the accretion phase at $t = 400$, the magnetic outflow is strongly enhanced compared to the non-accreting phase ($t = 315$). At this point, only ~25% of the magnetic angular momentum flux is ejected along with the propeller wind (compared to ~ 66% before) while the remaining 75% outflows along the field lines above the star. In contrast, the angular momentum flux in the matter, $\mathbf{F}_{\mathrm{Lm,z}}$, is comparable in both the accumulation and accretion phases—it is $\mathbf{F}_{\mathrm{Lf,z}}$ that differs strongly in the two cases. Inside the disc, the matter carries a substantial amount of angular momentum, but the primary angular momentum transport is due to the turbulent cells associated with the MRI (discussed further in §4.6.1). The tip of the inner disc loses additional angular momentum into a weak magnetocentrifugal wind which arises from the inclined field lines that are dragged in with the matter.

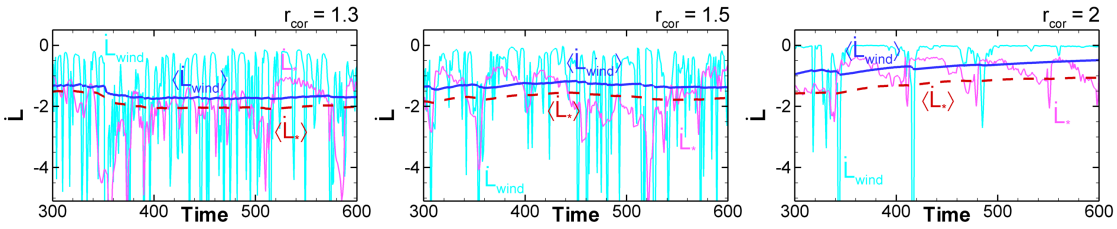

Figure 4.9: **Angular momentum fluxes in the three models.** The dark red and blue lines show the total, time averaged angular momentum flux out of the star and into the wind, respectively. The pink and light blue lines show the corresponding unaveraged total fluxes out of the star and into the wind.

To understand the effect of this angular momentum outflow on the spin-down of the star, the total angular momentum fluxes out of the star (as measured at the stellar surface) and into the wind (as measured at $r = 20$) are time averaged

$$\langle \dot{L}(t) \rangle = \frac{\int_{t_i}^{t} dt' \dot{L}(t')}{\int_{t_i}^{t} dt'}, \tag{4.9}$$

and plotted in Figure 4.9 on top of the unaveraged fluxes. In agreement with the above analysis, the time averages indicate that the majority of the stellar angular momentum is

extracted in the outflow or flows into the magnetically-dominated jet. As shown by the unaveraged $\dot{L}_*$, the episodic accretion results in a non-steady torque which is episodic in nature as well.

Using the time averaged angular momentum fluxes, we estimate spin-down timescales for the stars in each of the three models. In dimensional units, the characteristic spin-down time is

$$t_{\rm sp} = \frac{L_*}{\dot{L}} = \frac{I\Omega_*}{\dot{L}} \,, \tag{4.10}$$

where I is the star's moment of inertia. Substituting in $\dot{L} = \tilde{\dot{L}}\dot{L}_0$ and $\Omega_* = \tilde{\Omega}_*\Omega_0$ (with tildes denoting the dimensionless values) and expanding to reference units, we have

$$\begin{aligned} t_{\rm sp} = \frac{I\tilde{\Omega}_*\Omega_0}{\tilde{\dot{L}}\dot{L}_0} \qquad &= 1.22\times10^6{\rm yr}\left(\frac{I}{1.2\times10^{55}{\rm g\ cm^2}}\right)\left(\frac{M_*}{0.8{\rm M}_\odot}\right)^{\frac{1}{2}}\left(\frac{R_*}{2{\rm R}_\odot}\right)^{-\frac{9}{2}} \\ &\left(\frac{B_*}{3{\rm kG}}\right)^{-2}\left(\frac{\tilde{\mu}}{10}\right)^2\left(\frac{\tilde{\Omega}_*}{0.674}\right)\left(\frac{\tilde{\dot{L}}}{2.0}\right)^{-1} \,, \end{aligned} \tag{4.11}$$

where we have plugged in values for a 0.8 $M_\odot$, 2 $R_\odot$ cTTs with $I \approx 1.23\times10^{55}$ g cm^2 and a 3 kG surface field (see Table 4.1 for the other reference units). The spin-down timescales for each of the models is

$r_{\rm c}$ **= 1.3 :** $t_{\rm sp} \approx 1.22\times10^6$ yr $\quad(\langle\tilde{\dot{L}}_{fs}\rangle \approx 2.0)$.

$r_{\rm c}$ **= 1.5 :** $t_{\rm sp} \approx 1.16\times10^6$ yr $\quad(\langle\tilde{\dot{L}}_{fs}\rangle \approx 1.7)$.

$r_{\rm c}$ **= 2.0 :** $t_{\rm sp} \approx 1.16\times10^6$ yr $\quad(\langle\tilde{\dot{L}}_{fs}\rangle \approx 1.1)$.

The characteristic spin-down timescales are roughly the same in all three models, hovering around 1.2 megayears—comparable to the characteristic spin-down timescales found in our earlier propeller models (e.g. R05 and U06). The characteristic timescales for the three models are roughly independent of spin because the faster rotators have larger spin-down rates but also a larger amount of initial angular momentum. Table 4.3

Table 4.3: **Summary of values for a cTTs in the propeller regime.** These values are for a 0.8 $M_\odot$, 2$R_\odot$cTTs with a 3 kG surface dipole field (see Table 4.1 for other parameters). $r_c$is the corotation radius, P_* is the rotation period of the star, $\langle \dot{M}_{\rm wind} \rangle / (\langle \dot{M}_{\rm wind} \rangle + \langle \dot{M}_* \rangle)$ is the outflow ejection efficiency, t_{sp} is the spin-down timescale of the star and $\dot{\Omega}_*$ is the stellar spin-down rate.

$r_c[R_*]$	P_* [days]	$\langle \dot{M}_{\rm wind} \rangle / (\langle \dot{M}_{\rm wind} \rangle + \langle \dot{M}_* \rangle)$	$\dot{M}_{\rm wind}$ [$M_\odot$ yr^{-1}]	$t_{\rm sp}$ [Myr]	$\dot{\Omega}_*$ [s^{-2}]
1.3	1.5	0.87	2.6×10^{-8}	1.22	1.23×10^{-18}
1.5	1.9	0.74	1.8×10^{-8}	1.16	1.04×10^{-18}
2.0	2.9	0.51	1.2×10^{-8}	1.16	6.77×10^{-19}

summarizes some of the dynamical properties of each of the three models. The derived spin-down timescales are consistent with measurements of cTTs rotation periods which show that T Tauri stars older than ∼1 Myr are already slow rotators. Equation 4.11 depends on a large number of parameters—in particular, the stellar radius R_*, stellar magnetic field B_*, and the dimensionless magnetic moment $\tilde{\mu}$ which determines the size of the magnetosphere relative to the star. If the young star has a stronger magnetic field or larger radius than the given reference star, it will spin down even more rapidly than the reference star.

For parameters relevant to accreting millisecond pulsars, we estimate spin-down timescales of

$$t_{\rm sp} = \frac{I\tilde{\Omega}_*\Omega_0}{\tilde{\dot{L}}\dot{L}_0} = 1.27 \times 10^9 {\rm yr} \left(\frac{I}{2.78 \times 10^{45} {\rm g\ cm^2}}\right) \left(\frac{M_*}{1.4 M_\odot}\right)^{\frac{1}{2}} \left(\frac{R_*}{10 km}\right)^{-\frac{9}{2}} \left(\frac{B_*}{3 \times 10^8 {\rm G}}\right)^{-2} \left(\frac{\tilde{\mu}}{10}\right)^2 \left(\frac{\tilde{\Omega}_*}{0.674}\right) \left(\frac{\tilde{\dot{L}}}{2.0}\right)^{-1}, \quad (4.12)$$

where we have plugged in the corresponding values from Table 4.1.

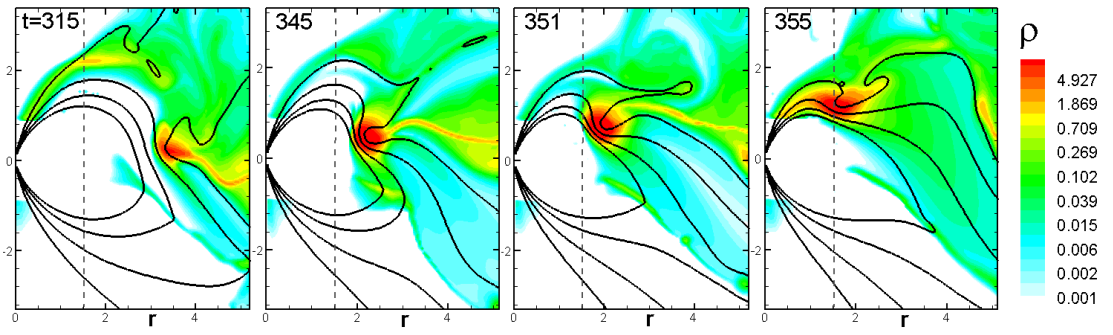

Figure 4.10: **Diffusive penetration through the magnetosphere.** The snapshots of the $r_c = 1.5$ model with diffusivity show the gradual diffusive penetration of the disc matter through several field lines of the outer magnetosphere. The color background shows the density distribution with red indicating the maximum density and light-cyan indicating the smallest density in the disc. There is also an even lower density corona which is shown in white.

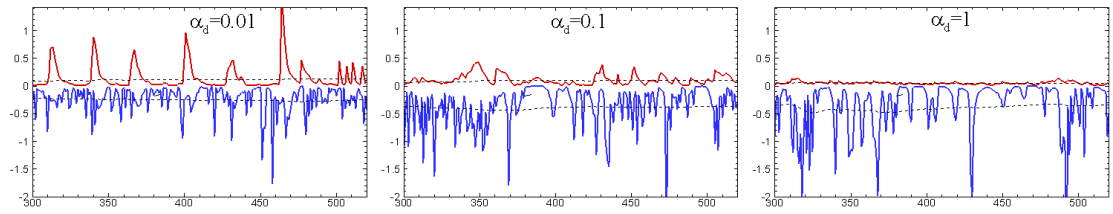

Figure 4.11: **Fluxes in the models with diffusion.** Matter fluxes to the star (top curves) and to the wind (bottom curves) in the $r_c = 1.5$ model with diffusivity. The fluxes are calculated through the surface $r = 20$, $z = 20$ and restricted by velocity $v > 0.2$, for different values of α_d.

4.5 Diffusivity and outflows

The MRI turbulence provides a mechanism for angular momentum transport in the disc and permits inward accretion from larger distances. However, it does not act as a source of diffusivity at the disc-magnetosphere boundary [Romanova et al., 2011]. In spite of the MRI-driven turbulence, the accretion disc is matter-dominated and its dynamics are similar to a non-magnetized disc. The inner disc rotates at the Keplerian velocity

Table 4.4: **Summary of results for the diffusive runs.** All runs were performed for r_c= 1.5. α_d is the diffusivity parameter, ρ_d is the threshold density for diffusivity, $\langle \dot{M}_{\rm wind} \rangle$ and $\langle \dot{M}_* \rangle$ are time-averaged values of matter flux to the wind and to the star, respectively. The ratio $\langle \dot{M}_{\rm wind} \rangle / (\langle \dot{M}_{\rm wind} \rangle + \langle \dot{M}_* \rangle)$ is the outflow ejection efficiency of the propeller. $\langle \dot{L}_* \rangle$ is the angular momentum flux from the surface of the star.

	base case	ρ_d = 0.01		
α_d	0.0	0.01	0.1	1
$\langle \dot{M}_{\rm wind} \rangle$	0.27	0.26	0.4	0.34
$\langle \dot{M}_* \rangle$	0.09	0.11	0.08	0.05
$\frac{\langle \dot{M}_{\rm wind} \rangle}{\langle \dot{M}_{\rm wind} \rangle + \langle \dot{M}_* \rangle}$	0.74	0.70	0.83	0.86
$\langle \dot{L}_* \rangle$	1.7	2.0	2.7	2.25

whereas the magnetosphere is super-Keplerian and they do not interact unless there is a mechanism for diffusivity which provides penetration of the disc matter through the magnetosphere.

In the ideal MHD simulations presented in this chapter, the matter in the inner disc gradually penetrates through the external magnetosphere due to the numerical diffusivity. Figure 4.10 shows several snapshots of the accumulation of matter in the inner disc, the slow diffusive penetration through the external field lines of the magnetosphere, and the resulting outflow launched along the inflated stellar field lines. The numerical diffusivity is low because the grid resolution is very high in the disc. However, even with the low diffusivity, the diffusive penetration of matter is possible when the velocity of diffusive penetration, $v_{\rm diff} \approx \eta/\Delta r$ (where Δr is the diffusion length scale), is comparable to the advection velocity v_r of the inner edge of the disc. Initially when $v_r \geq v_{\rm diff}$, the matter in the disc compresses the magnetospheric field lines inward until the matter and magnetic pressures come to an equilibrium (i.e. β_1 approaches 1). At this point the magnetosphere halts the accretion and v_r falls below $v_{\rm diff}$ bringing the matter into the diffusive regime. Even when the diffusivity is low, the matter at the disc-magnetosphere

boundary can penetrate into the outer magnetosphere.

The Rayleigh-Taylor and Kelvin-Helmholtz instabilities may be in large part responsible for the mixing of the matter and field at the disc-magnetosphere boundary [Arons and Lea, 1976]. In 3D, these mechanisms may serve as the primary source of diffusivity in the magnetosphere. The Kelvin-Helmholtz instability may be important because the inner disc matter rotates slower that the external magnetosphere. In the propeller regime, the Rayleigh-Taylor instability cannot act in its usual form because the presence of an inward pointing effective gravity is required [Spruit et al., 1995, Kulkarni and Romanova, 2008]. However, it may operate in the opposite direction, driven by the outward pointing centrifugal force. The enhancement of diffusivity can strongly influence the rate of accretion and outflows in the propeller regime.

To investigate the role of diffusivity in our axisymmetric simulations, we developed a non-ideal version of our MHD code by adding diffusivity terms to our MHD equations. The diffusivity coefficient is proportional to the Shakura and Sunyaev [1973] α parameter. We take $\alpha = \alpha_d$ inside the radius $r < 5$ where the inner disc interacts with the magnetosphere, and $\alpha = 0$ at larger radii so that the MRI-driven accretion proceeds normally in the rest of the disc (otherwise, the high diffusivity can damp the MRI). We also introduce a threshold density ρ_d below which the diffusivity is not applied so that only the matter in the disc is diffusive.

As a base, we take the case of a propelling star with the corotation radius $r_c = 1.5$ and vary the diffusivity between $\alpha_d = 0.01, 0.1$ and 1 (see Table 4.4). We also take a threshold density of $\rho_d = 0.01$ to ensure that only the disc matter is diffusive. In each simulation, we calculate fluxes of matter onto the star $\dot{M}_*$ and into the wind $\dot{M}_{\rm wind}$. The fluxes into the wind are calculated through the surface $z = 20, r = 20$ for velocities $v_p > 0.2$. The top curves in Figure 4.11 show that the flux onto the star systematically

decreases with increasing α_d and becomes less spiky, whereas the matter flux to the wind becomes somewhat larger. This dependence of fluxes on diffusivity can be easily understood: at larger values of α_d, matter diffuses more efficiently through the field lines and is ejected faster than it can accumulate at the disc-magnetosphere boundary. In cases of low diffusivity, the situation is the opposite: the accreting matter does not efficiently diffuse through the field lines, instead accumulating at the disc-magnetosphere boundary where it eventually overflows onto the star or is ejected into the outflow. This episodic accumulation-overflow results in the spikes in accretion which are observed.

We calculate averaged fluxes onto the star and into the wind using Equation 4.4. We expect that higher diffusivities will result in a higher outflow efficiency and indeed, we find that the accretion rate onto the star $\langle \dot{M}_* \rangle$ systematically decreases with diffusivity in our simulations. Matter flux to the wind $\langle \dot{M}_{\rm wind} \rangle$ increases for $\alpha_d = 0.1$ then decreases again when the diffusivity becomes too high at $\alpha_d = 1$. The angular momentum flux from the star, $\langle \dot{L}_\star \rangle$ (which determines the spin-down of the star), correspondingly increases, then decreases. It has a maximum value of 2.7, which is only 1.7 times larger than that in case of $\alpha_d = 0$. Therefore, if additional diffusivity were to be included in our base models, the spindown rate of the star may increase, but only by a factor of $\sim$2. As expected, the efficiency of the propeller $\langle \dot{M}_{\rm wind} \rangle / (\langle \dot{M}_{\rm wind} \rangle + \langle \dot{M}_* \rangle)$ systematically increases with α_d.

The analysis presented here shows that the larger diffusivities expected in more realistic three-dimensional simulations may lead to somewhat stronger outflows and shorter spindown timescales for the propelling stars. These larger diffusivities model the mixing instabilities at the disc-magnetosphere boundary which we do not see in our 2.5D simulations. Our investigation shows that the difference between the cases with low and high diffusivity is not substantial, differing only by a factor of 2. For the same accretion

rate in the disc, approximately the same amount of matter is ejected to winds due to propeller mechanism, roughly independent of α_d. In the less diffusive runs, the ejection occurs episodically in bursts whereas in the more diffusive runs the process is smoother as the episodic accretion cycle is suppressed. On average, however, the matter fluxes are comparable.

4.6 Discussion

4.6.1 The effect of the MRI

In this work, the MRI turbulence serves as the main source of viscosity in the disc and helps to regulate the accretion rate. The effective viscosities can be estimated using the standard definitions of the α-disc model where the stresses are proportional to the matter pressure in the disc [Shakura and Sunyaev, 1973]. In an MRI-driven disc, angular momentum is transported due to the matter stress T_m and magnetic stress T_f. The corresponding α-viscosity parameters can be estimated by calculating the ratio between the vertically averaged stresses and the matter pressure

$$\alpha_m = \frac{2}{3}\frac{\langle T_m \rangle}{\langle P_m \rangle}\,, \quad \alpha_f = \frac{2}{3}\frac{\langle T_f \rangle}{\langle P_m \rangle}\,, \tag{4.13}$$

where α_m and α_f are the effective viscosity coefficients due to the matter and the field, respectively. The stresses due to the matter and field are

$$\langle T_m \rangle = \frac{1}{2H}\int dz \rho v_r v_\phi - \langle \rho v_r \rangle \langle v_\phi \rangle\,, \quad \text{and} \quad \langle T_f \rangle = -\frac{1}{2H}\int dz \frac{B_r B_\phi}{4\pi}\,, \tag{4.14}$$

where

$$\langle v_\phi \rangle = \frac{1}{\Sigma}\int dz \rho v_\phi, \;\; \langle \rho v_r \rangle = \frac{1}{2H}\int dz \rho v_r, \tag{4.15}$$

$\Sigma = \int dz\rho$ is the disc surface density and $2H$ is the total thickness of the disc. The vertically averaged pressures are

$$\langle P_m \rangle = \frac{1}{2H} \int dz\, P, \quad \langle P_f \rangle = \frac{1}{2H} \int dz\, \frac{\mathbf{B}_{tot}^2}{8\pi}. \tag{4.16}$$

Figure 4.12 shows the radial distribution of the $\alpha-$parameters and the vertically averaged stresses and pressures at t=397 in the r_c= 1.3 model. At this moment in time, the inner disc is in the non-accreting phase of the episodic accretion cycle and the magnetosphere extends out to $r_m \approx 5-7$ (see bottom panel). Since the disc is highly turbulent, the stress and α profiles vary in time, especially near the disc-magnetosphere boundary where the matter is strongly influenced by the magnetosphere. In the bulk of the disc, we measure effective viscosities of $\alpha_m = 0.001 - 0.03$ and $\alpha_f = 0.02 - 0.1$ with α_f a few times α_m in general.

In the bulk of the disc, $\alpha_f \approx 0.02$ and $v_r \lesssim 0.01 v_{\rm Kep}$. The number of turbulent cells per disc thickness decreases from 10-20 at large radii to 1-2 in the inner disc (r = 5–7), where the disc height is small and the magnetic field is large with β ~1–10. The stellar magnetic field does not penetrate far into this region of the disc and as such, has little influence on the MRI. However, the magnetic field in the inner regions is large due to the azimuthal wrapping of the field lines by the Keplerian disc. This stronger field results in a magnetic stress which is more than an order of magnitude larger in the inner regions than in the bulk of the disc (e.g. middle panel of Figure 4.12). Inside the magnetosphere ($r \lesssim 5$), the matter pressure is very low and hence the nominal values of α_m and α_f both are high (see Equation 4.13). However, since these radii correspond to the region inside the magnetosphere, they are not relevant to the analysis of the disc.

The interaction between the rapidly-rotating magnetosphere and slower-rotating inner disc depends on the diffusivity in this region. In our simulations, the only source of diffusivity is the numerical diffusivity, which is small due to the high grid resolution at

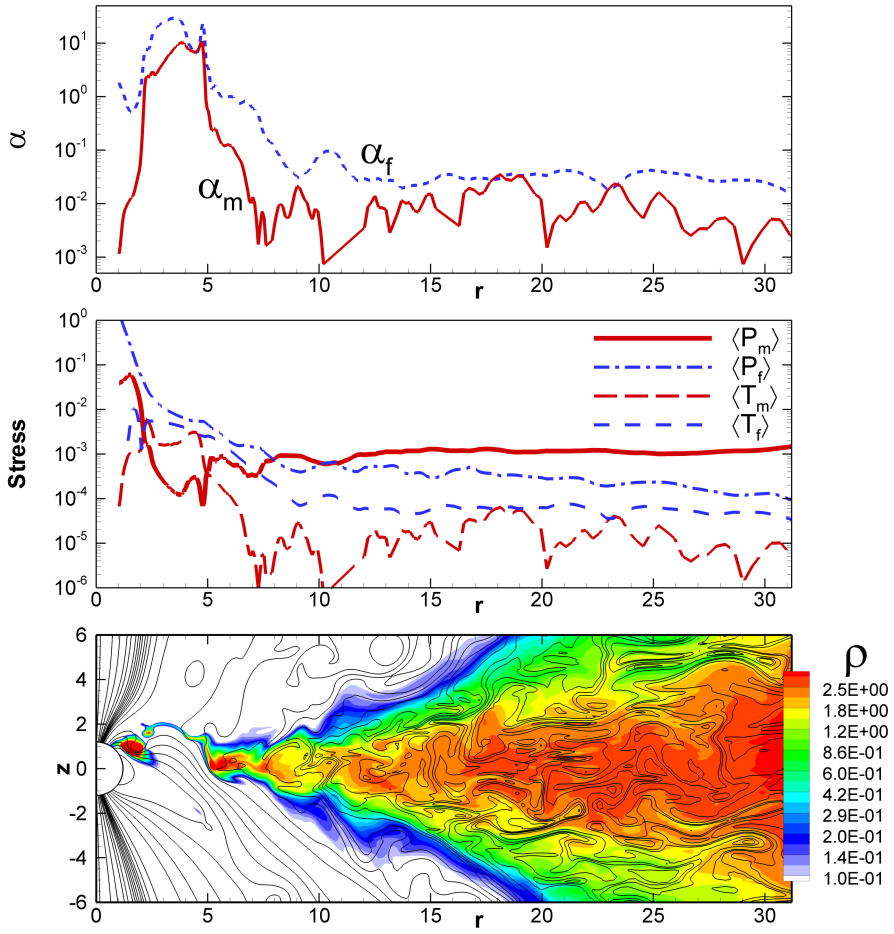

Figure 4.12: **Radial distribution of stresses in the disc.** The top panel shows the effective viscosities due to the matter, α_m, and the field, α_f. Inside the magnetosphere, the matter pressure is small and both effective αs are large. In the remainder of the disc, α_f is a few times α_m, indicating that the MRI is the dominant source of viscosity in the disc. The middle panel shows the z-averaged stresses and pressures inside the disc. The bottom panel shows a snapshot of the r_c=1.3 model at t=397, from which the effective αs are calculated.

the disc-magnetosphere boundary. Nonetheless, there is sufficient interaction between the magnetosphere and disc to drive the propeller outflow. However, in physical systems, the effective diffusivity may be larger due to instabilities in this interaction region. In §4.5, we study the effects of a larger diffusivity on the propeller outflow by enabling the code's diffusivity module and applying it to the matter near the disc-magnetosphere

boundary. The larger diffusivity generally increases the outflow rate, but only by a factor of two even in the most diffusive cases.

4.6.2 The one-sided propeller wind

The geometry of the stellar magnetosphere plays a key role in the launching of the propeller outflow. In the axisymmetric models, the aligned dipole is initially equatorially symmetric. However, as soon as the matter from the disc reaches the magnetosphere, the stellar dipole is deflected to one side and this initial top-bottom symmetry is broken. This asymmetry helps to drive the one-sided outflows observed in this work as it provides a preferential direction for the matter accretion and ejection. For the simple dipole magnetosphere, occasional "flip-flops" are observed where the direction of the outflow switches sides. Lovelace et al. [2010] modeled a star with a superposition of dipole and quadrupole fields, finding that this configuration can drive one-sided outflows despite the field being initially axially and equatorially symmetric. Like the simulations presented here, Lovelace et al. [2010] also found that a purely dipolar field drives one-sided outflows which can occasionally flip sides. Dyda et al. [2015a]showed that the degree of asymmetry depends on the degree of magnetization of the accreting disc.

The presence of a complex magnetic topology on a star may also help to drive one-sided outflows. Most cTTs's have fields which are inclined relative to the rotation axis—a configuration which is intrinsically non-axisymmetric. Additionally, several cTTs's are known where the higher order components are comparable to or stronger than the dipole components [e.g. BP Tauri, V2129 Oph, Donati et al., 2008, 2011]. While the dipole may dominate the dynamics at larger distances in the disc, these higher order components play a major role in the dynamics near the star. Axisymmetric simulations

do not capture cases such as the one where the dipole field on the western hemisphere of the star is deflected in the opposite direction than the field on the eastern hemisphere. However, these effects tend to enhance the one-sided nature of the outflow as they contribute to the asymmetry of the magnetosphere. Further MHD simulations in full 3D are necessary to study these magnetospheric dynamics.

4.6.3 Comparison with previous works

In prior numerical studies of the propeller regime [e.g. R05, U06, and Romanova et al., 2009], propeller-driven outflows were observed from α-discs where both the viscosity and diffusivity were modeled using the Shakura and Sunyaev α-disc approximation [Shakura and Sunyaev, 1973]. These previous works examined the outflows using an equatorially and axially symmetric (i.e. quarter-region) grid in spherical coordinates, finding that propeller outflows are ubiquitous for a large range of stellar and disc parameters. The present work utilizes a much higher resolution cylindrical grid without the requirement of equatorial symmetry where the source of the viscosity is the MRI-driven turbulence and the source of diffusivity is the small numerical diffusivity in the code. Despite these differences, the observed outflows are similar to the outflows observed in prior works. The main differences are associated with the different parameters used in the models as well as the removal of the requirement of symmetry about the equatorial plane.

In both the new and old studies, we observe the cyclic magnetospheric oscillations which arise due to the episodic accumulation and accretion-ejection of matter from the disc. The variable matter flux shown in Figure 3 of R05 is very similar to the $\dot{M}_{\rm wind}$ of the $r_{\rm c} = 1.3$ model shown in the left panel of Figure 4.4. The outflow rate is somewhat

higher in R05 due to the faster rotation of the star (r_c=1). The effective viscosity provided by the MRI in the inner disc ($\sim 0.1 - 1$) is comparable to the viscosities used in the base cases of R05 and U06 where $\alpha_v = 0.1 - 0.2$. However, one major difference is that the numerical diffusivity, α_d, in this work is roughly 0.01 which is much smaller than that used in R05 and U06.

U06 undertook a parameter space study and performed simulations for a wide range of viscosity and diffusivity parameters, α_v and α_d (see Figure 14-16 of U06). They derived the dependence of matter and angular momentum fluxes on these parameters and found that the torque on the star has a weak dependence on α_d. This is in agreement with the test simulations presented in §4.5. One key difference is that U06 found that the outflow tends to weaken with lower diffusivity. However, in the present models, strong outflows are still observed even though the diffusivity is small. This difference is associated with the breaking of the equatorial symmetry: in the prior works, the requirement of equatorial symmetry prevented simultaneous accretion and ejection. However in this work, the outflow is launched from one side of the magnetosphere even as matter accumulates and diffuses on the opposing hemisphere. Another difference between the older and present works is that in U06, $\dot{M}_*$ steadily increases with α_d (see Figure 14 of U06), whereas in our test simulations, the accretion rate *decreases* with α_d. This difference is also connected with the fact that the accreting matter is not trapped by the requirement of symmetry about the equatorial plane.

In both the older and present studies of the propeller regime, most of the matter flows into the conical-shaped winds while a significant part of the energy and angular momentum is carried away by the collimated, magnetically-dominated outflow. In the older models, the stellar angular momentum is primarily lost to the Poynting flux jet or through the field lines which are inflated by the propeller wind (N_s in Figure 16 of U06).

A smaller fraction of the angular momentum is transported from the star into the inner disc. This angular momentum subsequently flows from the disc into the propeller wind.

In the new models, a substantial amount of the angular momentum is lost into the propeller wind itself. The stellar magnetic field mediates the angular momentum exchange between the star and the matter which has accumulated at the disc-magnetosphere boundary. This angular momentum outflows from the star and provides the centrifugal acceleration which drives the propeller outflow. However, as in the older models, some of the angular momentum outflows along the collimated field lines extending out from the polar regions of the star.

The spin-down torque in the present model is about 2 times smaller than that of R05 and U05 (largely due to the slower rotation of the star). This results in a longer spin-down timescale compared to the older models. Nonetheless, the models presented here exhibit good agreement with the older models of propeller-driven outflows. In the new work, the self-consistent, MRI-driven turbulence and the breaking of equatorial symmetry together lead to several of the important differences we discuss above.

4.6.4 The propeller regime in transitional pulsars

Millisecond pulsars arise from slowly rotating neutron stars which accrete mass and angular momentum from a binary donor star undergoing Roche lobe overflow. During this accreting phase, these systems are typically X-ray bright and referred to as low-mass X-ray binaries (LMXBs). If the mass transfer from the donor declines, the accretion rate declines correspondingly and the neutron star transitions from accretion to rotation power, resulting in the emergence a radio-bright millisecond pulsar. However, prior to 2013, the link between the accretion and rotation-powered states had only been observed

indirectly [Burderi et al., 2003, Hartman et al., 2008, di Salvo et al., 2008, Patruno, 2010, Papitto et al., 2011].

Papitto et al. [2013] reported the first definitive observations of a pulsar swinging between the accretion and rotation powered stages in the X-ray transient IGR J18245-2452. During the transitional phase, the accretion rate onto the pulsar declines and the magnetosphere expands outward, likely pushing the system into the propeller regime of accretion. Models of IGR J18245-2452's spectrum by Ferrigno et al. [2014] are suggestive of the presence of outflows driven from the system. The outflows may indicate the onset of the strong propeller regime where the outflow efficiency is high and direct accretion onto the star is inhibited, similar to the centrifugally-launched outflows investigated in this chapter.

A number of additional accreting millisecond pulsars have been identified which also exhibit signatures of propeller regime accretion and outflows [Papitto et al., 2014, Papitto and Torres, 2015]. One such system, SAX J1808.4-3658, has experienced outbursts thought to be associated with a sudden increase of the mass accretion rate on to the pulsar. During the declining post-outburst phase, large luminosity variations are observed which are attributed to the onset of the propeller regime [Campana et al., 2008]. 1-5 Hz x-ray flaring has been observed during this onset: this flaring has been interpreted as the emergence of the episodic accumulation-accretion cycle described by Spruit and Taam [1993] and D'Angelo and Spruit [2010] and modeled in this chapter. Currently, no outflow signatures have been observed in SAX J1808.4-3658 suggesting that the flaring may be arising in the weak propeller regime of accretion.

4.7 Chapter summary

In this chapter, we have presented high-resolution simulations which have been used to study propeller-driven outflows from a realistic disc accreting due to MRI-driven turbulence. In the propeller regime of accretion, the star (and its magnetosphere) rotates faster than the Keplerian angular velocity of the inner accretion disc, resulting in a large centrifugal barrier at the disc-magnetosphere boundary. As we are interested in propeller-driven outflows, we study the "strong propeller" regime where $r_{\rm m}$ is a few times larger than $r_{\rm c}$ and outflows will be launched efficiently. The main conclusions of this chapter are as follows:

1. Stars accreting in the strong propeller regime can drive outflows. The rapidly-rotating magnetosphere behaves as a centrifugal barrier which inhibits matter from accreting onto the star. Instead, the accreting matter accumulates at the disc-magnetosphere boundary over time and diffuses through the outer magnetosphere into the more rapidly rotating inner regions. Inside the magnetosphere, it picks up angular momentum from the field lines, becomes super-Keplerian and inflates the stellar field, creating a path for the matter to flow out of the system. As the matter flows away the field lines reconnect, releasing magnetic flux and matter from the magnetosphere and truncating the outflow into discrete plasmoids. This matter-dominated propeller wind is ejected with a half-opening angle of 45° and gradually collimates at larger distances.

   The remainder of the matter which does not flow out instead undergoes an episodic accretion-ejection cycle. As the matter accumulates at the disc-magnetosphere boundary, the magnetosphere is slowly compressed towards the star. Eventually, the gravitational force becomes dominant and the matter deflects the magnetosphere to one side, accreting onto the star as a magnetospheric funnel flow. A

significant fraction of this accreting matter is driven into an outflow, resulting in a temporarily enhanced outflow rate. Once the accumulated matter is depleted, the stellar magnetosphere quickly re-expands to halt the accretion onto the star. The enhanced outflow results in the ejection of a larger amount of magnetic flux which helps to collimate the matter, giving a narrower half-opening angle (compared to the non-accreting phase) of 20–40° at the outer edge of the simulation region.

2. The propeller outflow has two main components: a high density, medium velocity, matter-dominated wind and a low density, high velocity, magnetically-dominated Poynting jet. The matter in the Poynting jet is magnetically accelerated and collimated by the helically wound magnetic field lines extending out from the polar regions of the star. It carries substantial amounts of magnetic energy away from the star and has a half-opening angle of 5–15° at the edge of the simulation region. The slower moving, matter-dominated propeller wind is launched from the disc-magnetosphere boundary by the centrifugal force and helps to remove matter and angular momentum from the disc and the star. Despite being matter dominated, the propeller wind also carries magnetic flux which acts to weakly collimate the outflow. We observe weak collimation in our simulation region, but the magnetic hoop-stress is expected to continue collimating the flow resulting in a well-collimated jet at large distances from the star.

3. Stars in the propeller regime experience a spin-down torque through the Poynting jet as well as the matter loaded magnetic field lines which launch the propeller wind from the disc-magnetosphere boundary. The more rapidly rotating stars have higher spin-down rates and in all three of our models, we measure characteristic spin-down timescales of around 1.2 Myr for a typical cTTs with a strong 3 kG surface field (other parameters can be found in Table 4.1).

CHAPTER 5

PLANET MIGRATION AT THE DISC-CAVITY BOUNDARY

5.1 Background and overview

Nascent planets in protoplanetary discs can migrate inward or outward by exchanging angular momentum through tidal interactions with the disc. The importance of these interactions in the evolution of planet orbits was recognized and developed early on by Goldreich and Tremaine [1979, 1980]. For planets undergoing Type I migration (in which the planet does have enough mass to substantially perturb the disc density profile), the tidal torque consists of two components: the differential Lindblad torque and the corotation torque [Goldreich and Tremaine, 1979]. The Lindblad torque arises from the generation of spiral density waves excited by the planet at the Lindblad resonances. In a Keplerian disc, the Lindblad resonances lie at the locations where the planet's orbital angular velocity is a whole number ratio of the matter orbital angular velocity $m\Omega_p = (m \pm 1)\Omega$. Thus the location of the resonances are

$$r_{\rm LR} = \left(1 \mp \frac{1}{m}\right)^{2/3} r_p \,, \tag{5.1}$$

where m is the order of the resonance. The minus sign refers to the inner Lindblad resonances (ILR) while the plus sign refers to the outer Lindblad resonances (OLR). The torque from the ILR tends to be positive while the torque from the OLR tends to be negative. The difference between the opposing torques from the ILR and OLR (known as the *differential Lindblad torque*) determines the migration direction—typically inward for a planet embedded in a protoplanetary disc [Ward, 1986, 1997].

This migration may be modified by the action of the corotation torque which arises from the material in the planet's co-orbital region where $\Omega = \Omega_p$. The role of the coro-

tation torque in planet migration has been studied recently by a number of authors [e.g., Paardekooper and Mellema, 2006, Baruteau and Masset, 2008, Paardekooper and Papaloizou, 2009, Kley et al., 2009, Masset and Casoli, 2009, 2010, Paardekooper et al., 2010, 2011, Paardekooper, 2014]. The co-orbiting material undergoes a horseshoe-shaped orbit in the vicinity of the planet and asymmetries in the corotation region can result in the exchange of angular momentum between the planet and disc matter. This torque is especially important when the density profile of the disc has some structure (such as at a gap or cavity in the disc). In these regions, the magnitude of the corotation torque may dominate over the differential Lindblad torque if the surface density gradient in the disc is larger than some fiducial value [see Tanaka et al., 2002]. This effect is especially non-negligible there is a sharp density gradient such as at the edge of the disc-magnetosphere boundary [e.g., Lin et al., 1996, Romanova and Lovelace, 2006].

Migrating protoplanets may encounter gaps or cavities in the disc present due to the influence of other planets, the star, or associated with transition regions in the disc, such as a dead zone, magnetospheric boundary or the dust sublimation radius. Lin et al. [1996] considered the case of a planet which migrates into the magnetospheric cavity and halts when its lowest-order OLR falls inside the cavity. Rice et al. [2008] studied this scenario in 2D hydrodynamic simulations and found that high-mass planets can undergo eccentricity growth while migrating inside the cavity whereas low-mass planets which migrate into the cavity simply stall in their migration. Kuchner and Lecar [2002] considered a similar scenario where planets migrate and halt inside an inner gap evacuated by the onset of efficient accretion due to the magnetorotational instability. Matsumura et al. [2007] considered the case of planet migration into a cold dead zone where the accretion is inefficient, finding that even low mass planets can open gaps due to the low viscosity in the dead zone, thereby slowing their migration significantly.

Masset et al. [2006] studied the effect of the corotation torque on the migration of planets in the vicinity of a *cavity edge* using 2D hydrodynamic simulations. In the study, super-Earth type planets with masses 5-15 $M_\oplus$ were allowed to migrate in an accretion disc with a lower-density central cavity (with $\Sigma_{\rm disc} \approx 4\Sigma_{\rm cavity}$). Far from the cavity boundary, the planets migrate inward as usual due to the differential Lindblad torque. However, as the planets approach the density transition, the authors find that the corotation torque contributes a positive torque, creating a stable *planet trap* where the net torque is zero and inward migration is halted. Instead of migrating into the cavity [as is expected if the Lindblad resonance is dominant, Lin et al., 1996, Kuchner and Lecar, 2002], the planets halt while they are still in the disc due to the action of the corotation resonance. Morbidelli et al. [2008] investigated the planet trap mechanism as a method for avoiding the inspiral problem, focusing on the case where planet embryos are trapped at a cavity boundary, allowing for gradual buildup of giant-planet cores. A single disc may have several such planet traps at the dust sublimation radius, at the inner edges of dead zones or ice lines, as well as at the magnetospheric gap where the star truncates the inner disc [Ida and Lin, 2008, Lyra et al., 2010, Hasegawa and Pudritz, 2011].

More massive planets ($M_p \gtrsim 1 M_J$) clear out the material in the co-orbital region and migrate in the Type II regime, meaning that the corotation torque never becomes important. Instead, when these planets encounter a low-density region in the disc, they continue migrating inward until the $m = 1$ OLR lies interior to the inner edge of the disc and the planet can no longer efficiently transfer angular momentum into the disc matter [Rice et al., 2008].

In this chapter, we study the lower-mass regime of super-Earth class ($M_p = 15 M_\oplus$) planets migrating near a central low-density cavity using hydrodynamic simulations.

The problem is considered in both global 3D models in cylindrical coordinates as well as in 2D polar coordinates to facilitate comparison. In particular, we study three primary cases of migration of: 1) a planet with an initial orbit inside a low-density cavity; 2) a planet with an initial orbit inside the higher-density disc; and 3) a planet with an initial orbit coinciding with the disc-cavity boundary. In §5.2 we discuss the problem setup in the 3D and 2D models. In §5.3, we detail the results of the 3D simulations for the three aforementioned cases. And lastly, in §5.4, we compare the 3D models with the 2D models and discuss various applications of the work in detail.

5.2 Numerical setup

Here, we describe the numerical setup of our hydrodynamic simulations of planet migration. Our code has a hydrodynamics module which models the gas dynamics in the disc as well as a planet module which computes the orbital trajectory of the planet which migrates under the influence of the gravity from the disc and star. In our model, the planet and disc only interact gravitationally and the disc is assumed to have negligible self-gravity. We investigate this problem in global 3D cylindrical $\mathbf{r} = (r, \phi, z)$ coordinates implemented in a Godunov-type code recently developed by our group (Koldoba et al. 2015, in prep). For comparison, we also perform analogous 2D simulations in polar coordinates with parameters that are similar to those in the 3D simulations.

5.2.1 The equations of hydrodynamics

Our 3D models are based on the equations of hydrodynamics which can be compactly written as

$$\partial_t \boldsymbol{U} + \nabla \cdot \boldsymbol{F}(\boldsymbol{U}) = \boldsymbol{Q} \,, \tag{5.2}$$

where $\boldsymbol{U}$ is the vector of conserved variables and $\boldsymbol{F}(\boldsymbol{U})$ is the vector of fluxes

$$\boldsymbol{U} = [\rho, \rho s, \rho \boldsymbol{v}]^T \,, \quad \boldsymbol{F}(\boldsymbol{U}) = [\rho \boldsymbol{v}, \rho \boldsymbol{v} s, \boldsymbol{M}]^T \,, \tag{5.3}$$

and $\boldsymbol{Q} = [0, 0, -\rho \nabla \Phi]$ is the vector of source terms. In the above equations, ρ is the fluid density, $s \equiv p/\rho^\gamma$ is the entropy per unit mass with $\gamma = 5/3$, $\boldsymbol{v}$ is the velocity vector, Φ is the gravitational potential of the star-planet system (given later on in this section) and $\boldsymbol{M}$ is the momentum tensor, with components

$$M_{ij} = \rho v_i v_j + \delta_{ij} p \tag{5.4}$$

where δ_{ij} is the Kronecker delta function and p is the fluid pressure. Our model does not include viscosity and solves the entropy conservation equations in place of the full energy equation. This approximation is valid as strong shocks are not expected to be important in the problem studied here.

We also investigate the migration of planets in 2D coordinates. In 2D, the equations of hydrodynamics are analogous to the 3D equations and are solved for the height averaged analogs of the state variables in Equation 5.3

$$\boldsymbol{U}_{\rm 2D} = [\Sigma, \Sigma S, \Sigma \boldsymbol{v}]^T \,, \quad \boldsymbol{F}_{\rm 2D}(\boldsymbol{U}) = [\Sigma \boldsymbol{v}, \Sigma S \boldsymbol{v}, \boldsymbol{M}_{\rm 2D}]^T \,. \tag{5.5}$$

Here $\Sigma \equiv \int_{-\infty}^{\infty} \rho dz$ is the surface density, $S \equiv \Pi/\Sigma^\gamma$ is the height-averaged entropy analog, $\Pi \equiv \int_{-\infty}^{\infty} p dz$ is the surface pressure, and

$$\boldsymbol{M}_{\rm 2D} = \begin{bmatrix} \Sigma v_r^2 + \Pi & \Sigma v_r v_\phi \\ \Sigma v_\phi v_r & \Sigma v_\phi^2 + \Pi \end{bmatrix} \tag{5.6}$$

is the two dimensional momentum tensor.

The gravitational potential of the star-planet system is given by

$$\Phi = -\frac{GM_*}{|\mathbf{x}|} - \frac{GM_p}{(|\mathbf{x}-\mathbf{x}_p|^2+\epsilon^2)^{1/2}} + \frac{GM_p}{|\mathbf{x}_p|^3}\mathbf{x}\cdot\mathbf{x}_p \tag{5.7}$$

where ϵ is a smoothing radius which is added to prevent divergence at the planet's location [Fromang et al., 2005, Nelson et al., 2000]. In our models, we take

$$\epsilon = 2r_{\rm Hill} \approx 0.025,$$

where $r_{\rm Hill} = r_p(M_p/3M_*)^{1/3}$ is the planet's Hill radius. The corresponding force per unit mass $\mathbf{a} = -\nabla\Phi$ is

$$\mathbf{a} = -\frac{GM_*}{|\mathbf{x}|^3}\mathbf{x} - \frac{GM_p}{(|\mathbf{x}-\mathbf{x_p}|^2+\epsilon^2)^{3/2}}(\mathbf{x}-\mathbf{x_p}) - \frac{GM_p}{|\mathbf{x}_p|^3}\mathbf{x_p}\ . \tag{5.8}$$

The first and second terms represent the gravitational forces from the star and planet, respectively. The final term accounts for the fact that the coordinate system is centered on the star which is a non-inertial frame due to the presence of the companion planet. The total mass of the disc is small compared to the masses of the star and planet, and hence we neglect the contribution to the potential from the disc matter.

5.2.2 The numerical method

The numerical solver is based on Godunov's method. Each fluid variable is discretized across the numerical grid and the equations of hydrodynamics are stepped forward in time by computing the fluxes between the grid cells at every time step. In order to compute the fluxes in between the cells, we utilize an HLLC-type Riemann solver similar to that first proposed by Toro et al. [1994] except that the entropy equation is solved in place of the energy equation [see details in Koldoba et al., August 2015].

Reference units. The reference mass unit of the simulations is set to the mass of the star $M_0 = M_*$; the value of M_* can be chosen arbitrarily to scale the simulations to different mass regimes. The reference length unit is taken to be $r_0 = r_{\rm cav}/1.5$ where $r_{\rm cav}$ is the radius of the disc-cavity boundary. The velocity unit is given by $v_0 = \sqrt{GM_*/r_0}$, corresponding to the Keplerian orbital velocity at $r = r_0$. The unit of time is $P_0 = 2\pi r_0/v_0$ corresponding to the Keplerian orbital period at $r = r_0$. The mass of the planet is given by $M_p = \kappa_p M_*$; in this chapter, we study the migration of super-Earths and hence we take $\kappa_p = 4.5 \times 10^{-5}$ which gives $M_p = 15.0 {\rm M}_\oplus$ when $M_* = {\rm M}_\odot$. The mass of the disc is $M_{d0} = \kappa_d M_*$ with $\kappa_d = 1$ in our simulations. From M_{d0} and r_0, we calculate the unit of density to be $\rho_0 = M_{d0}/r_0^3$ and the unit of surface density to be $\Sigma_0 = M_{d0}/r_0^2$. The reference pressure $p_0 = \rho_0 v_0^2$ and the reference temperature is $T_0 = p_0/(\mathcal{R}\rho_0)$ where $\mathcal{R}$ is the specific gas constant.

For a disc in orbit around a 1 ${\rm M}_\odot$ star with a low-density gap extending out to 1 au, the reference mass is $M_0 = 1 {\rm M}_\odot$, the reference length is $r_0 = 0.66$ au, the reference velocity is 36.5 km s^{-1}, the reference period is $P_0 = 199$ d, and the reference surface density is $\Sigma_0 = 2 \times 10^7$ g cm^{-2}. To determine the physical units, these reference units must then be scaled by the dimensionless values in the simulations. For each dimensionless quantity $\tilde{Q}$, we recover the physical value Q by multiplying by the corresponding reference unit, Q_0: $Q = \tilde{Q} Q_0$. For example, in the simulations, a typical value of the dimensionless surface density is $\tilde{\Sigma} = 4 \times 10^{-4}$, thus the physical disc surface density is $\Sigma = \tilde{\Sigma}\Sigma_0 = 8 \times 10^3$ g cm^{-2}. Similarly, the characteristic mass of the disc in the simulations is $M_d = 1.26 \times 10^{-3} M_{d0} = 1.31 M_J$. Note that this surface density is roughly $10 - 10^3$ times larger than that of a realistic disc, and thus the calculated migration timescales must be scaled accordingly. In this chapter, all of the values are given in terms of the dimensionless units, except where explicitly assigned physical units.

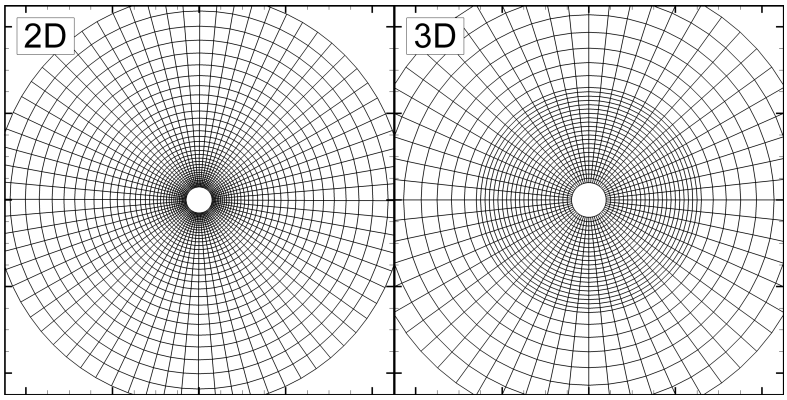

Figure 5.1: **Equatorial $r\phi$ slices of the grid in the 2D and 3D models.** The dimensions of the grid have been reduced by a factor of 8 to show the structure of the mesh.

The grid. We investigate planet migration at the disc-cavity boundary in both 3D $\boldsymbol{r} = (r, \phi, z)$ cylindrical coordinates and 2D $\boldsymbol{r} = (r, \phi)$ polar coordinates. The results of the 3D simulations are presented in §5.3 and we compare the results of the 3D simulations with 2D the models in §5.4.1.

The 2D polar grid is centered on the star and the cells are constructed such that the sides of each cell are approximately equal in length in the r and ϕ directions. The grid has total dimension $(N_r, N_\phi) = (256, 576)$ and spans $r = 0.3 - 4.8$ in the radial direction. Like the 2D grid, the 3D grid is centered on the star; however, the 3D models include radial mesh compression in the region close to the star in order to more finely resolve the dynamics in the inner disc. The inner compressed region spans $r = 0.4 - 2.6$ and has dimensions $N_r = 176$, with constant spacing in the radial direction. Outside of this region, the grid is spaced geometrically as in 2D. The grid is also evenly spaced in the z direction. The total dimension of the grid used in the 3D simulations is $(N_r, N_\phi, N_z) = (232, 480, 80)$ and spans r = 0.4 to 5.2 in the radial direction and z= -0.5 to +0.5 in the vertical direction. Figure 5.1 shows equatorial slices of the grids in 2D and 3D, rarefied by a factor of 8 for clarity.

The disc in 3D. The disc in the 3D models is locally isothermal, non self-gravitating, and initially axisymmetric. In the midplane of the disc, the initial radial density and pressure distributions are given by

$$\rho(r, z = 0) = \begin{cases} \rho_{\rm cav} \left(\frac{r}{r_{\rm cav}}\right)^{-n_{\rm 3D}} & \text{if } r < r_{\rm cav} \\ \rho_{\rm disc} \left(\frac{r}{r_{\rm cav}}\right)^{-n_{\rm 3D}} & \text{if } r \geq r_{\rm cav} \end{cases} \quad , \tag{5.9}$$

and

$$P(r, z = 0) = P_{\rm disc} \left(\frac{r}{r_{\rm cav}}\right)^{-l} \quad ,$$

where $n_{\rm 3D}$ and l are parameters which specify the radial profile of the disc density and pressure. The parameters $\rho_{\rm cav}$, $\rho_{\rm disc}$, and $P_{\rm disc}$ set the cavity density, disc density and pressure at $r = r_{\rm cav}$. The values in the simulations are taken to be $\rho_{\rm cav} = 4 \times 10^{-5}$, $\rho_{\rm disc} = 4{\times}10^{-3}$, and $P_{\rm disc} = 2.6{\times}10^{-6}$, corresponding to a disc aspect ratio of $H/r = 0.03$, where H is the disc half-height. The dimensionless temperature is related to the density and pressure by the ideal gas law $T(r, 0) = P(r, 0)/\rho(r, 0)$.

The disc is initialized in hydrostatic equilibrium and the full expression for the disc volume density is

$$\rho(r, z) = \rho(r, 0) \exp\left(\frac{\Phi_*(r, 0) - \Phi(r, z)}{T(r, 0)}\right)$$

where $\Phi_*(r, z) = -GM_*/(r^2 + z^2)^{1/2}$ is the gravitational potential of the star. The expression for the pressure is analogous. The azimuthal velocity v_ϕ is set by the balance of gravity and the pressure gradient in the radial direction

$$v_\phi(r, z) = \sqrt{r\left(\frac{\partial \Phi}{\partial r} + \frac{1}{\rho}\frac{\partial P}{\partial r}\right)} \tag{5.10}$$

The planet is initialized on a fixed circular orbit; the disc is allowed to relax from $t =$ 0 to 10 before the planet is released and permitted to migrate. As shown in Figure 5.2, the disc's surface density profile does not evolve significantly after this initial relaxation timescale, except under the gravitational influence of the planet.

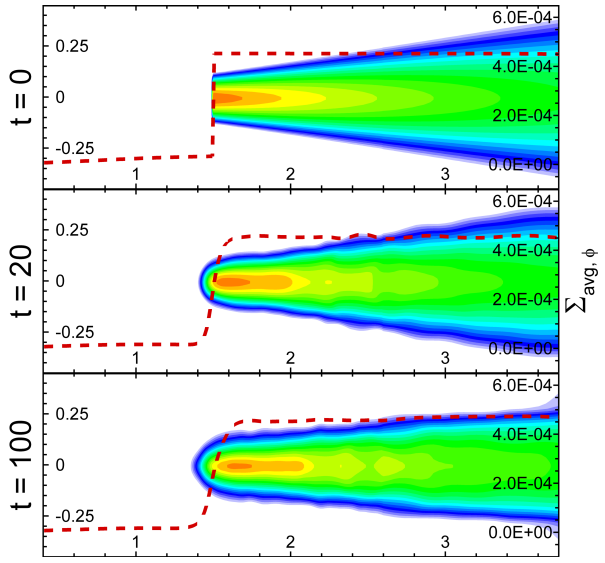

Figure 5.2: **An rz cut through the disc showing the time evolution of the disc density profile in the 3D models.** The contours show the volume density while the dashed line superimposed on top shows the azimuthally averaged surface density profile $\Sigma_{\mathrm{avg},\phi}$. The planet is fixed in place until $t = 10$ to allow for the disc to relax. The middle and bottom panels show that between $t = 20$ and 100, the surface density profile does not evolve substantially in the absence of a perturber.

The disc in 2D. In the 2D simulations, the surface density, Σ, is calculated instead of the volumetric density ρ. The expression for the initial surface density distribution is

$$\Sigma_{\mathrm{2D}}(r) = \left(\Sigma_{\mathrm{cav}} + \frac{\Sigma_{\mathrm{disc}}}{1 + e^{(r_{\mathrm{cav}} - r)/\Delta r}}\right)\left(\frac{r}{r_{\mathrm{cav}}}\right)^{-n_{\mathrm{2D}}} \quad . \tag{5.11}$$

The initial parentheses includes the cavity surface density plus the disc surface density times a logistic function centered at r_{cav} with width Δr and offset Σ_{cav}; the term in the second parentheses is the radial surface density profile in the disc. This functional form is similar (but not identical) to the expression for Σ adopted by Hasegawa and Pudritz [2011]. Σ_{2D} is plotted in the top panel of Figure 5.3 for a range of values of n_{2D} and fixed $\Delta r = 0.01$. This functional form for the surface density is advantageous because the density transition between the cavity and disc is smooth initially. In addition, the inclusion of the parameter Δr permits tuning of the initial width and the slope of the

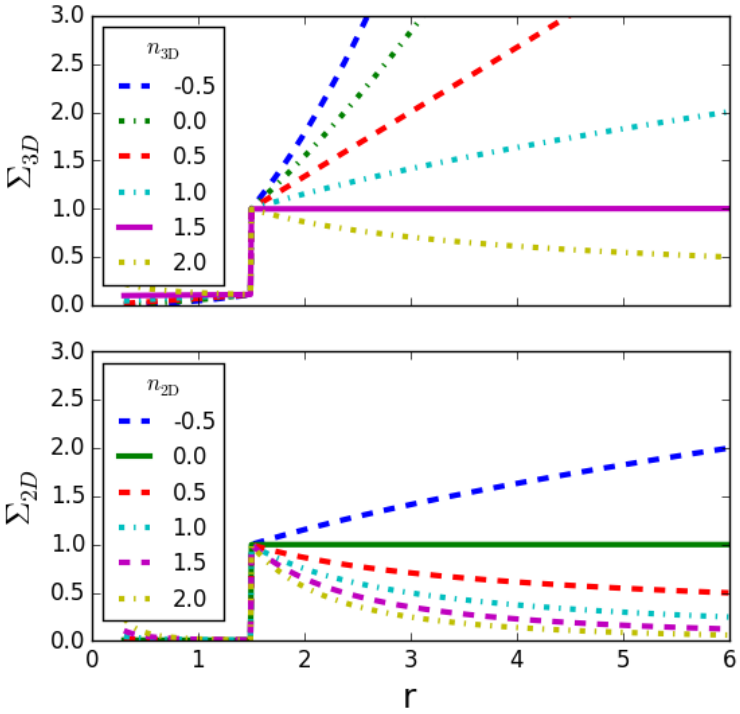

Figure 5.3: **Comparison of the surface density profiles in 2D and 3D for different values of n.** In 2D, n_{2D} directly sets the surface density slope. However, in 3D n_{3D} sets the midplane volume density and Σ_{3D} is computed by integrating the volume density over the height of the disc.

density transition at the cavity boundary. Since the density profile in 2D is initially smooth, the planet in the 2D models is permitted to migrate starting at $t = 0$.

The surface and volumetric densities in 2D and 3D (Σ_{2D} and ρ) can be compared by integrating the 3D volume density over the disc height $2H$ to get $\Sigma_{3D}(r)$

$$\Sigma_{3D}(r) = \int_{-H}^{H} \rho(r, z) dz \quad .$$

In general, the 2D and 3D surface densities have different profiles even when $n_{2D} = n_{3D}$ because the latter is calculated from the volume density. In 2D, $n_{2D} = 0$ results in a flat surface density distribution. However, in 3D, a slope of $n_{3D} = 1.5$ in the equatorial volume density results in a flat surface density profile when integrated over the disc

height. As such, we adopt $n_{3D} = 1.5$ and $n_{2D} = 0$ for all of the simulations to allow for direct comparison of the results in 2D and 3D.

5.3 Results

We consider Type I migration in three separate regions of a three dimensional disc: inside the low-density cavity, at the sharp density transition at the disc-cavity boundary, and inside the dense disc. These three regions are illustrated in the top row of Figure 5.4 which shows surface density waves excited by planets at $r_p = 1.0$, 1.5 and 2.0. The surface density is computed by integrating the volume density over the height of the disc $\int_{-H}^{H} \rho dz$. The second row of panels shows the surface density perturbation

$$\Sigma_{\rm perturb} = \Sigma - \Sigma_{{\rm avg},\phi} = \Sigma - \frac{1}{2\pi}\int_0^{2\pi} \Sigma(r,\phi)\, d\phi \ ,$$

which traces over- and underdensities due to the passage of non-axisymmetric waves in the disc. Here $\Sigma_{{\rm avg},\phi}$ is the azimuthally averaged surface density.

The torque per unit volume (torque density) from the disc on the planet is

$$\gamma_z = \rho(\mathbf{x})\frac{\partial \Phi_p}{\partial \phi} = \frac{GM_p\rho(\mathbf{x})}{(|\mathbf{x}-\mathbf{x_p}|^2+\epsilon^2)^{3/2}} r r_p \sin(\phi - \phi_p) \ ,$$

where Φ_p is the gravitational potential of the planet (the second term in Equation 5.7). The bottom row of Figure 5.4 shows the absolute value of the vertically integrated torque density $|\int \gamma_z dz|$. The degree of asymmetry between the torques sets the direction of the planet's overall migration. This net torque can be measured by integrating the torque density over the simulation region

$$\Gamma_z = \int_{\mathcal{V}} \gamma_z dV = GM_p \int_{\mathcal{V}} \rho(\mathbf{x}) \frac{r r_p \sin(\phi-\phi_p)}{(|\mathbf{x}-\mathbf{x_p}|^2+\epsilon^2)^{3/2}} dV \ . \tag{5.12}$$

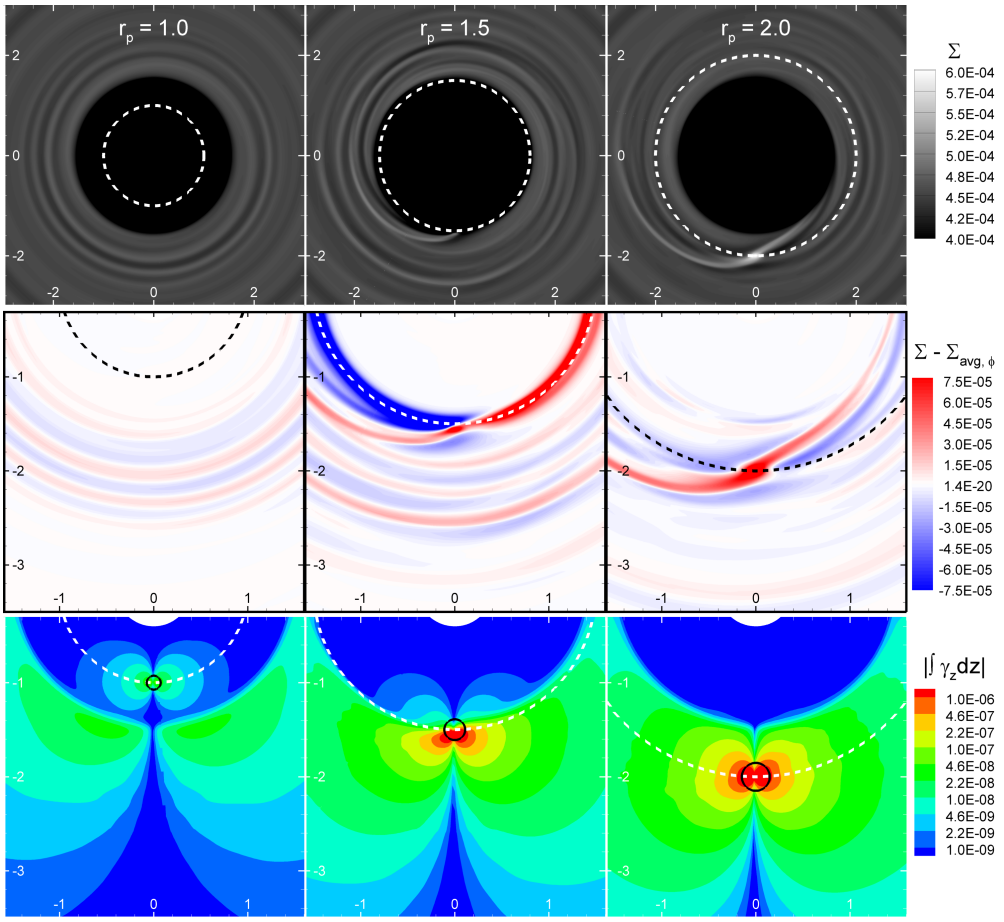

Figure 5.4: **The three main cases of migration in the 3D disc:** (1) in the cavity, $r_p = 1.0$; (2) at the disc-cavity boundary, $r_p = 1.5$; and (3) in the disc, $r_p = 2.0$. *Top row:* the height integrated surface density Σ in the 3D simulations. The white dashed line shows the planet's orbital radius. The red and blue dashed lines show the lowest order inner and outer Lindblad resonances, respectively. *Middle row:* the surface density minus the azimuthally averaged surface density $\Sigma_{\rm pertb} = \Sigma - \Sigma_{{\rm avg},\phi}$ highlighting over- and underdensities in the disc. *Bottom row:* the absolute value of the torque per unit area acting on the planet. This traces the magnitude of the z-torque from each region of the disc.

Another useful quantity is the torque per unit disc mass which is defined similarly

$$\frac{d\Gamma_z}{dM} = \frac{1}{2\pi\Sigma_{{\rm avg},\phi}} \int_{-\infty}^{\infty} \int_{0}^{2\pi} \gamma_z d\phi dz \,, \tag{5.13}$$

[D'Angelo and Lubow, 2008]. Since the aim of this chapter is to study migration, we consider only the z component of the torque which tracks the forces in the disc plane.

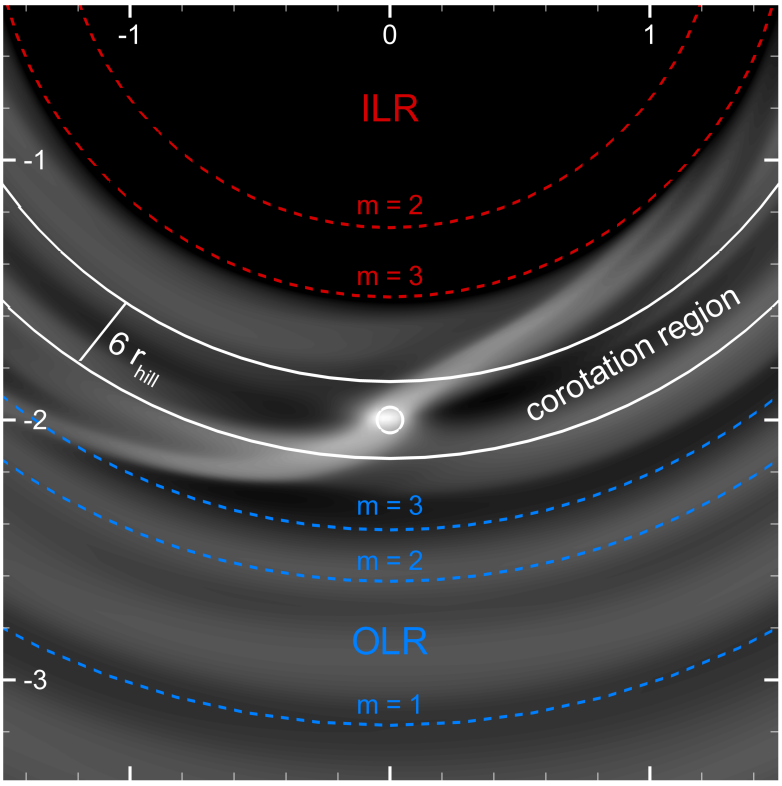

Figure 5.5: **A schematic diagram of the various resonance locations.** The plot shows the corotation region (plotted here as $r_p \pm 3r_{\rm Hill}$) and the location of the $m = 1 - 3$ Lindblad resonances.

Figure 5.5 shows a schematic illustration of the various resonance locations in the disc. The corotation region is plotted schematically as an annulus that extends in between $r_p - 3r_{\rm Hill}$ and $r_p + 3r_{\rm Hill}$. The lowest-order inner and outer Lindblad resonances are located at $0.63r_p$ and $1.59r_p$ respectively (see Equation 5.1), meaning that the lowest order Lindblad resonances lie well outside of the corotation annulus. In the following sections, we analyze the results of our global 3D simulations of planet migration. First, in §5.3.1 we consider the migration of the planets in the cavity and disc ($r_p = 1.0$ and 2.0) and measure the torques acting on the planets as well as their individual migration timescales. Then in §5.3.2 we study the case of a planet which has an initial orbit coinciding with the disc-cavity boundary ($r_p = 1.5$).

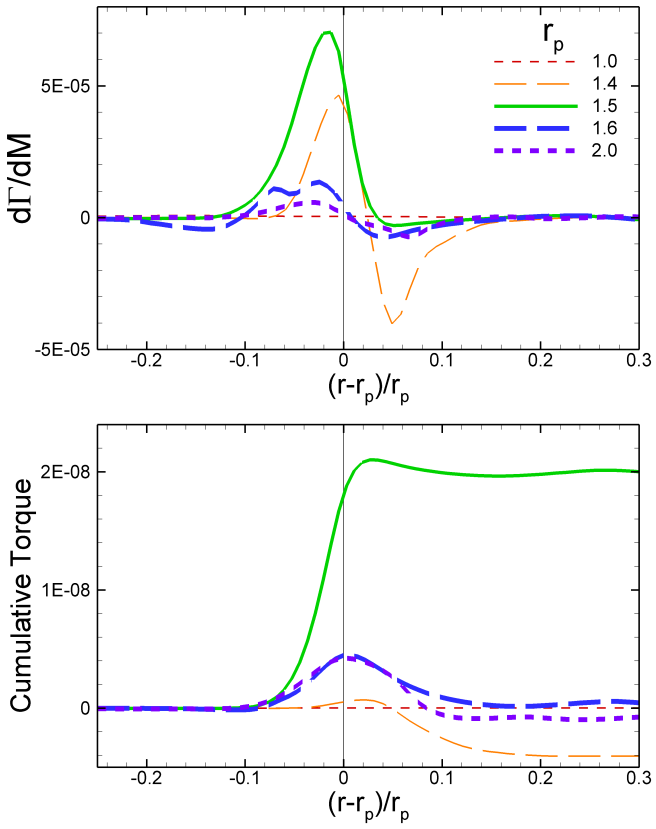

Figure 5.6: **Torque profiles.** *Top panel:* torque per unit disc mass for several different planets at different distances from the star, r_p, at $t = 20$. *Bottom panel:* cumulative torque as a function of normalized radius.

5.3.1 Migration in the disc and cavity

The top panel of Figure 5.6 shows the torque per unit mass (Equation 5.13) as a function of normalized radius while the bottom panel shows the cumulative torque (i.e. the integrated torque density out to the given radius). For the planet embedded in the disc (at $r_p = 2.0$, thick purple dashed line), both the inner and outer Lindblad resonances contribute to the torque on the planet. The lowest order ($m = 2$ and 3) ILRs of the planet lie inside the low-density cavity, but the higher order resonances sit in the disc and contribute a positive torque on the planet. However, the torque from the OLR is larger in magnitude causing the cumulative torque to be negative overall (e.g., bottom panel of

Figure 5.6). This drives inward migration of the planet as shown in the top panel of Figure 5.7. The migration rate for a 15 $M_\oplus$ planet in this region is $\dot{a} = 3.9 \times 10^{-4} v_0$, corresponding to a migration timescale of $t_{\rm mig} = \dot{a}/a = 5200 P_0$ or roughly 2.8×10^3 yr. The density waves generated by the planet are clearly visible in the rightmost panels of Figure 5.4.

For the planet orbiting inside the low-density cavity (at $r_p = 1.0$, thin red dashed line), both the ILR and corotation torques are weak as there is only low-density matter in this region. However, the planet's $m = 1$ OLR sits just outside the inner edge of the disc. For this reason, the planet generates weak density waves at the inner edge of the disc (apparent in the left column of Figure 5.4). The planet loses angular momentum and slowly migrates inward (the migration timescale is discussed in §5.3.1). However, as evidenced in Figure 5.6, the magnitude of this torque is much smaller than the torques on the planets in the disc and at the disc-cavity boundary.

Migration Timescale in the Cavity

Figure 5.7 shows the migration tracks and measured migration rates for planets starting at different distances throughout the cavity and disc. The migration rates are determined by measuring the slope between the start and midpoints of the migration tracks. In this section, we consider just the migration rates of the planets inside the cavity ($r_p < 1.5$). As planets in the cavity migrate inward, the migration rates decline because the planets' higher order OLRs move from the dense disc into the low-density cavity. Once a planet migrates past $r_p \leq 0.945$, the lowest-order OLR of the planet falls entirely inside the gap and the migration rates flatten out at $r_p = 0.8$ with a migration rate of $\dot{a} = 8.6 \times 10^{-7} v_0$ corresponding to a migration timescale of $9.3 \times 10^5 P_0$, or about 0.51 Myr.

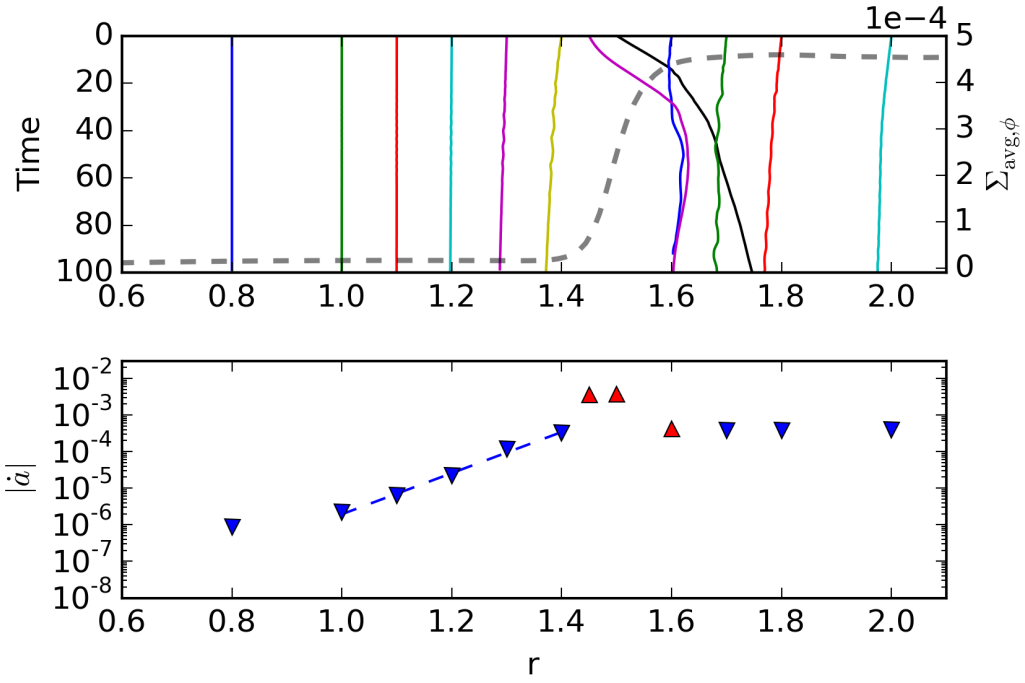

Figure 5.7: **Migration in the 3D model.** *Top panel:* Planet migration tracks in the disc (solid lines) for planets with initial orbital radii ranging from r_p = 0.8–2.0. The disc's surface density profile at t = 20 is shown as a dashed line for reference. *Bottom panel:* absolute value of the migration rates of the planets in 3D code calculated by measuring the overall migration between t = 10 (when the planet is first allowed to migrate) and t = 60. The downward triangles indicate inward migration while the upward pointing triangles indicate outward migration.

This timescale can be compared to the time it takes for the planet to migrate from the inner edge of the disc to the point at which the planet's OLR falls inside the gap (i.e. from $r \approx 1.5$ to 0.945). In this situation, the migration rate varies in time because it depends on the strength of the Lindblad torque which is in turn dependent on the distance of the planet from the disc-cavity boundary. The migration timescale is estimated by fitting an exponential function to the migration rates (shown as a dashed line in Figure

5.7) and integrating over the resulting function

$$t_{\rm mig} = \int_{r_{\rm gap}}^{r_{\rm in}} \frac{dr}{\dot{r}} \quad .$$

This gives a timescale of $8.1 \times 10^4 P_0$, corresponding to 4.4×10^4 years–an order of magnitude smaller than the 5.1×10^5 yr timescale for the planet to migrate from $r_p = 0.8$ to the star.

5.3.2 Migration at the disc-cavity boundary

At the boundary between the cavity and disc, the density gradient can modify the horseshoe orbits in the corotation regions of planets, resulting in a strong corotation torque on planets in this region. The middle column of Figure 5.4 shows a planet at $r_p = 1.5$ with an initial orbit coinciding with the disc-cavity boundary. The top and middle panels illustrate the clear asymmetry between the leading and trailing surface densities; this asymmetry in the surface density translates into a correspondingly asymmetric torque which is apparent in the bottom panel of the figure. This asymmetry is also apparent in Figure 5.6 which shows the torque per unit mass as a function of radius. The top panel shows that for the planet at $r_p = 1.5$, there is a strong positive torque from the region interior to the planet, resulting a large positive cumulative torque (bottom panel). This large, positive torque causes the planet to migrate outward rapidly in contrast to the planets at $r_p = 1.0$ and 2.0 which consistently migrate inward due to their tidal interactions with the disc.

The migration tracks of planets which start near the disc-cavity boundary are shown in Figure 5.7. The range of radii in which the corotation torque is significant is quite narrow—only planets in the range $r \approx 1.45 - 1.6$ migrate outward due to their interaction with positive density gradient at the disc-cavity boundary. The planets starting just in-

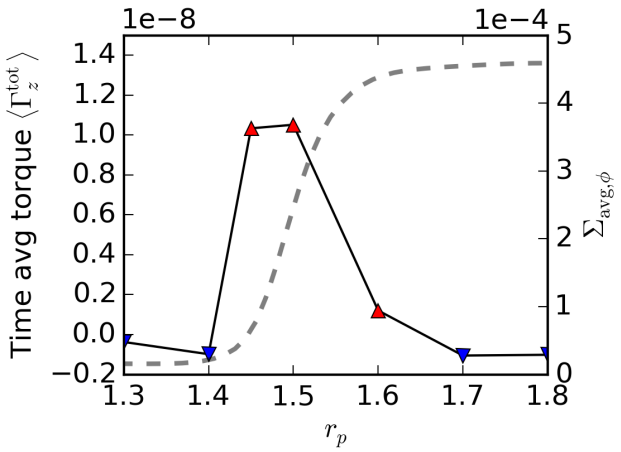

Figure 5.8: **The time averaged total torque.** The plot shows $\left\langle \Gamma_z^{\rm tot} \right\rangle$ versus planet radius r_p for the planets with initial orbits near the disc-cavity boundary. The torques are computed by time averaging between $t = 10$ (when the planet is first allowed to migrate) and $t = 60$. For reference, the surface density profile at $t = 20$ is plotted as a dashed line.

side and outside of the disc-cavity boundary at $r_p = 1.4$ and 1.7 migrate inward as usual due to the differential Lindblad torque. However, this indicates that there must exist a stable halting region where the positive corotation torque exactly balances the negative differential Lindblad torque: this region is referred to as the *planet trap* by Masset et al. [2006]. To identify this trapping region in our models, the total torque from $t = 10 - 60$ is time averaged and plotted versus r_p in Figure 5.8. The azimuthally-averaged surface density, $\Sigma_{{\rm avg},\phi}$, is also plotted for reference. Evidently, the planet trap lies at $r_{\rm trap} \approx 1.65$ in our 3D model. A planet in this region is stably trapped because the torque interior to $r_{\rm trap}$ is positive and drives outward migration toward the trap; similarly, the torque exterior to $r_{\rm trap}$ is negative and also drives inward migration towards the trap. As suggested by Masset et al. [2006] and Morbidelli et al. [2008], this implies that planets undergoing Type I migration will tend to be trapped when encountering a positive density gradient in the disc (such as the edge of a cavity or gap).

5.4 Discussion

5.4.1 Comparison with 2D Models

Here we compare the results of planet migration in the 3D cylindrical models to the results of the 2D models in polar coordinates. In 2D, the hydrodynamic equations for the height-integrated analogs of each fluid quantity (for example, the surface density Σ instead of the volume density ρ) are solved. Like the disc in the 3D model, the 2D disc has a central low density cavity with radius $r = 1.5$. To facilitate comparisons, the initial surface density in the 2D simulations is tuned to approximately match the slope and magnitude of the surface density profile in the 3D simulations: $n_{2D} = 0$, $\Sigma_{\rm disc} = 4 \times 10^{-4}$, and $\Delta r = 0.05$. A complete description of the 2D model can be found in §5.2.

As in the 3D models, planet migration rates are measured for planets orbiting at distances ranging from $r_p = 0.7 - 2$. The top panel of Figure 5.9 shows the migration tracks of these planets through the disc; the dashed line shows the initial surface density profile of the disc for reference. The migration of the planets in 2D is qualitatively the same as in 3D: planets starting out in the disc or inside the cavity experience inward migration due to the differential Lindblad torque on the planet; near the disc-cavity boundary at $r = 1.5$, the corotation torque dominates and results in a net positive torque which drives the planets to migrate outward. The planets near the boundary tend to migrate outward until they reach the point where the corotation torque balances the Lindblad torque (around $r_p \approx 1.57$) and they become trapped.

The bottom panel of Figure 5.9 shows the measured migration rates determined from the slope of the migration tracks between $t = 0$ and 50. The downward facing arrows indicate inward migration toward the star while the upward facing arrows indicate outward

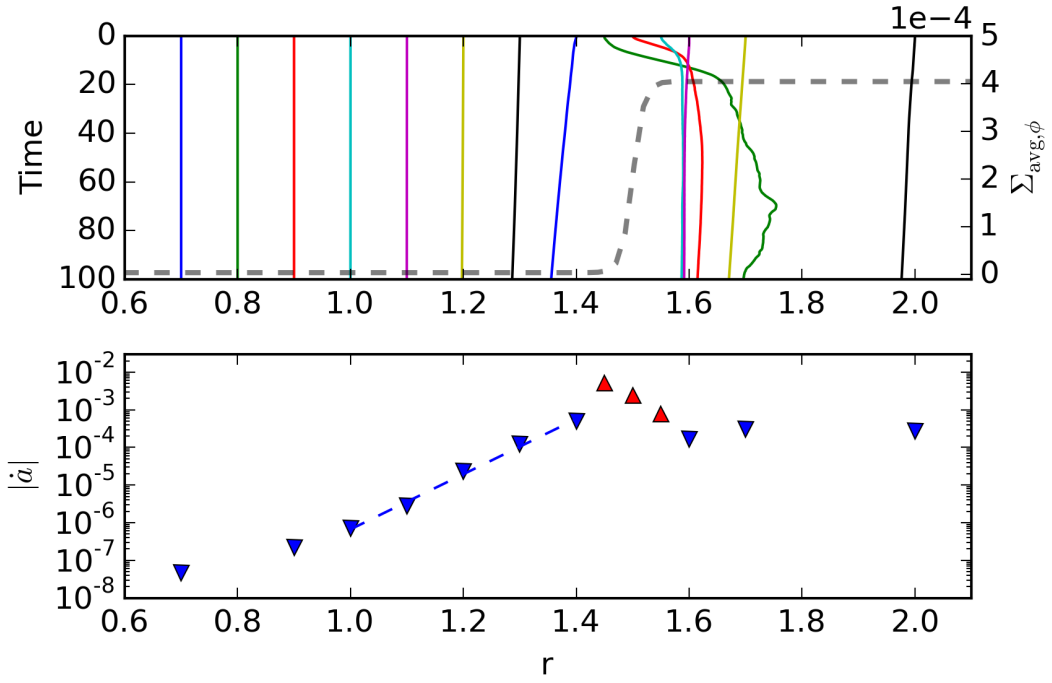

Figure 5.9: **Migration in the 2D model.** *Top panel:* Planet migration tracks in the disc (solid lines) for planets with initial orbital radii ranging from r_p = 0.7–2.0. The disc's surface density profile at t=0 is shown as a dashed line for reference. *Bottom panel:* absolute value of the migration rates of the planets in 2D code calculated between t = 0–50. The downward triangles indicate inward migration while the upward pointing triangles indicate outward migration.

migration. As is evident from the top panel, the migration of the planets which start near r_p = 1.5 (i.e., the disc-cavity boundary) proceeds rapidly, with timescales ranging from $t = 10 - 20$. This means that the initial migration rates of the planets near the boundary are underestimated by a factor of ~2–5.

One key difference between the 2D and 3D models is in the magnitude of the density gradient at the disc-cavity boundary. In 2D, the gradient is more positive, and as such, the initial migration in the 2D models proceeds more quickly. Additionally, since the density gradient is larger, the disc-cavity boundary is narrower, resulting in a narrower

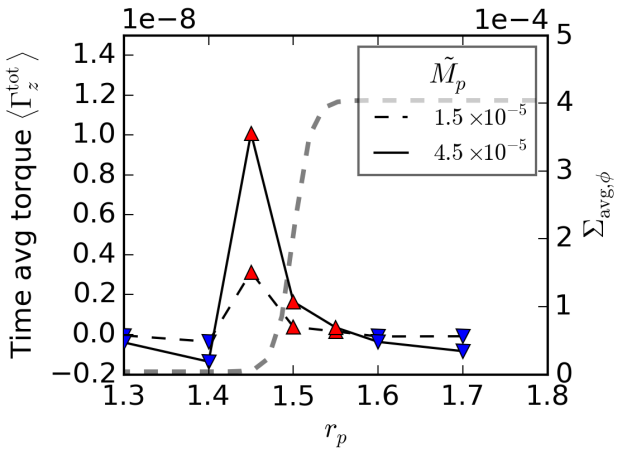

Figure 5.10: **Time averaged torques for the 2D case.** The same plot as Figure 5.8 for two different mass planets in the 2D models.

range of radii where the corotation torque is important and outward migration is possible. This is evident in Figure 5.10 which shows the time averaged torques as a function of radius in the 2D models (see Figure 5.8 for $\left\langle \Gamma_z^{\rm tot} \right\rangle$ in the 3D models). The narrower edge also shifts location of the planet trap to $r = 1.55$, slightly closer to the disc-cavity boundary compared to the 3D models. However, in all other respects, the torques in the 2D and 3D models are qualitatively the same.

5.4.2 Dependence on the disc aspect ratio

A key difference between the 2D and 3D models is that the disc height can vary in the 3D models. In order to investigate the effect of the disc height on the planet migration, we fix the disc's surface density profile while varying the disc aspect ratio, H/r. The resulting density profiles are shown in Figure 5.11 for $H/r = 0.03$, 0.05, and 0.1. The midplane densities are tuned such that all three discs have identical surface densities which are constant with radius: $\Sigma(r) = 4 \times 10^{-4}$ for $r > r_{\rm cav}$.

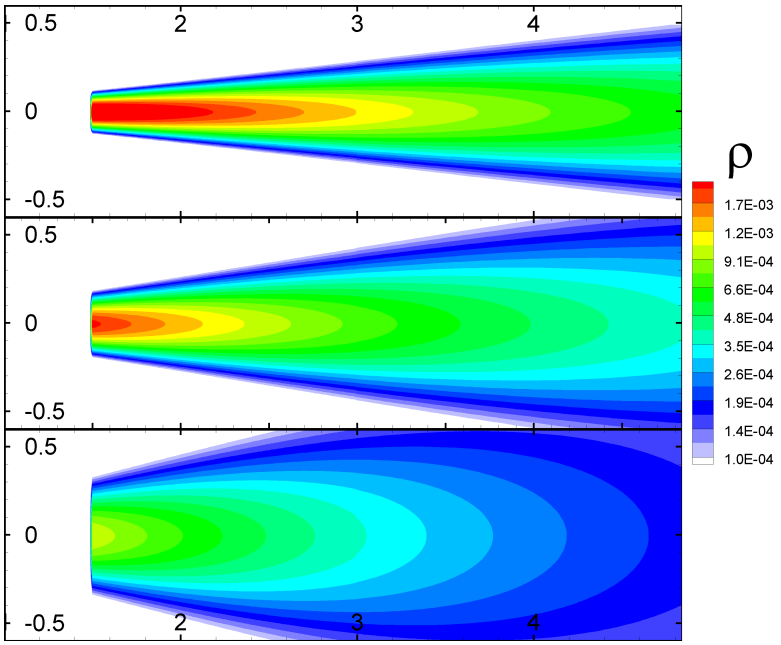

Figure 5.11: **Different aspect ratio discs.** From top to bottom: three discs with differing aspect ratios of $H/r = 0.03$, 0.05, and 0.10 but *identical surface density profiles*.

We measure the torques on two planets at $r_p = 1.5$ (the disc-cavity boundary) and $r_p = 2.0$ (in the disc). Figure 5.12 shows the torque per unit mass (top row) and cumulative torque (bottom row) on the two planets as a function of normalized radius, time averaged from $t = 10 - 80$. Evidently, the net torque on the planet is diminished by increasing the disc's aspect ratio for both the planet at $r_p = 1.5$ where the corotation torque is important and at $r_p = 2.0$ where the differential Lindblad torque dominates. The bottom panels of Figure 5.12 show that the tidal torque's dependence on the aspect ratio is nonlinear, with much stronger torques in thinner discs. This is due to the fact that as the disc thickness increases, less mass is concentrated near the disc midplane. For the corotation resonance, this means that less matter participates in the horseshoe orbit and the magnitude of the corotation torque is smaller. Similarly, for the Lindblad torques, the amplitude of the surface density perturbations raised by the planet is smaller and the torque again weakens.

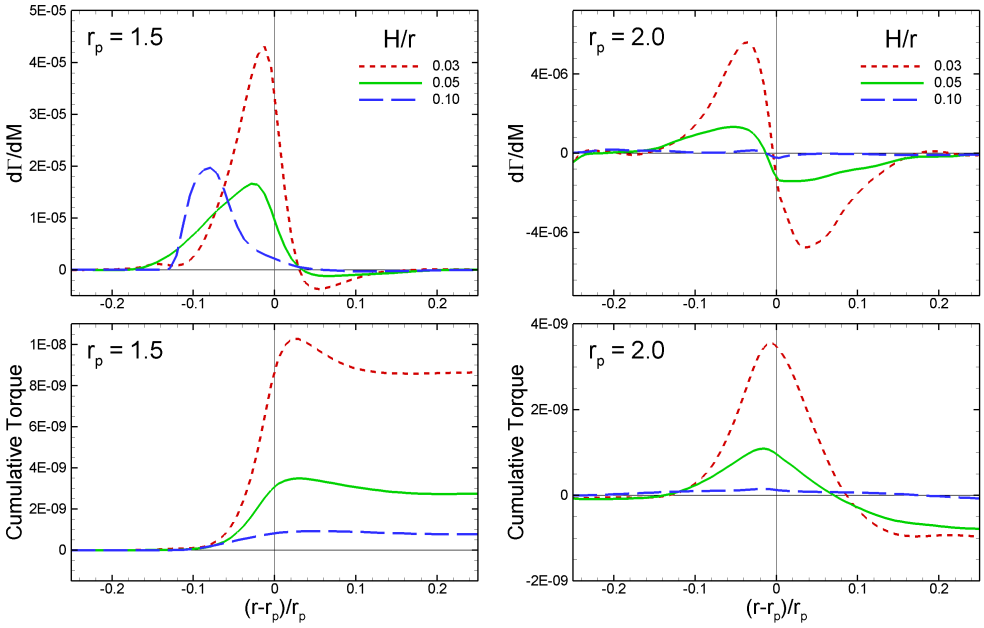

Figure 5.12: **Torque profiles for differing disc aspect ratios.** *Top row:* the torque per unit mass as a function of normalized radius for planets starting at $r_p = 1.5$ and 2.0 in three discs with differing aspect ratios, but identical surface density profiles. *Bottom row:* same as the top row, but showing the cumulative torque as a function of normalized radius. The profiles are time averaged over $t = 70$.

The implication of these results is that for reasonable values of H/r, varying the disc height does not change the direction of the migration; however, it may strongly modify the migration timescale of the planet. This effect is especially significant for the planets interacting with the disc-cavity boundary where the corotation torque is important. However, since the migration direction is unaffected, the planet trapping mechanism is robust across the varying disc aspect ratios.

5.4.3 Applications

A planet trap at the dust sublimation radius

Observations of protoplanetary discs show an infrared excess at 3 μm which can be attributed to an inner disc edge at a distance coinciding with the dust-sublimation radius of the system [Dullemond et al., 2001]. Exterior to this radius, the disc is cold and dusty and the MRI-powered accretion (which is sensitive to the ionization fraction in the disc) proceeds slowly.

However, interior to the dust sublimation radius, the gas disc is optically thin and the ionization fraction is high. As a result, the viscosity provided by the MRI turbulence is large and accretion interior to the dust sublimation radius proceeds efficiently. The result is an evacuated low-density inner cavity surrounded by a cold, higher density disc. Migrating planets which encounter this inner cavity may become trapped at the density transition and migrate in or out if the dust sublimation radius changes as the young star moves along the Hayashi track towards the main sequence.

Infrared observations of protoplanetary discs show that these inner cavities can range from ~0.1 to 4 au in size depending on the luminosity of the central star [Muzerolle et al., 2003, Akeson et al., 2005, Monnier et al., 2005]. The outer edge of this cavity may act as a trap for inwardly migrating planetesimals, allowing for the gradual buildup of planetary embryos in this region [Morbidelli et al., 2008]. Kuchner and Lecar [2002] investigated a similar scenario of a migrating planet which halts when its 2:1 Lindblad resonance falls interior of the dust sublimation radius. This scenario is still possible for higher mass planets migrating in the Type II regime: as shown in §5.3.1, the migration rate of a planet in the cavity decreases substantially as the distance from the cavity boundary increases. However, as demonstrated in §5.3.2, lower mass planets are likely

to become trapped at the dust sublimation radius before they can migrate into the cavity.

As discussed by Masset et al. [2006], low-mass migrating planets may also become trapped at the inner edge of a dead zone where the ionizing radiation does not penetrate far enough into the disc to sustain MRI-driven accretion [Gammie, 1996]. The surface density in the dead zone is expected to be substantially higher than the density in inner regions where the MRI-driven turbulence is ongoing. As such, the inner edge of the dead zone may serve as trap for migrating planets. Like the dust sublimation radius, the inner dead zone radius may change in time causing planets trapped at the inner edge to move in or out correspondingly [Kretke and Lin, 2012].

A planet trap at the disc-magnetosphere boundary

The young stars at the center of protoplanetary systems tend to be highly magnetized due to the onset of convection in their protostellar cores. The stellar field truncates the inner disc, creating a low-density *magnetospheric gap* in the region immediately adjacent to the star [Königl, 1991]. This density transition between between the low-density magnetosphere and the higher-density accretion disc has a sharp positive density gradient due to the truncation by the magnetic field [e.g., Romanova et al., 2003, Romanova and Lovelace, 2006]. This sharp interface is known as the *disc-magnetosphere* boundary and is often defined as the location where the thermal and matter ram pressure in the disc balance the magnetic pressure of the stellar field. A migrating planet which encounters this boundary becomes trapped due to this sharp density gradient at the disc-magnetosphere interface. If the disc accretion rate declines and the magnetospheric radius increases, the trapped planet may move outward with the inner edge of the disc due to the action of the corotation torque. For a typical T Tauri star, the magnetospheric boundary is located at $\sim 0.05 - 0.1$ au and may serve as a final barrier, preventing planets from migrating all

the way into their host stars.

The accretion rates in the disc around young stars may span several orders of magnitude from $\dot{M} \sim 10^{-7} - 10^{-11} \mathrm{M}_{\odot}/\mathrm{yr}$, meaning that the size of the magnetospheric cavity can also differ substantially between young stellar systems [Hartmann, 2000]. This impies that planets will become trapped at a variety of distances from the star and may explain why Kepler observations do not show planets bunched up at a particular radius.

5.5 Chapter summary

The main points of this chapter are as follows:

- We have presented global 3D simulations of planets migrating near the edge of a disc cavity.
- For planets migrating far from the cavity boundary, the migration proceeds due to the excitation of density waves at the Lindblad resonances. However, migrating planets which encounter the boundary experience a large positive corotation torque due the the positive surface density gradient at the disc-cavity interface.
- There exists a region in the disc where the magnitude of the corotation torque is equal and opposite to the differential Lindblad torque, resulting in a region where a planet experiences zero net torque from the disc. Interior to this region, the net torque is positive due to the corotation torque and the planet migrates outward; similarly, exterior to this location, differential Lindblad torque is larger in magnitude and the net torque is negative, resulting in inward migration. Hence the zero-torque region is a stable "planet trap" as any perturbations in either direction result in a torque which pushes the planet back toward the trapping region.

- An accretion disc around a young star may have several such planet traps wherever there is a positive surface density gradient in the disc. A positive surface density gradient may appear at the dust-sublimation radius, at the inner edge of dead zones, or at the edge of the magnetospheric cavity. As the disc's accretion rate or the stellar luminosity change in time, the locations of these boundaries may shift. Any planets which are trapped at the density gradients are likely to migrate along with the boundary.

CHAPTER 6

CONCLUSIONS

Outflows are ubiquitous among both young and old stellar systems and are understood to be magnetocentrifugally driven. Outflows require three processes: accretion, which acts as a source of matter, and magnetic fields and rotation which load and accelerate the matter out of the disk. In Chapter 3, we discussed a mechanism for the launching and collimation of outflows from the disk-magnetosphere boundary of accreting magnetized stars. In regimes of high accretion, the magnetosphere of the star can become strongly compressed, resulting in large magnetic pressure which loads the matter onto the rotating field lines. As the matter accelerates outward, it is quickly collimated by the magnetic hoop stress of the field lines extending up from the disc. In the jet, we observe half-opening angles of less than 4° at distances of a few tens of stellar radii away from the star.

The results of these models are most relevant to EXors or FUor class stars which are undergoing eruptive outbursts. These outbursts are attributed to intense bursts of accretion or the sudden infall of circumstellar material and the models presented here may explain some of the strongly collimated outflows associated with these outbursting sources.

In Chapter 4, we discussed another form of outflows, this time launched from the disk-magnetosphere of stars accreting in the propeller regime. We showed that these rapidly rotating stars can centrifugally launch matter from the disk-magnetosphere boundary with efficiencies ranging from 50% to nearly 90% for the parameter space studied. Unlike the well-collimated outflows discussed in Chapter 3, the propeller-driven outflows have wide opening angles of 45° at the base and exhibit weak collimation. Our models show that the accretion onto these rapidly rotating stars proceeds in

an episodic fashion through an accumulation-accretion cycle: the disc matter is blocked by accreting by the centrifugal barrier of the star and gradually accumulates at the disc-magnetosphere boundary. The accumulated matter compresses the magnetosphere inward until the inward gravitational acceleration exceeds the outward centrifugal barrier and the matter accretes as a funnel flow on the star in a burst of accretion. With the reservoir of matter depleted, the magnetosphere rapidly re-expands and truncates the accretion onto the star. This mechanism is similar to the episodic accretion instability first described by Spruit and Taam [1993]. Each burst of accretion is accompanied by a corresponding one-sided burst in the outflow and may serve to explain some of the clumpy outflows observed in accreting stellar systems.

This model is highly relevant to transitional pulsars which are transitioning between accretion and rotation powered regimes. As the accretion rate onto these stars declines, the star is expected to enter the propeller regime of accretion. Suggestions of outflows and episodes of quasi-periodic X-ray flares have been observed in these systems, which hint at the underlying propeller-regime dynamics as shown in the simulations presented here. Future work on these systems must be approached from both observational and theoretical perspectives. Observationally, we require high time-cadence X-ray observations to further understand the dynamics of the inner disk where the accretion processes occur on millisecond timescales. This will allow us to probe the properties of the disk-magnetosphere boundary by matching the observations with our models. Spectral observations will help us determine the emission mechanism in these systems and help constrain physical properties such as the temperature, density and magnetic field strength in these inner regions. Additionally, observations of the outflows in these systems would allow us to estimate the magnetic diffusivity in these inner regions. Long term monitoring of the transitional millisecond pulsars are also needed in order to determine the mechanism behind the sudden shifts between the high and low X-ray states

observed in IGR J18245-2452.

From the theoretical side, further simulations are needed to understand the observational signatures of the accretion-ejection cycle. Namely, we wish to understand why a single system can exhibit both regular, periodic X-ray flaring as well as irregular, quasi-periodic X-ray flares depending on the accretion rate. Three-dimensional simulations of the propeller regime are needed to investigate the role of magnetic instabilities at the disk-magnetosphere boundary as well as the effect of magnetospheric spin-axis misalignment. We also seek to understand the dependence of the accretion-ejection mechanism on various parameters such as accretion rate, stellar rotation, disk or stellar magnetic fields, and the magnetic diffusivity. We also need to investigate the emission mechanisms in these systems which can then be applied in radiative transfer models to model the emission from the disk, accretion column, accretion shock and the star.

In Chapter 5, we shifted our focus to planet-disc dynamics and investigated the interaction of super-Earth class planets with a disk that has a sharp density gradient (such as the edge of the dust sublimation region or the disk-magnetosphere boundary). In a typical power-law protoplanetary disk, the differential Lindblad torque dominates the overall torque on the planet, resulting in preferentially inward migration. However, if there is a sharp positive density gradient in the disk, the magnitude of the corotation torque can be large and positive. Using 3D simulations, we demonstrated that this can create a stable "planet trap" at the location where the positive corotation torque exactly balances the negative differential Lindblad torque, resulting in a region where the net torque is zero. This trapping region is stable: planets interior to this region experience a stronger positive corotation torque which causes outward migration toward the trap; similarly, planets exterior to this region experience a negative torque from the differential Lindblad resonance, and also migrate inward towards the trap. Any perturbations

in either direction result in a torque which pushes the planet back toward the trapping region. A protoplanetary disk around a young star may have several such planet traps at the dust-sublimation radius, the inner edges of dead zones, or the edge of the magnetospheric cavity. Additionally, trapped planets are likely to migrate along with the trapping regions as the disc evolves in time. Future work on the planet trap should investigate the parameter space in which this effect is important. Namely, in what planetary mass regime is this effect significant and how does the surface density of the disk affect the trapping? Additionally, further research should investigate how a multi-planet system can change this picture and what the observational signatures of such a system might be.

APPENDIX A

THE EQUATIONS OF MHD IN CYLINDRICAL COORDINATES

In cylindrical coordinates, the divergence operator takes the form

$$\nabla \cdot \boldsymbol{A} = \frac{1}{r}\partial_r(rA_r) + \frac{1}{r}\partial_r A_\phi + \partial_z A_z \,. \tag{A.1}$$

Using this equation, we can explicitly write out the full MHD equations in cylindrical coordinates by plugging in the state, flux and source terms (Equation 2.6 and Equation 2.10) into the conservation equation (Equation 2.9).

- The continuity equation.

$$\partial_t \rho + \frac{1}{r}\partial_r(r\rho v_r) + \frac{1}{r}\partial_\phi(\rho v_\phi) + \partial_z(\rho v_z) = 0 \tag{A.2}$$

- The entropy conservation equation.

$$\partial_t(\rho s) + \frac{1}{r}\partial_r(r\rho s v_r) + \frac{1}{r}\partial_\phi(\rho s v_\phi) + \partial_z(\rho s v_z) = 0 \tag{A.3}$$

- The momentum conservation equation.

$$\partial_t(\rho v_r) + \partial_r\left(\rho v_r^2 + p_{\rm tot} - \frac{B_r^2}{4\pi}\right) + \frac{1}{r}\partial_\phi\left(\rho v_r v_\phi - \frac{B_r B_\phi}{4\pi}\right) + \partial_z\left(\rho v_r v_z - \frac{B_r B_z}{4\pi}\right) = \frac{1}{r}\left(\rho(v_\phi^2 - v_r^2) - \frac{B_\phi^2 - B_r^2}{4\pi}\right) + \rho g_r \tag{A.4}$$

$$\partial_t(\rho v_\phi) + \frac{1}{r^2}\partial_r r^2\left(\rho v_r v_\phi - \frac{B_r B_\phi}{4\pi}\right) + \frac{1}{r}\partial_\phi\left(\rho v_\phi^2 + p_{\rm tot} - \frac{B_\phi^2}{4\pi}\right) + \partial_z\left(\rho v_\phi v_z - \frac{B_\phi B_z}{4\pi}\right) = 0 \tag{A.5}$$

$$\partial_t(\rho v_z) + \frac{1}{r}\partial_r r\left(\rho v_r v_z - \frac{B_r B_z}{4\pi}\right) + \frac{1}{r}\partial_\phi\left(\rho v_\phi v_z - \frac{B_\phi B_z}{4\pi}\right) + \partial_z\left(\rho v_z^2 + p_{\rm tot} - \frac{B_z^2}{4\pi}\right) = \rho g_z \tag{A.6}$$

where $p_{\rm tot} = p + \frac{B^2}{8\pi}$ is the total pressure and $\mathbf{g} = -\nabla\Phi$ is net external force from the central star and planet.

- The induction equation.

$$\partial_t B_r + \frac{1}{r}\partial_\phi \left(v_\phi B_r - v_r B_\phi\right) + \partial_z \left(v_z B_r - v_r B_z\right) = 0 \tag{A.7}$$

$$\partial_t B_\phi + \partial_r \left(v_r B_\phi - v_\phi B_r\right) + \partial_z \left(v_z B_\phi - v_\phi B_z\right) = 0 \tag{A.8}$$

$$\partial_t B_z + \frac{1}{r}\partial_r r \left(v_r B_z - v_z B_r\right) + \frac{1}{r}\partial_\phi \left(v_\phi B_z - v_z B_\phi\right) = 0 \tag{A.9}$$

These equations are described in full in Skinner and Ostriker [2010] and Koldoba et al. [August 2015].

BIBLIOGRAPHY

V. Agra-Amboage, C. Dougados, S. Cabrit, and J. Reunanen. Sub-arcsecond [Fe ii] spectro-imaging of the DG Tauri jet. Periodic bubbles and a dusty disk wind? A&A, 532:A59, August 2011. doi: 10.1051/0004-6361/201015886.

R. L. Akeson, C. H. Walker, K. Wood, J. A. Eisner, E. Scire, B. Penprase, D. R. Ciardi, G. T. van Belle, B. Whitney, and J. E. Bjorkman. Observations and Modeling of the Inner Disk Region of T Tauri Stars. ApJ, 622:440–450, March 2005. doi: 10.1086/427770.

S. H. P. Alencar, C. M. Johns-Krull, and G. Basri. The Spectral Variability of the Classical T Tauri Star DR Tauri. AJ, 122:3335–3360, December 2001. doi: 10.1086/323914.

S. H. P. Alencar, G. Basri, L. Hartmann, and N. Calvet. The extreme T Tauri star RW Aur: accretion and outflow variability. A&A, 440:595–608, September 2005. doi: 10.1051/0004-6361:20053315.

M. A. Alpar. On Young Neutron Stars as Propellers and Accretors with Conventional Magnetic Fields. ApJ, 554:1245–1254, June 2001. doi: 10.1086/321393.

J. Arons and S. M. Lea. Accretion onto magnetized neutron stars - Structure and interchange instability of a model magnetosphere. ApJ, 207:914–936, August 1976. doi: 10.1086/154562.

F. Bacciotti, R. Mundt, T. P. Ray, J. Eislöffel, J. Solf, and M. Camezind. Hubble Space Telescope STIS Spectroscopy of the Optical Outflow from DG Tauri: Structure and Kinematics on Subarcsecond Scales. ApJ, 537:L49–L52, July 2000. doi: 10.1086/312745.

S. A. Balbus and J. F. Hawley. A powerful local shear instability in weakly magnetized disks. I - Linear analysis. II - Nonlinear evolution. ApJ, 376:214–233, July 1991. doi: 10.1086/170270.

C. Baruteau and F. Masset. Type I Planetary Migration in a Self-Gravitating Disk. ApJ, 678:483–497, May 2008. doi: 10.1086/529487.

C. G. Bassa, A. Patruno, J. W. T. Hessels, E. F. Keane, B. Monard, E. K. Mahony, S. Bogdanov, S. Corbel, P. G. Edwards, A. M. Archibald, G. H. Janssen, B. W. Stappers, and S. Tendulkar. A state change in the low-mass X-ray binary XSS J12270-4859. MNRAS, 441:1825–1830, June 2014. doi: 10.1093/mnras/stu708.

T. L. Beck, A. Riera, A. C. Raga, and B. Reipurth. The Structure of the Inner HH 34 Jet from Optical Integral Field Spectroscopy. AJ, 133:1221–1235, April 2007. doi: 10.1086/511269.

N. Bessolaz, C. Zanni, J. Ferreira, R. Keppens, and J. Bouvier. Accretion funnels onto weakly magnetized young stars. A&A, 478:155–162, January 2008. doi: 10.1051/0004-6361:20078328.

G. S. Bisnovatyi-Kogan and R. V. E. Lovelace. Large-Scale B-Field in Stationary Accretion Disks. ApJ, 667:L167–L169, October 2007. doi: 10.1086/522206.

G. S. Bisnovatyi-Kogan and A. A. Ruzmaikin. The Accretion of Matter by a Collapsing Star in the Presence of a Magnetic Field. Ap&SS, 28:45–59, May 1974. doi: 10.1007/BF00642237.

G. S. Bisnovatyi-Kogan and A. A. Ruzmaikin. The accretion of matter by a collapsing star in the presence of a magnetic field. II - Selfconsistent stationary picture. Ap&SS, 42:401–424, July 1976. doi: 10.1007/BF01225967.

R. D. Blandford and D. G. Payne. Hydromagnetic flows from accretion discs and the production of radio jets. MNRAS, 199:883–903, June 1982.

S. Bogdanov and J. P. Halpern. Identification of the High-energy Gamma-Ray Source 3FGL J1544.6-1125 as a Transitional Millisecond Pulsar Binary in an Accreting State. ApJ, 803:L27, April 2015. doi: 10.1088/2041-8205/803/2/L27.

J. Bouvier, A. Chelli, S. Allain, L. Carrasco, R. Costero, I. Cruz-Gonzalez, C. Dougados, M. Fernández, E. L. Martín, F. Ménard, C. Mennessier, R. Mujica, E. Recillas, L. Salas, G. Schmidt, and R. Wichmann. Magnetospheric accretion onto the T Tauri star AA Tauri. I. Constraints from multisite spectrophotometric monitoring. A&A, 349:619–635, September 1999.

J. Bouvier, K. N. Grankin, S. H. P. Alencar, C. Dougados, M. Fernández, G. Basri, C. Batalha, E. Guenther, M. A. Ibrahimov, T. Y. Magakian, S. Y. Melnikov, P. P. Petrov, M. V. Rud, and M. R. Zapatero Osorio. Eclipses by circumstellar material in the T Tauri star AA Tau. II. Evidence for non-stationary magnetospheric accretion. A&A, 409:169–192, October 2003. doi: 10.1051/0004-6361:20030938.

J. Bouvier, S. H. P. Alencar, T. Boutelier, C. Dougados, Z. Balog, K. Grankin, S. T. Hodgkin, M. A. Ibrahimov, M. Kun, T. Y. Magakian, and C. Pinte. Magnetospheric accretion-ejection processes in the classical T Tauri star AA Tauri. A&A, 463:1017–1028, March 2007. doi: 10.1051/0004-6361:20066021.

M. Brio and C. C. Wu. An upwind differencing scheme for the equations of ideal magnetohydrodynamics. *Journal of Computational Physics*, 75(2):400 – 422, 1988. ISSN 0021-9991. doi: DOI: 10.1016/0021-9991(88)90120-9. URL http://www.sciencedirect.com/science/article/pii/0021999188901209.

S. Brittain, T. W. Rettig, T. Simon, D. S. Balsara, D. Tilley, E. Gibb, and K. H. Hinkle.

Post-Outburst Observations of V1647 Orionis: Detection of a Brief Warm Molecular Outflow. ApJ, 670:L29–L32, November 2007. doi: 10.1086/524035.

P. Bult and M. van der Klis. Discovery of 1-5 Hz Flaring at High Luminosity in SAX J1808.4-3658. ApJ, 789:99, July 2014. doi: 10.1088/0004-637X/789/2/99.

L. Burderi, T. Di Salvo, F. D'Antona, N. R. Robba, and V. Testa. The optical counterpart to SAX J1808.4-3658 in quiescence: Evidence of an active radio pulsar? A&A, 404: L43–L46, June 2003. doi: 10.1051/0004-6361:20030669.

S. Cabrit, S. Edwards, S. E. Strom, and K. M. Strom. Forbidden-line emission and infrared excesses in T Tauri stars - Evidence for accretion-driven mass loss? ApJ, 354:687–700, May 1990. doi: 10.1086/168725.

M. J. Cai, H. Shang, H.-H. Lin, and F. H. Shu. X-Winds in Action. ApJ, 672:489–503, January 2008. doi: 10.1086/523788.

N. Calvet, L. Hartmann, and S. J. Kenyon. Mass loss from pre-main-sequence accretion disks. I - The accelerating wind of FU Orionis. ApJ, 402:623–634, January 1993. doi: 10.1086/172164.

S. Campana, L. Stella, and J. A. Kennea. Swift Observations of SAX J1808.4-3658: Monitoring the Return to Quiescence. ApJ, 684:L99–L102, September 2008. doi: 10.1086/592002.

A. Caratti o Garatti, R. Garcia Lopez, A. Scholz, T. Giannini, J. Eislöffel, B. Nisini, F. Massi, S. Antoniucci, and T. P. Ray. The outburst of an embedded low-mass YSO in L1641. A&A, 526:L1, February 2011. doi: 10.1051/0004-6361/201016146.

C. Carrasco-González, L. F. Rodríguez, G. Anglada, J. Martí, J. M. Torrelles, and M. Osorio. A Magnetized Jet from a Massive Protostar. *Science*, 330:1209–, November 2010. doi: 10.1126/science.1195589.

C. Carrasco-González, J. M. Torrelles, J. Cantó, S. Curiel, G. Surcis, W. H. T. Vlemmings, H. J. van Langevelde, C. Goddi, G. Anglada, S.-W. Kim, J.-S. Kim, and J. F. Gómez. Observing the onset of outflow collimation in a massive protostar. *Science*, 348(6230):114–117, 2015. doi: 10.1126/science.aaa7216. URL http://www.sciencemag.org/content/348/6230/114.abstract.

F. Casse and R. Keppens. Magnetized Accretion-Ejection Structures: 2.5-dimensional Magnetohydrodynamic Simulations of Continuous Ideal Jet Launching from Resistive Accretion Disks. ApJ, 581:988–1001, December 2002. doi: 10.1086/344340.

F. Casse and R. Keppens. Radiatively Inefficient Magnetohydrodynamic Accretion-Ejection Structures. ApJ, 601:90–103, January 2004. doi: 10.1086/380441.

S. Chandrasekhar. The Stability of Non-Dissipative Couette Flow in Hydromagnetics. *Proceedings of the National Academy of Science*, 46:253–257, February 1960. doi: 10.1073/pnas.46.2.253.

D. Coffey, T. P. Downes, and T. P. Ray. The evolution and simulation of the outburst from XZ Tauri - A possible EXor? A&A, 419:593–598, May 2004. doi: 10.1051/0004-6361:20034316.

D. Coffey, F. Bacciotti, and L. Podio. T Tauri Jet Physics Resolved Near the Launching Region with the Hubble Space Telescope. ApJ, 689:1112–1126, December 2008. doi: 10.1086/592343.

M. L. Comins, M. M. Romanova, A. V. Koldoba, G. V. Ustyugova, and R. V. E. Lovelace. The effects of a magnetic field on planetary migration in laminar and turbulent discs. forthcoming.

W. Cui. Evidence for "Propeller" Effects in X-Ray Pulsars GX 1+4 and GRO J1744-28. ApJ, 482:L163, June 1997. doi: 10.1086/310712.

C. R. D'Angelo and H. C. Spruit. Episodic accretion on to strongly magnetic stars. MNRAS, 406:1208–1219, August 2010. doi: 10.1111/j.1365-2966.2010.16749.x.

C. R. D'Angelo and H. C. Spruit. Accretion discs trapped near corotation. MNRAS, 420:416–429, February 2012. doi: 10.1111/j.1365-2966.2011.20046.x.

G. D'Angelo and S. H. Lubow. Evolution of Migrating Planets Undergoing Gas Accretion. ApJ, 685:560–583, September 2008. doi: 10.1086/590904.

R. E. Davies, A. C. Fabian, and J. E. Pringle. Spindown of neutron stars in close binary systems. MNRAS, 186:779–782, March 1979.

S. F. Davis. Simplified second-order godunov-type methods. *SIAM J. Sci. Stat. Comput.*, 9(3):445–473, May 1988. ISSN 0196-5204. doi: 10.1137/0909030. URL http://dx.doi.org/10.1137/0909030.

T. di Salvo, L. Burderi, A. Riggio, A. Papitto, and M. T. Menna. Orbital evolution of an accreting millisecond pulsar: witnessing the banquet of a hidden black widow? MNRAS, 389:1851–1857, October 2008. doi: 10.1111/j.1365-2966.2008.13709.x.

J.-F. Donati and J. D. Landstreet. Magnetic Fields of Nondegenerate Stars. ARA&A, 47:333–370, September 2009. doi: 10.1146/annurev-astro-082708-101833.

J.-F. Donati, M. M. Jardine, S. G. Gregory, P. Petit, J. Bouvier, C. Dougados, F. Ménard, A. Collier Cameron, T. J. Harries, S. V. Jeffers, and F. Paletou. Magnetic fields and accretion flows on the classical T Tauri star V2129 Oph. MNRAS, 380:1297–1312, October 2007. doi: 10.1111/j.1365-2966.2007.12194.x.

J.-F. Donati, M. M. Jardine, S. G. Gregory, P. Petit, F. Paletou, J. Bouvier, C. Dougados, F. Menard, A. Collier Cameron, T. J. Harries, G. A. J. Hussain, Y. Unruh, J. Morin, S. C. Marsden, N. Manset, M. Auriere, C. Catala, and E. Alecian. Magnetospheric

accretion on the T Tauri star BP Tauri. MNRAS, 386:1234–1251, May 2008. doi: 10.1111/j.1365-2966.2008.13111.x.

J.-F. Donati, M. B. Skelly, J. Bouvier, S. G. Gregory, K. N. Grankin, M. M. Jardine, G. A. J. Hussain, F. Ménard, C. Dougados, Y. Unruh, S. Mohanty, M. Aurière, J. Morin, R. Farès, and MAPP Collaboration. Magnetospheric accretion and spin-down of the prototypical classical T Tauri star AA Tau. MNRAS, 409:1347–1361, December 2010. doi: 10.1111/j.1365-2966.2010.17409.x.

J.-F. Donati, J. Bouvier, F. M. Walter, S. G. Gregory, M. B. Skelly, G. A. J. Hussain, E. Flaccomio, C. Argiroffi, K. N. Grankin, M. M. Jardine, F. Ménard, C. Dougados, and M. M. Romanova. Non-stationary dynamo and magnetospheric accretion processes of the classical T Tauri star V2129 Oph. MNRAS, 412:2454–2468, April 2011. doi: 10.1111/j.1365-2966.2010.18069.x.

J.-F. Donati, S. G. Gregory, S. H. P. Alencar, J. Bouvier, G. Hussain, M. Skelly, C. Dougados, M. M. Jardine, F. Ménard, M. M. Romanova, Y. C. Unruh, and the MaPP collaboration. The large-scale magnetic field and poleward mass accretion of the classical t tauri star tw hya. MNRAS, pages no–no, 2011. ISSN 1365-2966. doi: 10.1111/j.1365-2966.2011.19288.x. URL http://dx.doi.org/10.1111/j.1365-2966.2011.19288.x.

C. Dougados, S. Cabrit, C. Lavalley, and F. Ménard. T Tauri stars microjets resolved by adaptive optics. A&A, 357:L61–L64, May 2000.

C. P. Dullemond, C. Dominik, and A. Natta. Passive Irradiated Circumstellar Disks with an Inner Hole. ApJ, 560:957–969, October 2001. doi: 10.1086/323057.

S. Dyda, R. V. E. Lovelace, G. V. Ustyugova, P. S. Lii, M. M. Romanova, and A. V.

Koldoba. Advection of matter and b-fields in alpha-discs. MNRAS, 432:127–137, June 2013. doi: 10.1093/mnras/stt429.

S. Dyda, R. V. E. Lovelace, G. V. Ustyugova, P. S. Lii, M. M. Romanova, and A. V. Koldoba. Asymmetric mhd outflows/jets from accreting t tauri stars. MNRAS, 450: 481–493, June 2015a. doi: 10.1093/mnras/stv623.

S. Dyda, R. V. E. Lovelace, G. V. Ustyugova, M. M. Romanova, and A. V. Koldoba. Counter-rotating accretion discs. MNRAS, 446:613–621, January 2015b. doi: 10.1093/mnras/stu2131.

S. Edwards, W. Fischer, J. Kwan, L. Hillenbrand, and A. K. Dupree. He I λ10830 as a Probe of Winds in Accreting Young Stars. ApJ, 599:L41–L44, December 2003. doi: 10.1086/381077.

S. Edwards, W. Fischer, L. Hillenbrand, and J. Kwan. Probing T Tauri Accretion and Outflow with 1 Micron Spectroscopy. ApJ, 646:319–341, July 2006. doi: 10.1086/504832.

K. Y. Ekşi, L. Hernquist, and R. Narayan. Where Are All the Fallback Disks? Constraints on Propeller Systems. ApJ, 623:L41–L44, April 2005. doi: 10.1086/429915.

R. F. Elsner and F. K. Lamb. Accretion by magnetic neutron stars. I - Magnetospheric structure and stability. ApJ, 215:897–913, August 1977. doi: 10.1086/155427.

M. L. Enoch, N. J. Evans, II, A. I. Sargent, and J. Glenn. Properties of the Youngest Protostars in Perseus, Serpens, and Ophiuchus. ApJ, 692:973, February 2009. doi: 10.1088/0004-637X/692/2/973.

N. J. Evans, II, M. M. Dunham, J. K. Jørgensen, M. L. Enoch, B. Merín, E. F. van Dishoeck, J. M. Alcalá, P. C. Myers, et al. The Spitzer c2d Legacy Results: Star-

Formation Rates and Efficiencies; Evolution and Lifetimes. ApJS, 181:321, April 2009. doi: 10.1088/0067-0049/181/2/321.

C. Fendt. Formation of Protostellar Jets as Two-Component Outflows from Star-Disk Magnetospheres. ApJ, 692:346–363, February 2009. doi: 10.1088/0004-637X/692/1/346.

C. Fendt and D. Elstner. Long-term evolution of a dipole type magnetosphere interacting with an accretion disk. II. Transition into a quasi-stationary spherically radial outflow. A&A, 363:208–222, November 2000.

J. Ferreira, C. Dougados, and S. Cabrit. Which jet launching mechanism(s) in T Tauri stars? A&A, 453:785–796, July 2006. doi: 10.1051/0004-6361:20054231.

C. Ferrigno, E. Bozzo, A. Papitto, N. Rea, L. Pavan, S. Campana, M. Wieringa, M. Filipović, M. Falanga, and L. Stella. Hiccup accretion in the swinging pulsar IGR J18245-2452. A&A, 567:A77, July 2014. doi: 10.1051/0004-6361/201322904.

A. Frank and G. Mellema. Hydrodynamical Models of Outflow Collimation in Young Stellar Objects. ApJ, 472:684–+, November 1996. doi: 10.1086/178099.

A. Frank, T. P. Ray, S. Cabrit, P. Hartigan, H. G. Arce, F. Bacciotti, J. Bally, M. Benisty, J. Eislöffel, M. Güdel, S. Lebedev, B. Nisini, and A. Raga. Jets and Outflows from Star to Cloud: Observations Confront Theory. *Protostars and Planets VI*, pages 451–474, 2014.

S. Fromang, C. Terquem, and R. P. Nelson. Numerical simulations of type I planetary migration in non-turbulent magnetized discs. MNRAS, 363:943–953, November 2005. doi: 10.1111/j.1365-2966.2005.09498.x.

C. F. Gammie. Layered Accretion in T Tauri Disks. ApJ, 457:355, January 1996. doi: 10.1086/176735.

P. Ghosh and F. K. Lamb. Disk accretion by magnetic neutron stars. ApJ, 223:L83–L87, July 1978. doi: 10.1086/182734.

S. K. Godunov. A difference method for numerical calculation of discontinuous solutions of the equations of hydrodynamics. *Matematicheskii Sbornik*, 89(3):271–306, 1959.

P. Goldreich and S. Tremaine. The excitation of density waves at the Lindblad and corotation resonances by an external potential. ApJ, 233:857–871, November 1979. doi: 10.1086/157448.

P. Goldreich and S. Tremaine. Disk-satellite interactions. ApJ, 241:425–441, October 1980. doi: 10.1086/158356.

A. I. Gómez de Castro and B. von Rekowski. On the source of dense outflows from T Tauri stars - III. Winds driven from the star-disc shear layer. MNRAS, 411:849–858, February 2011. doi: 10.1111/j.1365-2966.2010.17726.x.

A. P. Goodson and R. M. Winglee. Jets from Accreting Magnetic Young Stellar Objects. II. Mechanism Physics. ApJ, 524:159–168, October 1999. doi: 10.1086/307780.

A. P. Goodson, R. M. Winglee, and K.-H. Boehm. Time-dependent Accretion by Magnetic Young Stellar Objects as a Launching Mechanism for Stellar Jets. ApJ, 489: 199–+, November 1997. doi: 10.1086/304774.

A. P. Goodson, K.-H. Böhm, and R. M. Winglee. Jets from Accreting Magnetic Young Stellar Objects. I. Comparison of Observations and High-Resolution Simulation Results. ApJ, 524:142–158, October 1999. doi: 10.1086/307779.

S. G. Gregory, S. P. Matt, J.-F. Donati, and M. Jardine. The non-dipolar magnetic fields of accreting T Tauri stars. MNRAS, 389:1839–1850, October 2008. doi: 10.1111/j.1365-2966.2008.13687.x.

P. Hartigan, S. Edwards, and L. Ghandour. Disk Accretion and Mass Loss from Young Stars. ApJ, 452:736–+, October 1995. doi: 10.1086/176344.

P. Hartigan, S. Edwards, and R. Pierson. Going Slitless: Images of Forbidden-Line Emission Regions of Classical T Tauri Stars Observed with the Hubble Space Telescope. ApJ, 609:261–276, July 2004. doi: 10.1086/386317.

J. M. Hartman, A. Patruno, D. Chakrabarty, D. L. Kaplan, C. B. Markwardt, E. H. Morgan, P. S. Ray, M. van der Klis, and R. Wijnands. The Long-Term Evolution of the Spin, Pulse Shape, and Orbit of the Accretion-powered Millisecond Pulsar SAX J1808.4-3658. ApJ, 675:1468–1486, March 2008. doi: 10.1086/527461.

L. Hartmann and N. Calvet. Observational constraints on FU ORI winds. AJ, 109: 1846–1855, April 1995. doi: 10.1086/117411.

L. Hartmann and S. J. Kenyon. The FU Orionis Phenomenon. ARA&A, 34:207–240, 1996. doi: 10.1146/annurev.astro.34.1.207.

Lee Hartmann. *Accretion processes in star formation*, volume 32. Cambridge University Press, 2000.

Y. Hasegawa and R. E. Pudritz. The origin of planetary system architectures - I. Multiple planet traps in gaseous discs. MNRAS, 417:1236–1259, October 2011. doi: 10.1111/j.1365-2966.2011.19338.x.

M. R. Hayashi, K. Shibata, and R. Matsumoto. X-Ray Flares and Mass Outflows Driven by Magnetic Interaction between a Protostar and Its Surrounding Disk. ApJ, 468: L37+, September 1996. doi: 10.1086/310222.

G. H. Herbig. Eruptive phenomena in early stellar evolution. ApJ, 217:693–715, November 1977. doi: 10.1086/155615.

G. H. Herbig. FU Orionis eruptions. In B. Reipurth, editor, *European Southern Observatory Conference and Workshop Proceedings*, volume 33 of *European Southern Observatory Conference and Workshop Proceedings*, pages 233–246, September 1989.

G. H. Herbig. EX Lupi: History and Spectroscopy. AJ, 133:2679–2683, June 2007. doi: 10.1086/517494.

G. H. Herbig. History and Spectroscopy of EXor Candidates. AJ, 135:637–648, February 2008. doi: 10.1088/0004-6256/135/2/637.

S. Hirose, Y. Uchida, K. Shibata, and R. Matsumoto. Disk Accretion onto a Magnetized Young Star and Associated Jet Formation. PASJ, 49:193–205, April 1997.

S. Ida and D. N. C. Lin. Toward a Deterministic Model of Planetary Formation. V. Accumulation Near the Ice Line and Super-Earths. ApJ, 685:584–595, September 2008. doi: 10.1086/590401.

N. R. Ikhsanov. Supersonic propeller spindown of neutron stars in wind-fed mass-exchange close binaries. A&A, 381:L61–L63, January 2002. doi: 10.1051/0004-6361:20011661.

A. F. Illarionov and R. A. Sunyaev. Why the Number of Galactic X-ray Stars Is so Small? A&A, 39:185, February 1975.

W. Kley, B. Bitsch, and H. Klahr. Planet migration in three-dimensional radiative discs. A&A, 506:971–987, November 2009. doi: 10.1051/0004-6361/200912072.

A. V. Koldoba, G. V. Ustyugova, P.S. Lii, M.L. Comins, S. Dyda, M.M. Romanova, and R.V.E. Lovelace. Numerical MHD Codes for Modeling Astrophysical Flows. *ArXiv e-prints*, August 2015.

A. Königl. Disk accretion onto magnetic T Tauri stars. ApJ, 370:L39–L43, March 1991. doi: 10.1086/185972.

A. Königl and R. E. Pudritz. Disk Winds and the Accretion-Outflow Connection. *Protostars and Planets IV*, pages 759–+, May 2000.

A. Königl, M. M. Romanova, and R. V. E. Lovelace. Are the outflows in FU Orionis systems driven by the stellar magnetic field? MNRAS, 416:757–766, September 2011. doi: 10.1111/j.1365-2966.2011.19098.x.

R. Krasnopolsky, Z.-Y. Li, and R. Blandford. Magnetocentrifugal Launching of Jets from Accretion Disks. I. Cold Axisymmetric Flows. ApJ, 526:631–642, December 1999. doi: 10.1086/308023.

K. A. Kretke and D. N. C. Lin. The Importance of Disk Structure in Stalling Type I Migration. ApJ, 755:74, August 2012. doi: 10.1088/0004-637X/755/1/74.

M. J. Kuchner and M. Lecar. Halting Planet Migration in the Evacuated Centers of Protoplanetary Disks. ApJ, 574:L87–L89, July 2002. doi: 10.1086/342370.

M. Küker, T. Henning, and G. Rüdiger. Magnetic Star-Disk Coupling in Classical T Tauri Systems. ApJ, 589:397–409, May 2003. doi: 10.1086/374408.

A. K. Kulkarni and M. M. Romanova. Accretion to magnetized stars through the Rayleigh-Taylor instability: global 3D simulations. MNRAS, 386:673–687, May 2008. doi: 10.1111/j.1365-2966.2008.13094.x.

A. K. Kulkarni and M. M. Romanova. Analytical hotspot shapes and magnetospheric radius from 3D simulations of magnetospheric accretion. MNRAS, 433:3048–3061, August 2013. doi: 10.1093/mnras/stt945.

F. K. Lamb, C. J. Pethick, and D. Pines. A Model for Compact X-Ray Sources: Accretion by Rotating Magnetic Stars. ApJ, 184:271–290, August 1973. doi: 10.1086/152325.

C. Lavalley-Fouquet, S. Cabrit, and C. Dougados. DG Tau: A shocking jet. A&A, 356: L41–L44, April 2000.

J. Li and D. T. Wickramasinghe. Disc Accretion Onto Magnetic Stars: Slow Rotator and Propeller. In D. T. Wickramasinghe, G. V. Bicknell, & L. Ferrario, editor, *IAU Colloq. 163: Accretion Phenomena and Related Outflows*, volume 121 of *Astronomical Society of the Pacific Conference Series*, page 241, 1997.

P. Lii, M. Romanova, and R. Lovelace. Magnetic launching and collimation of jets from the disc-magnetosphere boundary: 2.5D MHD simulations. MNRAS, 420:2020–2033, March 2012. doi: 10.1111/j.1365-2966.2011.20133.x.

P. S. Lii, M. M. Romanova, G. V. Ustyugova, A. V. Koldoba, and R. V. E. Lovelace. Propeller-driven outflows from an MRI disc. MNRAS, 441:86–100, June 2014. doi: 10.1093/mnras/stu495.

P. S. Lii, M. M. Romanova, A. V. Koldoba, G. V. Ustyugova, and R. V. E. Lovelace. 3D Simulations of Planet Migration at Disc-Cavity Boundaries. forthcoming.

D. N. C. Lin, P. Bodenheimer, and D. C. Richardson. Orbital migration of the planetary companion of 51 Pegasi to its present location. Nature, 380:606–607, April 1996. doi: 10.1038/380606a0.

M. Long, M. M. Romanova, and R. V. E. Lovelace. Locking of the Rotation of Disk-Accreting Magnetized Stars. ApJ, 634:1214–1222, December 2005. doi: 10.1086/497000.

R. V. E. Lovelace. Dynamo model of double radio sources. Nature, 262:649–652, August 1976. doi: 10.1038/262649a0.

R. V. E. Lovelace, C. Mehanian, C. M. Mobarry, and M. E. Sulkanen. Theory of axisymmetric magnetohydrodynamic flows - Disks. ApJS, 62:1–37, September 1986. doi: 10.1086/191132.

R. V. E. Lovelace, J. C. L. Wang, and M. E. Sulkanen. Self-collimated electromagnetic jets from magnetized accretion disks. ApJ, 315:504–535, April 1987. doi: 10.1086/165156.

R. V. E. Lovelace, C. M. Mobarry, and J. Contopoulos. Magnetohydrodynamic flows in accretion disks and jets. In G. Belvedere, editor, *Accretion Disks and Magnetic Fields in Astrophysics*, volume 156, pages 71–90, 1989.

R. V. E. Lovelace, H. L. Berk, and J. Contopoulos. Magnetically driven jets and winds. ApJ, 379:696–705, October 1991. doi: 10.1086/170544.

R. V. E. Lovelace, M. M. Romanova, and G. S. Bisnovatyi-Kogan. Magnetic Propeller Outflows. ApJ, 514:368–372, March 1999. doi: 10.1086/306945.

R. V. E. Lovelace, H. Li, A. V. Koldoba, G. V. Ustyugova, and M. M. Romanova. Poynting Jets from Accretion Disks. ApJ, 572:445–455, June 2002. doi: 10.1086/340292.

R. V. E. Lovelace, M. M. Romanova, G. V. Ustyugova, and A. V. Koldoba. One-sided outflows/jets from rotating stars with complex magnetic fields. MNRAS, 408:2083–2091, November 2010. doi: 10.1111/j.1365-2966.2010.17284.x.

W. Lyra and M.-M. Mac Low. Rossby Wave Instability at Dead Zone Boundaries in Three-dimensional Resistive Magnetohydrodynamical Global Models of Protoplanetary Disks. ApJ, 756:62, September 2012. doi: 10.1088/0004-637X/756/1/62.

W. Lyra, A. Johansen, A. Zsom, H. Klahr, and N. Piskunov. Planet formation bursts at the borders of the dead zone in 2D numerical simulations of circumstellar disks. A&A, 497:869–888, April 2009. doi: 10.1051/0004-6361/200811265.

W. Lyra, S.-J. Paardekooper, and M.-M. Mac Low. Orbital Migration of Low-mass Planets in Evolutionary Radiative Models: Avoiding Catastrophic Infall. ApJ, 715: L68–L73, June 2010. doi: 10.1088/2041-8205/715/2/L68.

F. S. Masset and J. Casoli. On the Horseshoe Drag of a Low-Mass Planet. II. Migration in Adiabatic Disks. ApJ, 703:857–876, September 2009. doi: 10.1088/0004-637X/703/1/857.

F. S. Masset and J. Casoli. Saturated Torque Formula for Planetary Migration in Viscous Disks with Thermal Diffusion: Recipe for Protoplanet Population Synthesis. ApJ, 723:1393–1417, November 2010. doi: 10.1088/0004-637X/723/2/1393.

F. S. Masset, A. Morbidelli, A. Crida, and J. Ferreira. Disk Surface Density Transitions as Protoplanet Traps. ApJ, 642:478–487, May 2006. doi: 10.1086/500967.

T. Matsakos, K. Tsinganos, N. Vlahakis, S. Massaglia, A. Mignone, and E. Trussoni. Two-component jet simulations. I. Topological stability of analytical MHD outflow solutions. A&A, 477:521–533, January 2008. doi: 10.1051/0004-6361:20077907.

S. Matsumura, R. E. Pudritz, and E. W. Thommes. Saving Planetary Systems: Dead Zones and Planetary Migration. ApJ, 660:1609–1623, May 2007. doi: 10.1086/513175.

S. Matt and R. E. Pudritz. Accretion-powered Stellar Winds. II. Numerical Solutions for Stellar Wind Torques. ApJ, 678:1109–1118, May 2008. doi: 10.1086/533428.

S. Matt, A. P. Goodson, R. M. Winglee, and K.-H. Böhm. Simulation-based Investigation of a Model for the Interaction between Stellar Magnetospheres and Circumstellar Accretion Disks. ApJ, 574:232–245, July 2002. doi: 10.1086/340896.

S. Matt, R. Winglee, and K.-H. Böhm. Collimation of a central wind by a disc-associated magnetic field. MNRAS, 345:660–670, October 2003. doi: 10.1046/j.1365-8711.2003.06977.x.

L. Maurri, F. Bacciotti, L. Podio, J. Eislöffel, T. P. Ray, R. Mundt, U. Locatelli, and D. Coffey. Physical properties of the jet from DG Tauri on sub-arcsecond scales with HST/STIS. A&A, 565:A110, May 2014. doi: 10.1051/0004-6361/201117510.

K. A. Miller and J. M. Stone. Magnetohydrodynamic Simulations of Stellar Magnetosphere–Accretion Disk Interaction. ApJ, 489:890–+, November 1997. doi: 10.1086/304825.

T. Miyoshi and K. Kusano. A multi-state HLL approximate Riemann solver for ideal magnetohydrodynamics. *Journal of Computational Physics*, 208:315–344, September 2005. doi: 10.1016/j.jcp.2005.02.017.

H. K. Moffatt. *Magnetic field generation in electrically conducting fluids*. Cambridge University Press, Cambridge, England, 1978.

J. D. Monnier, R. Millan-Gabet, R. Billmeier, R. L. Akeson, D. Wallace, J.-P. Berger, N. Calvet, P. D'Alessio, W. C. Danchi, L. Hartmann, L. A. Hillenbrand, M. Kuchner, J. Rajagopal, W. A. Traub, P. G. Tuthill, A. Boden, et al. The Near-Infrared Size-Luminosity Relations for Herbig Ae/Be Disks. ApJ, 624:832–840, May 2005. doi: 10.1086/429266.

A. Morbidelli, A. Crida, F. Masset, and R. P. Nelson. Building giant-planet cores at a planet trap. A&A, 478:929–937, February 2008. doi: 10.1051/0004-6361:20078546.

G. C. Murphy, J. Ferreira, and C. Zanni. Large scale magnetic fields in viscous resistive accretion disks. I. Ejection from weakly magnetized disks. A&A, 512:A82+, March 2010. doi: 10.1051/0004-6361/200912633.

J. Muzerolle, N. Calvet, L. Hartmann, and P. D'Alessio. Unveiling the Inner Disk Structure of T Tauri Stars. ApJ, 597:L149–L152, November 2003. doi: 10.1086/379921.

J. R. Najita and F. H. Shu. Magnetocentrifugally driven flows from young stars and disks. 3: Numerical solution of the sub-Alfvenic region. ApJ, 429:808–825, July 1994. doi: 10.1086/174365.

M. Nakamura, I. L. Tregillis, H. Li, and S. Li. A Numerical Model of Hercules A by Magnetic Tower: Jet/Lobe Transition, Wiggling, and the Magnetic Field Distribution. ApJ, 686:843–850, October 2008. doi: 10.1086/591222.

R. P. Nelson, J. C. B. Papaloizou, F. Masset, and W. Kley. The migration and growth of protoplanets in protostellar discs. MNRAS, 318:18–36, October 2000. doi: 10.1046/j.1365-8711.2000.03605.x.

J. M. Oliveira, B. H. Foing, J. T. van Loon, and Y. C. Unruh. Magnetospheric accretion and winds on the T Tauri star SU Aurigae. Multi-spectral line variability and cross-correlation analysis. A&A, 362:615–627, October 2000.

R. Ouyed and R. E. Pudritz. Numerical Simulations of Astrophysical Jets from Keplerian Disks. I. Stationary Models. ApJ, 482:712–+, June 1997. doi: 10.1086/304170.

S.-J. Paardekooper. Dynamical corotation torques on low-mass planets. MNRAS, 444: 2031–2042, November 2014. doi: 10.1093/mnras/stu1542.

S.-J. Paardekooper and G. Mellema. Halting type I planet migration in non-isothermal disks. A&A, 459:L17–L20, November 2006. doi: 10.1051/0004-6361:20066304.

S.-J. Paardekooper and J. C. B. Papaloizou. On corotation torques, horseshoe drag and the possibility of sustained stalled or outward protoplanetary migration. MNRAS, 394:2283–2296, April 2009. doi: 10.1111/j.1365-2966.2009.14511.x.

S.-J. Paardekooper, C. Baruteau, A. Crida, and W. Kley. A torque formula for non-isothermal type I planetary migration - I. Unsaturated horseshoe drag. MNRAS, 401: 1950–1964, January 2010. doi: 10.1111/j.1365-2966.2009.15782.x.

S.-J. Paardekooper, C. Baruteau, and W. Kley. A torque formula for non-isothermal Type I planetary migration - II. Effects of diffusion. MNRAS, 410:293–303, January 2011. doi: 10.1111/j.1365-2966.2010.17442.x.

A. Papitto and D. F. Torres. A propeller model for the sub-luminous disk state of the transitional millisecond pulsar PSR J1023+0038. *ArXiv e-prints*, April 2015.

A. Papitto, A. Riggio, L. Burderi, T. di Salvo, A. D'Aí, and R. Iaria. Spin down during quiescence of the fastest known accretion-powered pulsar. A&A, 528:A55, April 2011. doi: 10.1051/0004-6361/201014837.

A. Papitto, C. Ferrigno, E. Bozzo, N. Rea, L. Pavan, L. Burderi, M. Burgay, S. Campana, T. di Salvo, M. Falanga, M. D. Filipović, P. C. C. Freire, J. W. T. Hessels, A. Possenti, S. M. Ransom, A. Riggio, P. Romano, J. M. Sarkissian, I. H. Stairs, L. Stella, D. F. Torres, M. H. Wieringa, and G. F. Wong. Swings between rotation and accretion power in a binary millisecond pulsar. Nature, 501:517–520, September 2013. doi: 10.1038/nature12470.

A. Papitto, D. F. Torres, and J. Li. A propeller scenario for the gamma-ray emission of low-mass X-ray binaries: the case of XSS J12270-4859. MNRAS, 438:2105–2116, March 2014. doi: 10.1093/mnras/stt2336.

A. Patruno. The Accreting Millisecond X-ray Pulsar IGR J00291+5934: Evidence for a Long Timescale Spin Evolution. ApJ, 722:909–918, October 2010. doi: 10.1088/0004-637X/722/1/909.

A. Patruno and A. L. Watts. Accreting Millisecond X-Ray Pulsars. *ArXiv e-prints*, June 2012.

A. Patruno, A. Watts, M. Klein Wolt, R. Wijnands, and M. van der Klis. 1 Hz Flaring in SAX J1808.4-3658: Flow Instabilities near the Propeller Stage. ApJ, 707:1296–1309, December 2009. doi: 10.1088/0004-637X/707/2/1296.

A. Patruno, A. M. Archibald, J. W. T. Hessels, S. Bogdanov, B. W. Stappers, C. G. Bassa, G. H. Janssen, V. M. Kaspi, S. Tendulkar, and A. G. Lyne. A New Accretion Disk around the Missing Link Binary System PSR J1023+0038. ApJ, 781:L3, January 2014. doi: 10.1088/2041-8205/781/1/L3.

T.-S. Pyo, M. Hayashi, N. Kobayashi, H. Terada, and A. T. Tokunaga. Spatio-Kinematic Structure at the Base of the [Fe II] Jets from L1551 IRS 5. ApJ, 694:654–663, March 2009. doi: 10.1088/0004-637X/694/1/654.

S. A. Rappaport, J. M. Fregeau, and H. Spruit. Accretion onto Fast X-Ray Pulsars. ApJ, 606:436–443, May 2004. doi: 10.1086/382863.

T. Ray, C. Dougados, F. Bacciotti, J. Eislöffel, and A. Chrysostomou. Toward Resolving the Outflow Engine: An Observational Perspective. *Protostars and Planets V*, pages 231–244, 2007.

B. Reipurth. Herbig-Haro objects and FU Orionis eruptions - The case of HH 57. A&A, 143:435–442, February 1985.

W. K. M. Rice, P. J. Armitage, and D. F. Hogg. Why are there so few hot Jupiters? MNRAS, 384:1242–1248, March 2008. doi: 10.1111/j.1365-2966.2007.12817.x.

M. M. Romanova and R. V. E. Lovelace. The Magnetospheric Gap and the Accumulation of Giant Planets Close to a Star. ApJ, 645:L73–L76, July 2006. doi: 10.1086/505967.

M. M. Romanova, G. V. Ustyugova, A. V. Koldoba, V. M. Chechetkin, and R. V. E. Lovelace. Formation of Stationary Magnetohydrodynamic Outflows from a Disk by Time-dependent Simulations. ApJ, 482:708–+, June 1997. doi: 10.1086/304199.

M. M. Romanova, G. V. Ustyugova, A. V. Koldoba, and R. V. E. Lovelace. Magnetohydrodynamic Simulations of Disk-Magnetized Star Interactions in the Quiescent Regime: Funnel Flows and Angular Momentum Transport. ApJ, 578:420–438, October 2002. doi: 10.1086/342464.

M. M. Romanova, G. V. Ustyugova, A. V. Koldoba, J. V. Wick, and R. V. E. Lovelace. Three-dimensional Simulations of Disk Accretion to an Inclined Dipole. I. Magnetospheric Flows at Different Θ. ApJ, 595:1009–1031, October 2003. doi: 10.1086/377514.

M. M. Romanova, G. V. Ustyugova, A. V. Koldoba, and R. V. E. Lovelace. The Propeller Regime of Disk Accretion to a Rapidly Rotating Magnetized Star. ApJ, 616:L151–L154, December 2004. doi: 10.1086/426586.

M. M. Romanova, G. V. Ustyugova, A. V. Koldoba, and R. V. E. Lovelace. Propeller-driven Outflows and Disk Oscillations. ApJ, 635:L165–L168, December 2005. doi: 10.1086/499560.

M. M. Romanova, G. V. Ustyugova, A. V. Koldoba, and R. V. E. Lovelace. Launching of conical winds and axial jets from the disc-magnetosphere boundary: axisymmetric and 3D simulations. MNRAS, 399:1802–1828, November 2009. doi: 10.1111/j.1365-2966.2009.15413.x.

M. M. Romanova, G. V. Ustyugova, A. V. Koldoba, and R. V. E. Lovelace. MRI-driven accretion on to magnetized stars: axisymmetric MHD simulations. MNRAS, 416: 416–438, September 2011. doi: 10.1111/j.1365-2966.2011.19050.x.

D. M. Rothstein and R. V. E. Lovelace. Advection of Magnetic Fields in Accretion Disks: Not So Difficult After All. ApJ, 677:1221–1232, April 2008. doi: 10.1086/529128.

G. Sandell and D. A. Weintraub. On the Similarity of FU Orionis Stars to Class I Protostars: Evidence from the Submillimeter. ApJS, 134:115–132, May 2001. doi: 10.1086/320360.

E. Schisano, E. Covino, J. M. Alcalá, M. Esposito, D. Gandolfi, and E. W. Guenther. Variability of the transitional T Tauri star T Chamaeleontis. A&A, 501:1013–1030, July 2009. doi: 10.1051/0004-6361/200811073.

N. I. Shakura and R. A. Sunyaev. Black holes in binary systems. Observational appearance. A&A, 24:337–355, 1973.

F. Shu, J. Najita, E. Ostriker, F. Wilkin, S. Ruden, and S. Lizano. Magnetocentrifugally driven flows from young stars and disks. 1: A generalized model. ApJ, 429:781–796, July 1994. doi: 10.1086/174363.

A. Sicilia-Aguilar, Á. Kóspál, J. Setiawan, P. Ábrahám, C. Dullemond, C. Eiroa, M. Goto, T. Henning, and A. Juhász. Optical spectroscopy of EX Lupi during quiescence and outburst. Infall, wind, and dynamics in the accretion flow. A&A, 544:A93, August 2012. doi: 10.1051/0004-6361/201118555.

M. A. Skinner and E. C. Ostriker. The Athena Astrophysical Magnetohydrodynamics Code in Cylindrical Geometry. ApJS, 188:290–311, May 2010. doi: 10.1088/0067-0049/188/1/290.

H. C. Spruit and R. E. Taam. An instability associated with a magnetosphere-disk interaction. ApJ, 402:593–604, January 1993. doi: 10.1086/172162.

H. C. Spruit, R. Stehle, and J. C. B. Papaloizou. Interchange instability in and accretion disc with a poloidal magnetic field. MNRAS, 275:1223–1231, August 1995.

G. Srinivasan. Recycled pulsars. New A Rev., 54:93–100, March 2010. doi: 10.1016/j.newar.2010.09.026.

J. E. Staff, B. P. Niebergal, R. Ouyed, R. E. Pudritz, and K. Cai. Confronting Three-dimensional Time-dependent Jet Simulations with Hubble Space Telescope Observations. ApJ, 722:1325–1332, October 2010. doi: 10.1088/0004-637X/722/2/1325.

L. Stella, N. E. White, and R. Rosner. Intermittent stellar wind accretion and the long-term activity of Population I binary systems containing an X-ray pulsar. ApJ, 308: 669–679, September 1986. doi: 10.1086/164538.

T. F. Stepinski. Generation of dynamo magnetic fields in the primordial solar nebula. Icarus, 97:130–141, May 1992. doi: 10.1016/0019-1035(92)90062-C.

T. F. Stepinski and E. H. Levy. Generation of dynamo magnetic fields in protoplanetary and other astrophysical accretion disks. ApJ, 331:416–434, August 1988. doi: 10.1086/166569.

R. A. Sunyaev and N. I. Shakura. Disk reservoirs in binary systems and prospects for observing them. *Pisma v Astronomicheskii Zhurnal*, 3:262–266, June 1977.

H. Tanaka, T. Takeuchi, and W. R. Ward. Three-Dimensional Interaction between a Planet and an Isothermal Gaseous Disk. I. Corotation and Lindblad Torques and Planet Migration. ApJ, 565:1257–1274, February 2002. doi: 10.1086/324713.

T. Tanaka. Finite volume TVD scheme on an unstructured grid system for three-dimensional MHD simulation of inhomogeneous systems including strong background potential fields. *Journal of Computational Physics*, 111:381–390, April 1994. doi: 10.1006/jcph.1994.1071.

Eleuterio F Toro. *Riemann solvers and numerical methods for fluid dynamics: a practical introduction*. Springer Science & Business Media, 2009.

Eleuterio F Toro, M Spruce, and W Speares. Restoration of the contact surface in the hll-riemann solver. *Shock waves*, 4(1):25–34, 1994.

Gábor Tóth. The [backward difference]ůB=0 Constraint in Shock-Capturing Magnetohydrodynamics Codes. *Journal of Computational Physics*, 161(2):605 – 652, 2000. ISSN 0021-9991. doi: DOI: 10.1006/jcph.2000.6519. URL http://www.sciencedirect.com/science/article/pii/S0021999100965197.

G. V. Ustyugova, A. V. Koldoba, M. M. Romanova, V. M. Chechetkin, and R. V. E. Lovelace. Magnetocentrifugally Driven Winds: Comparison of MHD Simulations with Theory. ApJ, 516:221–235, May 1999. doi: 10.1086/307093.

G. V. Ustyugova, R. V. E. Lovelace, M. M. Romanova, H. Li, and S. A. Colgate. Poynting Jets from Accretion Disks: Magnetohydrodynamic Simulations. ApJ, 541:L21–L24, September 2000. doi: 10.1086/312890.

G. V. Ustyugova, A. V. Koldoba, M. M. Romanova, and R. V. E. Lovelace. "Propeller" Regime of Disk Accretion to Rapidly Rotating Stars. ApJ, 646:304–318, July 2006. doi: 10.1086/503379.

EP Velikhov. Stability of an ideally conducting liquid flowing between rotating cylinders in a magnetic field. *Zhur. Eksptl'. i Teoret. Fiz.*, 36, 1959.

Y. M. Wang and J. A. Robertson. 'Propeller' action by rotating neutron stars. A&A, 151:361–371, October 1985.

W. R. Ward. Density waves in the solar nebula - Differential Lindblad torque. Icarus, 67:164–180, July 1986. doi: 10.1016/0019-1035(86)90182-X.

W. R. Ward. Protoplanet Migration by Nebula Tides. Icarus, 126:261–281, April 1997. doi: 10.1006/icar.1996.5647.

R. J. White and A. M. Ghez. Observational Constraints on the Formation and Evolution of Binary Stars. ApJ, 556:265–295, July 2001. doi: 10.1086/321542.

G. A. Wynn, A. R. King, and K. Horne. A magnetic propeller in the cataclysmic variable AE Aquarii. MNRAS, 286:436–446, April 1997.

H. Yang and C. M. Johns-Krull. Magnetic Field Measurements of T Tauri Stars in the Orion Nebula Cluster. ApJ, 729:83–+, March 2011. doi: 10.1088/0004-637X/729/2/83.

C. Zanni and J. Ferreira. MHD simulations of accretion onto a dipolar magnetosphere. II. Magnetospheric ejections and stellar spin-down. A&A, 550:A99, February 2013. doi: 10.1051/0004-6361/201220168.

C. Zanni, A. Ferrari, R. Rosner, G. Bodo, and S. Massaglia. MHD simulations of jet acceleration from Keplerian accretion disks. The effects of disk resistivity. A&A, 469:811–828, July 2007. doi: 10.1051/0004-6361:20066400.